POLITECNICO DI MILANO

Scuola di Ingegneria Industriale e dell'Informazione
Corso di studi in Ingegneria Aeronautica

POLITECNICO
MILANO 1863

VIBROACOUSTIC METHODOLOGY FOR TRANSFORMERS AIR-BORNE NOISE COMPUTATION BASED ON FEM MULTIPHYSICS APPROACH

Relatore: Prof. Lorenzo Dozio

Correlatore: Ing. Luigi De Mercato

Tesi di Laurea Magistrale di:

Vito Murgida 927969

Anno Accademico 2021/2022

Alla mia famiglia, che mi ha supportato in ogni momento di questa ardua avventura.

Grazie, vi amo.

1. Introduction

The objective of this work is to build a methodology based on Finite Element Method for computing noise emissions of transformers based on a review of the numerous papers present in literature as well as on what has been studied by researchers in the company during the past years. The main source mechanisms are studied and modeling techniques are proposed. Since some of the mechanisms involved in transformers noise are not perfectly understood still today, this work gives also a contribution to the research.

Based on the nature of the problem, a multi-physic approach is adopted. The three involved physics, Electromagnetism, Structural Mechanics and Acoustics (air-borne noise) are explicitly modeled making use of FEM and one-way coupling. A model of an on-board traction reactor is developed to test the methodology and give to the readers more insight into the methodology. Figure 1 shows the workflow followed in the methodology.

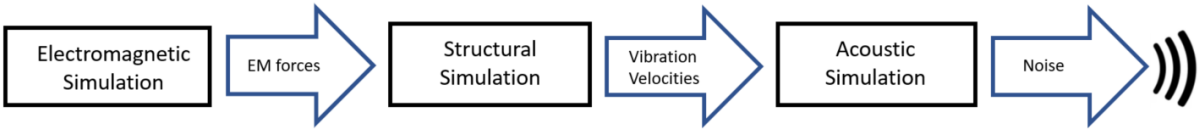

Figure 1 - Methodology Workflow

In the past years, a technology gap between research and engineering was suffered on acoustic topics related to transformers in Hitachi Energy. Many independent studies have been conducted by researchers but none of them has been converted in a ready-to-use methodology to be integrated in the engineering process. However, with the new eco-directives coming and the pressing demand from customers, a methodology for noise emission computation became a must.

This methodology represents the starting point of a roadmap whose final output will be a technical standard containing design rules for transformers noise minimization. However, some mechanisms and the effect of some parameters are still not clear today. Some tentative of understanding them has been done in this work and effort will be put in future works for reaching a deep knowledge, being able to model and control them.

The reason of the choice of such a thesis from an Aeronautical Structural Engineering student is due to the many analogies and to the adoption of the same models and numerical tools as the ones used for structures in the aeronautical field. As for aeronautics, multi-physics is a peculiarity of transformers: as the aerodynamic loads are mapped onto the airplane structure to compute its response, electromagnetic loads are responsible for transformer structure excitation. Moreover, acoustics is a topic of increasing importance in the helicopter industry on which a background has been obtained during the course studies. Regarding modeling tools, Finite Element method, for which a strong background is provided from the Aeronautical Structural Engineering course, is used in both aeronautical and transformer fields. Same modeling concepts and analytical models are used. Finally, even if not discussed in this thesis, concepts as mass minimization, structural integrity under fatigue, impact events, fluid-dynamics are typical of transformers as well of airplanes, which makes the background of an aeronautical engineer well fitting in this field.

Table of contents

2. Transformers structural concept

Before going into the details of the source of noise generation, it is useful to review the structural configuration of a transformer in order to have a clearer understanding of the terminology used later. Transformers are made of four main parts: winding, core, frame and tank. An example is shown in Figure 2.

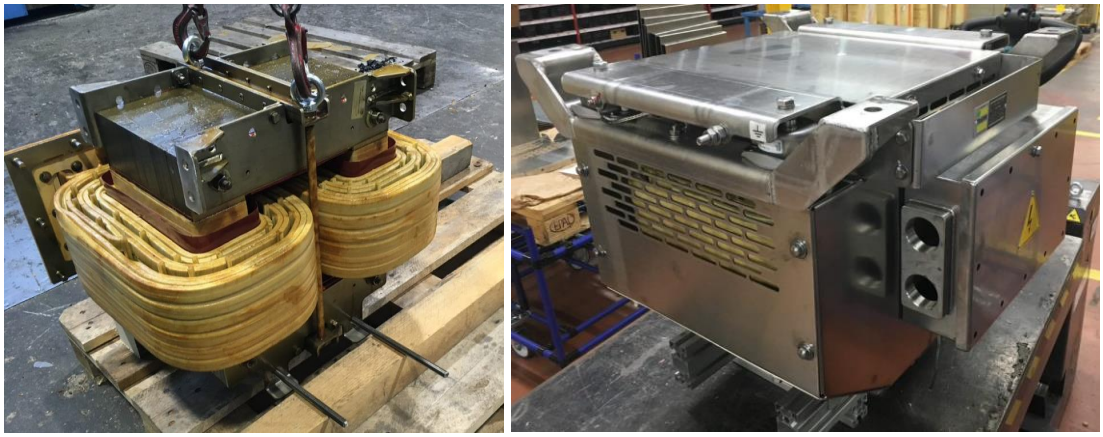

Figure 2 - Example of single-phase traction reactor for rail applications. The two windings are connected in parallel.

Winding is composed of copper or aluminum sheets or cables wrapped to form a winding with cylindrical or rectangular shape. The winding is travelled by alternating current. For *power, distribution* and *traction transformers*, which are used to transfer the power between two lines at different voltage, two different windings are needed: the input one, where current comes in at a high/medium voltage, called primary winding, and the output one, where the current induced by the magnetic field exits at a low voltage, called secondary. The primary and secondary windings are concentric. On the other side, *traction reactors* (example in Figure 2) are used as filters to remove high-frequency harmonics from the signal which will be transmitted to the traction system of a train, and they are composed of a primary winding only. The conductor is covered by insulating materials, like paper, and then impregnated by cured resin whose function is that of protecting the winding from damages. Then, it can be considered a composite material. The winding is divided in sections, separated by sticks made of fiberglass or aluminum whose function is that of creating cooling channels. In Figure 3 windings with cooling channels are visible.

Figure 3 - Winding with the presence of cooling channels (in white)

Core is a lamination stack of electrical steel (silicon-iron alloy) thin sheets with a thickness of the order of 10 μm and covered by insulating varnish. A core made of insulated laminas reduces drastically the induced currents inside the core, decreasing the power dissipated by heat (core losses) and increasing the power transmission efficiency. The sheets are typically manufactured by means of cold rolling techniques and for this reason they present oriented grains. This creates electromagnetic and mechanical anisotropies in the material. The core is composed of vertical columns, on which windings are mounted, and horizontal upper and lower yokes, which connect the columns creating a closed magnetic circuit. Figure 4 shows an example of a yoke. The joints between columns and yokes can be realized in different ways and each of them has an impact on power transmission efficiency and noise emission. The core is travelled by an induced magnetic flux. In traction reactors, air-gaps made of fiber glass (low permeability material) perpendicular to the laminas planes are inserted between different lamination stacks in the columns, in order to increase the total reluctance of the equivalent magnetic circuit and consequently decrease the magnetic flux.

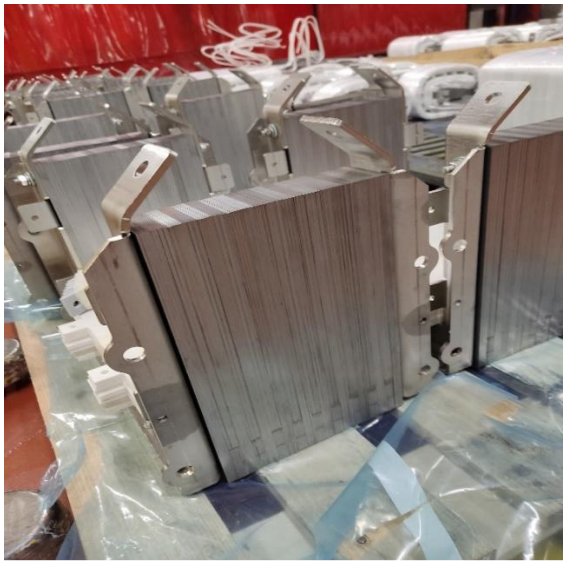

Figure 4 - Core yoke

The *Frame* is the structure whose function is that of keeping the core lamination stack together and maintain nominal geometrical configuration during operation, providing stiffness to the whole assembly. It is also needed to connect the transformer to the tank. It is made of bolted steel profiles and plates. The clamping pressure applied influences efficiency and noise emission. Figure 5 shows an example of frame of a distribution transformers.

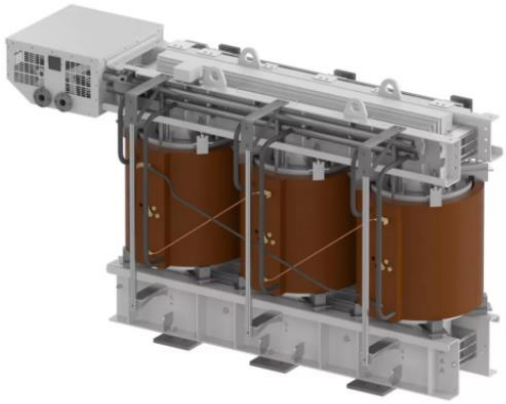

Figure 5 - Dry-type distribution transformer

The *Tank* is a container in which the transformer is inserted. In case of oil-type high power and distribution transformers this is filled with oil, whereas this is not the case for dry-type transformers and reactors. It can have cylindrical or box shape according to the specific application. For large power and distribution transformers, usually it is a box made of thin stiffened panels, as shown on Figure 6. For these applications, it is actually the main source of noise, being subjected to electromagnetic forces and to the loads transmitted from the transformer through the oil.

Figure 6 – Distribution transformer tank

3. Introduction to transformers noise

The mechanisms of noise generation applied to industrial transformers have been object of research during the last 60 years. The target was to understand which the sources are, how they can be associated to the generated noise and how can they be modeled. The main noise sources can be classified as:
- Lorentz force
- Maxwell forces
- Magnetostriction and
- Cooling systems.

Lorentz forces are generated by the interaction between the current flowing through the winding and the induced magnetic field. Since the winding is travelled by alternating current, Lorentz forces act as an alternating force applied to the windings, making them vibrate in the axial and radial direction and emit the so-called *Load noise.*

Maxwell forces, also known as *magnetic forces,* are surface forces concentrated on the free surfaces of the core as well as on transformer tank. They can be described as a stress acting on the free surfaces of the core.

Magnetostriction is a magneto-mechanical coupling typical of ferromagnetic materials, as the one used in the core. When a magnetic flux density travels in such materials, they react with a mechanical strain. Since alternating current is used, alternating magnetic flux is produced. Core vibration occurs and noise is emitted. Magnetostriction generates also on the tank, where a magnetic field is present as well. Noise generated by magnetostriction and Maxwell forces is referred to as *Core noise* while noise generated by tank vibration is referred to as *Tank noise.*

Cooling systems are used for heat dissipation in transformers. Winding is cooled by forcing a fluid through fans or pumps. Turbulence and vorticity generated by such machines represent a source of noise. Since only vibroacoustic will be object of this work, noise emission due to cooling system, known as aeroacoustics, is not here considered. Together with the aerodynamic noise, cooling system produces noise due to the eccentricities of rotating systems, which generate vibrations.

It is evident that finding acoustic emissions of a transformer means dealing with a multi-physics environment in which Electromagnetism, Structural Mechanics and Acoustics are coupled. Numerical, analytical and empirical models have been developed for this scope, but still today there are open points to be clarified, as for example the nature of magnetostriction and the effect of the compression of the core on emitted noise. In the following paragraphs a more insightful illustration of the source mechanisms and the affecting parameters will be given.

3.1 Lorentz forces

Lorentz forces are generated by the interaction between the current travelling in the winding and the induced magnetic field. Lorentz forces are composed by a DC component, constant in time, and an AC component, sinusoidal in time. Since they depend on the square of the current, the AC component of Lorentz forces has double the frequency of the current. Lorentz forces have two main components: a radial component which has a parabolic distribution along the winding axis (maximum at the center) and an axial component which is null at the center and maximum at the top and bottom extremities. This force distribution generates an operative deformation of the winding which is known as *breathing* mode or *barrel deformation*. Figure 7 shows a schematic.

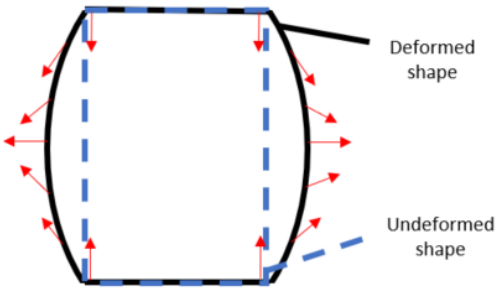

Figure 7 - Lorentz forces and barrel deformation

Being acoustic power dependent on the square of the vibration velocity, being the latter linearly dependent on the Lorentz forces and being Lorentz forces dependent on the square of the current, the acoustic power generated by Lorentz forces depends on the 4th power of the input current. According to standards [1], winding noise can be calculated using the following formula [2] where S_r denotes the rated power of the transformer (in MVA) and MVA is the reference power (1 MVA).

$$L = 39 + 18 \log_{10}\left(\frac{S_r}{MVA}\right)$$

However, experimental tests show a deviation of 5-10 dB. Ali *Al-Abadi* [2] developed an empirical formula based on the fitting of several experimental tests conducted on transformers, which is a modification of the formula suggested by regulations in which some parameters are introduced in order to take into account the influence of winding geometry, winding type, winding material and clamping force on radiated noise through several experimental tests combined with machine learning algorithms. The formula gives higher accuracy than the one suggested by regulations with a maximum deviation on several measurements of about 5 dB. However, the mechanisms involved in the transmission of winding vibration to the structure and how they affect noise cannot be deeply understood with such procedure, leading to the impossibility of finding new solutions.

Finite Elements are therefore needed for a deeper and more systematic understanding. *Kavasoglu* et al. [3] presented a FE 2D model in which a multi-physic analysis has been performed and load noise has been computed, as shown in Figure 8. Sound Power Level showed a deviation from experimental results of less than 2 dB.

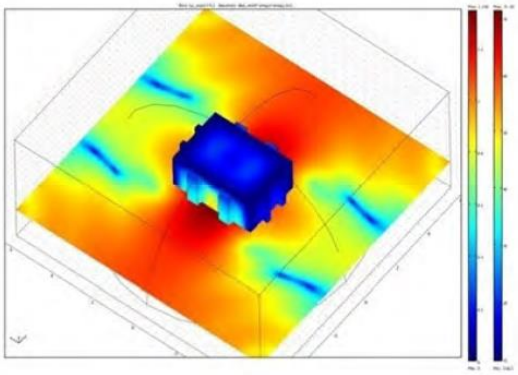

Figure 8 - Tank wall displacements and sound pressure field outside the tank [3]

An alternative modelling technique based on 3-dimensional equivalent magnetic circuit network (3D EMCN) is proposed in [4]. EMCN is a simplified modeling technique in which magnetic quantities and Lorentz forces can be computed using an equivalent magnetic circuit composed by lumped permeances (inverse of reluctances), magnetomotive forces and magnetic fluxes. Figure 9 shows the idea behind this method. After having calculated the Lorentz forces, the average vibration velocity is computed making use of dynamics equation, in which the winding is considered as a cylinder whose mass is

known and whose stiffness can be analytically computed knowing the material property and the geometry of the winding. After having computed the vibration velocity, the winding is assumed to be an unbaffled speaker and dipole model analytical formulas are used to compute the radiated SPL. The following formula for the calculation of emitted Sound Power Level is obtained, where D is the diameter of the winding, E is the Young's modulus of the winding material, ρ_0 is the air density, c is the sound speed, K is the wavenumber, A is the surface area of the winding, F_0 is the magnitude of Lorentz forces, s can be set equal to the winding diameter, d is the winding thickness, L_C is the winding height, m is the mass of the winding, ω is the frequency of the force, P_{ref} is the reference sound pressure (20 μPa).

$$Noise = 20\log_{10}\left(\frac{12D^3\rho_0 cK^2 AF_0 s}{\left(16\pi Ed^3 L_c - 12D^3 m\omega^2\right)4\sqrt{2}\pi r P_{ref}}\right)$$

Next, some coefficients have been added to the equation to take into account the effect of the thickness of the winding, the thickness of the insulating paper and the area of the tank, obtaining an improved equation. Finally, experimental activities have been run for measuring the load noise of 32 different transformers. Standard deviations of the original equation and the improved one has been found to be 3.77 dBA and 1.90 dBA respectively, showing the applicability of the method for load noise prediction.

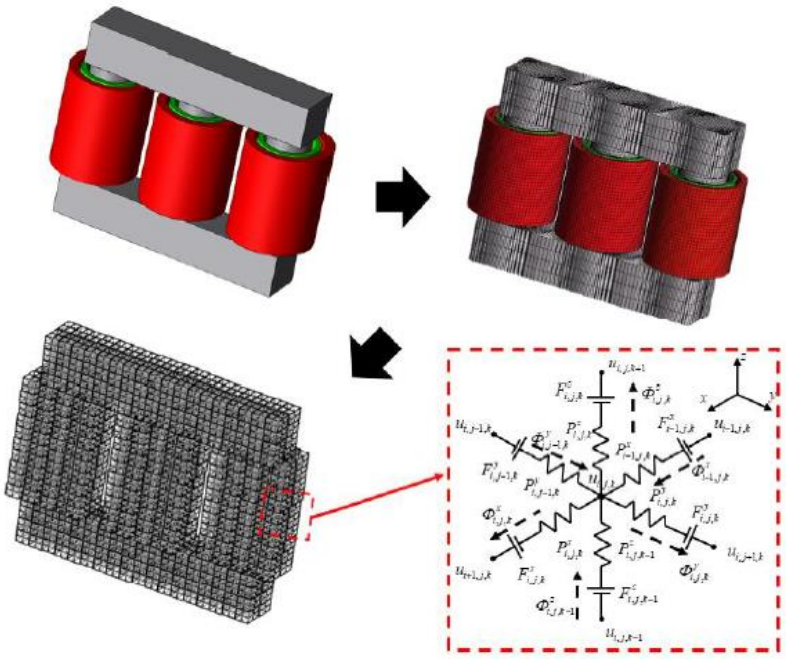

Figure 9 - 3D EMCN method [4]

3.2 Maxwell forces

Maxwell forces, also known as magnetic forces, are surface forces concentrated at the core and tank surfaces. They are expressed as a stress distribution. Maxwell forces depend on the square of the magnetic field at each time instant, meaning that they have double the frequency of the magnetic field (and of the exciting current). Maxwell forces act as attracting forces between core laminas and core stacks. They also act on the tank due to parasitic currents induced on it by the magnetic field. Maxwell forces are the same forces responsible for attraction-repulsion of magnets as well as for electric motors

rotation. Being acoustic power dependent on the square of the vibration velocity, being the latter linearly dependent on the Maxwell forces and being the Maxwell forces dependent on the square of the current, the acoustic power generated by Maxwell forces depends on the 4th power of the input current. Pfützner [5] has found that Maxwell forces are negligible in power transformers compared to Lorentz forces and magnetostriction. During the development of the methodology presented for this thesis, it has been found that this consideration doesn't apply to reactors with core air-gaps.

3.3 Magnetostriction

Magnetostriction is a magneto-mechanical coupling typical of ferromagnetic materials. When a ferromagnetic material, like the electrical steel composing the core of a transformer, is travelled by magnetic flux, it reacts with a deformation. Magnetostriction is a hysteretic non-linear phenomenon, described by the so-called butterfly curves, which associates the magnetic field with the strain in the material. An example of these curves is shown on Figure 10. For a pure alternating current, magnetostriction behavior is symmetric with respect the vertical axis, whereas if a DC bias is present, magnetostriction behavior becomes unsymmetrical. Experimental evidence shows that the higher the DC bias, the higher the noise emitted [1]. Magnetostriction is in general of the order of 10-6 ϵ and is indicated in $\mu\epsilon$ or *ppm.*

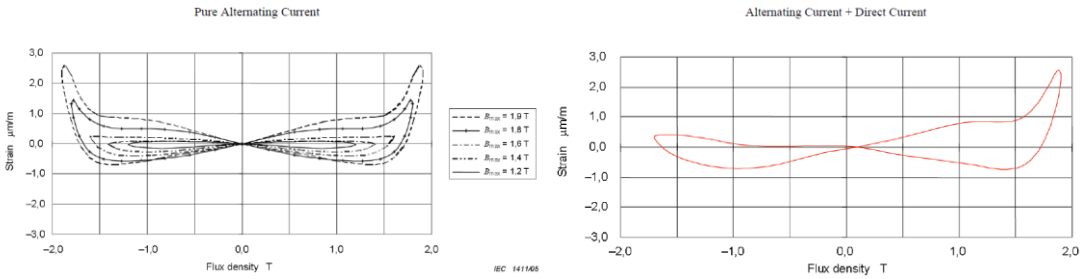

Figure 10 - Magnetostriction with pure alternating current (left) and with direct + alternating current (right) [1]

Magnetostriction can also be described analytically as a strain depending on the magnetic field by a polynomial in which only even powers are present, which means that magnetostriction has a fundamental harmonic at double the frequency of the magnetic field plus higher even harmonics. If a DC bias is present, odd harmonics spot out. Moreover, magnetostriction is anisotropic due to the material anisotropies originated by rolling during manufacturing. Deformation is predominant in the rolling direction for grain oriented electrical steel. Figure 11 shows the typical behavior of magnetostriction in time domain.

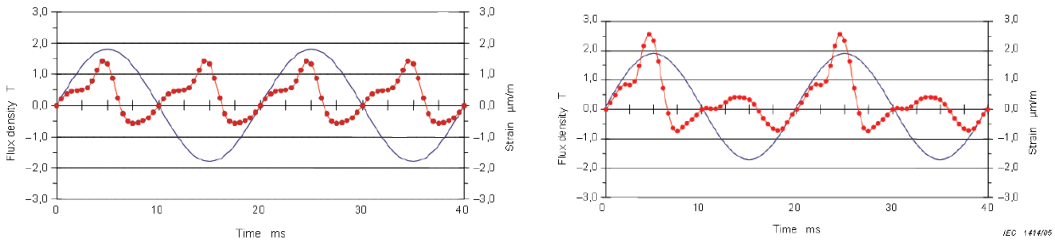

Figure 11 - Magnetic flux (blue) and strain (red) for pure alternating current (left) and direct + alternating current (right) [1]

Magnetostriction is experimentally measured using the so-called Epstein sample, which is a single sheet of electrical steel 305 mm in length and 30 mm in width. A stack of multiple sheets is used. Figure 12 shows the typical experimental setup for magnetostriction measurements. The Epstein samples are assembled by means of overlapping and a squared core is realized. Excitation coils are used to induce

a magnetic field while search coils are used to monitor it. Magnetostriction is measured by means of strain gauges, piezoelectric accelerometers or vibrometers [6] [7].

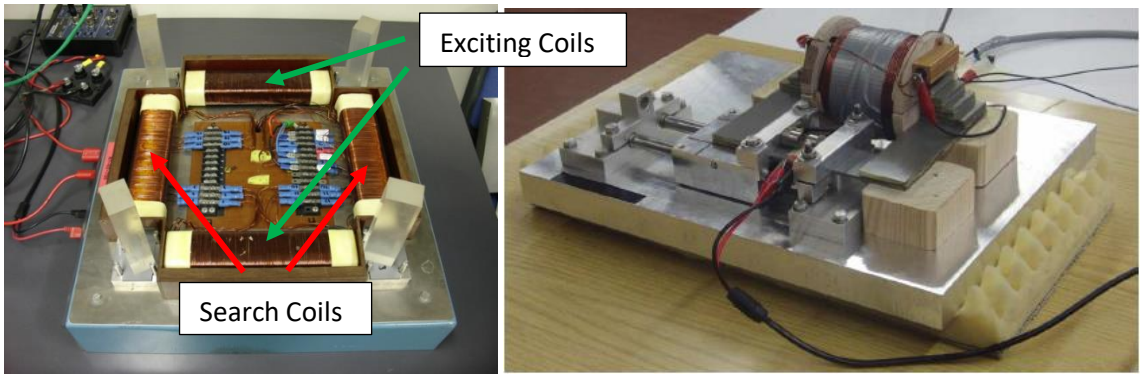

Figure 12 - Epstein frame [6] [7]

3.3.1 In-plane transverse deformation and out of plane deformation

In addition to the deformation in the rolling direction, deformations in the transverse and normal directions occur. They have an opposite sign with respect to the deformations in rolling direction. Figure 13 shows the maximum strain of a grain oriented electrical steel in the three space directions for magnetic fluxes with different direction, as measured by Weiser and Pfützner [5]. ψ denotes the angle between the magnetic flux direction and the rolling one, while λ_z denotes the out-of-plane strain. For an angle ψ equal to zero, magnetic flux is aligned with rolling direction. It is evident that deformation in rolling direction is always higher. Also, for a magnetic field in transverse direction ($\psi = 90°$), magnetostriction reaches the highest values. Angles ψ different from zero are present in correspondence of the joints between columns and yokes, where the magnetic flux changes direction. The same results have been found by other researchers [8].

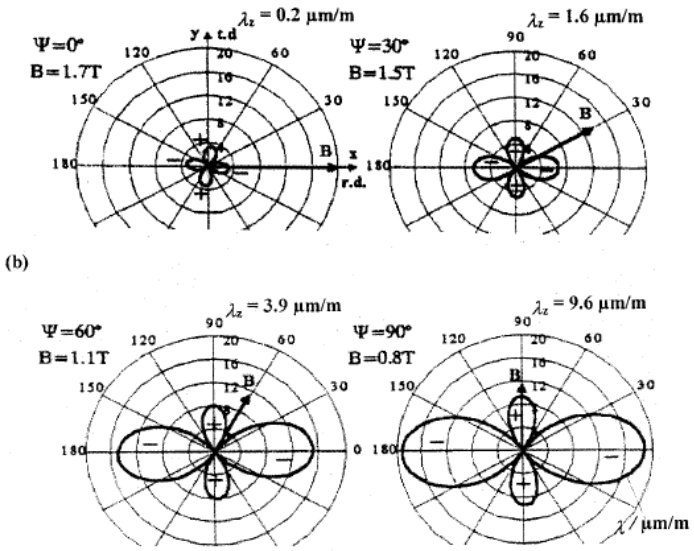

Figure 13 - Magnetostriction in the three space directions for different magnetic flux directions on a highly GO (Grain Oriented) SiFe magnetic sheet. [5]

Out-of-plane deformation can also occur when an out-of-plane magnetic flux travels across the lamination sheets. This happens in correspondence of the joints between vertical limbs and yokes, where air gaps are present and magnetic flux is deviated, as shown in Figure 14.

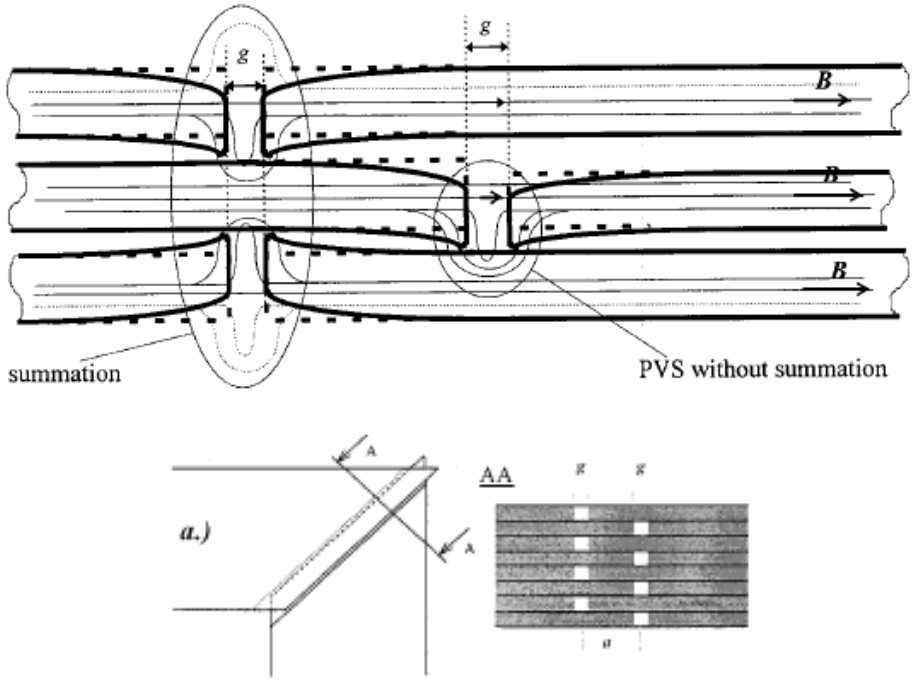

Figure 14 - Magnetic flux deviation in normal direction due to air gaps in correspondence of overlaps [5]

Many researchers have found that magnetostriction is an isochoric process [9] [10] [11], i.e. the deformations in the directions perpendicular to the rolling one are half the deformation in the rolling direction. In other words, the magnetic Poisson ratio is equal to *0.5.* This kind of relation is known as *incompressible magnetostriction* and leads to an important consequence: being A matrix singular (A matrix links magnetostrictive strain components to the square of the magnetic field ones), the principal strains remain constant when changing the direction of the applied magnetic field. However, other researchers have found a different relation between rolling and perpendicular directions. Pfützner et al. have measured different coefficients, for which the considerations made before are not valid anymore. This shows how magnetostriction deserves further experimental investigation still today. Figure 15 shows an example of the measured magnetostriction coefficients in the 2D case linking deformation to magnetic field, where the first row refers to the deformation in rolling direction and the second row refers to the deformation in the transverse one.

$$A = \begin{bmatrix} 1 & -2 \\ -0.5 & 1 \end{bmatrix} \qquad A = \begin{bmatrix} 1 & -2 \\ -1 & 1 \end{bmatrix}$$

Figure 15 - Magnetostriction coefficients measured by Baumgartlinger et al. on ZDKH23 electrical steel (left). Magnetostriction coefficients measured by Pfutzner et al. on HiB electrical steel (right) [12]

3.3.2 In plane stress

Many researchers have studied the effect of the application of a pre-stress on magnetostriction. It has been found that compressive stress in the rolling direction or tension in the transverse one increase magnetostriction and consequently noise radiation. Mizokami and Kurosaki [13] performed a magnetostriction test on a single sheet (500 mm x 100 mm) under compressive stress from 0 to 3 MPa. Two different materials have been used, CGO (conventional grain oriented) and HGO (high permeability grain oriented). It has been found that an increase of compressive stress in the rolling direction leads to an increase of 0-to-peak magnetostriction. In addition, a noise test in anechoic room has been performed on a real 3-phase 3-limbs transformer, where the compressive stress was

controlled through springs located in correspondence of the vertical clamps, and the same behavior was found, with increasing noise for increasing compressive stress, as shown on Figure 16.

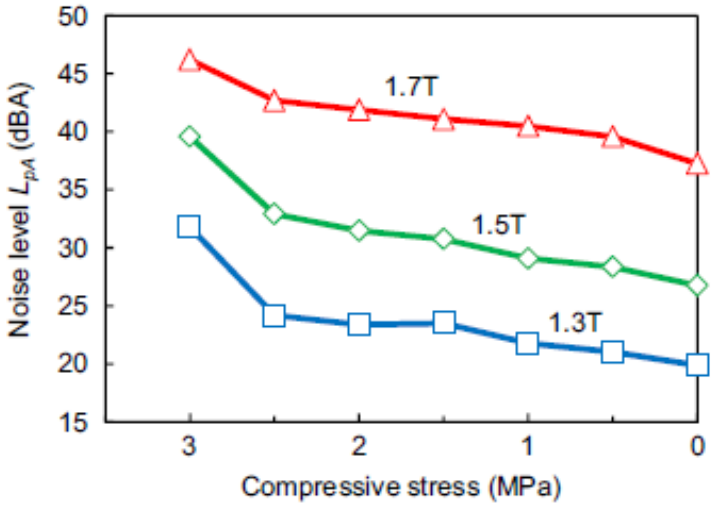

Figure 16 - a) HGO at 1.3 T. b) CGO at 1.3 T. c) HGO at 1.7 T. d) CGO at 1.7 T (left). Relation between noise level and compressive stress (right) [13].

Moses et al. [14] found similar results about magnetostriction of a commercial grain oriented electrical steel (GOSI) under compressive stress, also investigating the beneficial effects of coatings. A step-like curve is obtained, as shown on Figure 17. Similar results regarding compressive stress in rolling direction and application of coating have been found by Anderson et al. [15].

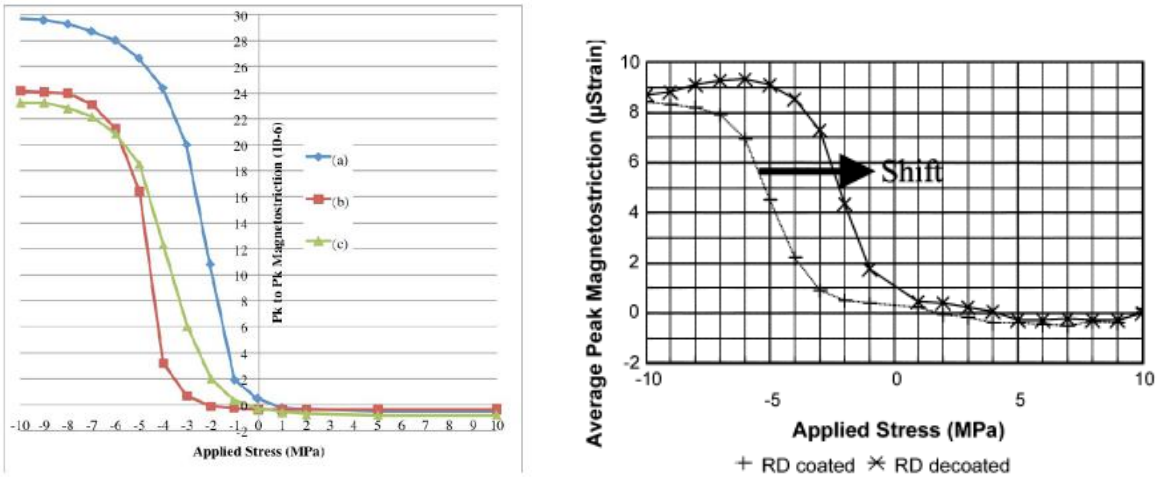

Figure 17 – Effect of stress on typical GOSI a) uncoated. b) high stress coating. c) standard coating (left) [14]. Magnetostriction as function of stress applied in rolling direction (right) [15].

Holt and Robey [16] showed the influence of normal pressure generated by clamps on magnetostriction. When assembling the core, laminations are kept together by means of bolts tightened with a certain torque, exerting a pressure normal to the laminas planes. The results they obtained show that normal pressure has a smoothing effect on the step-like curve representing magnetostriction as a function of compressive stress in rolling direction. At low compressive stress, a

normal pressure increases magnetostriction while at higher compressive stress the contrary occurs, as shown on Figure 18.

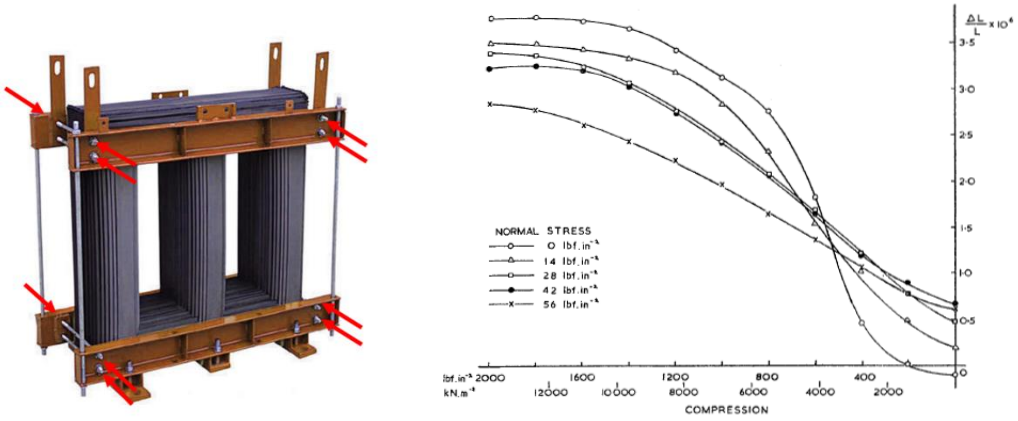

Figure 18 – Application of normal pressure (left) and Influence of longitudinal and normal stress on magnetostriction (right) [16]

3.3.3 Annealing

Some researchers have studied the effects of thermal treatment on electrical steel magnetostriction. Foster and Reiplinger [17] found that annealing of M5 grade GOSI laminations at 780 °C produces positive peak-to-peak magnetostriction, while annealing at 850 °C produces negative peak-to-peak magnetostriction, as shown in Figure 19. This leads to a modification of the harmonic content of the emitted noise, as shown in Figure 20.

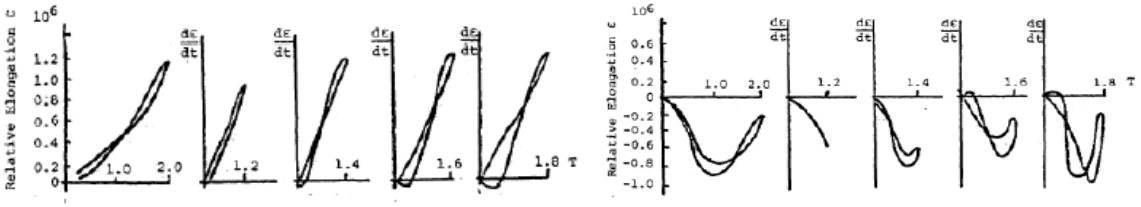

Figure 19 - Positive peak-to-peak magnetostriction for 780 °C annealing (left), negative peak-to-peak magnetostriction at 850 °C annealing (right) [17]

Sample		Frequency Hz						L_{total}	
		100 n = 1	200 n = 2	300 n = 3	400 n = 4	500 n = 5	600 n = 6	C	A
	$n(\epsilon_n x 10^6)$	1.35	0.735	0.265	0.059	0.059	0.09		
I	L_n dB	81.8	76.5	67.7	54.5	54.5	58.1	83	
	L_n dB(A)	62.7	65.7	61.2	49.7	51.3	56.2		69
	$n(\epsilon_n x 10^6)$	0.96	0.23	0.2	0.075	0.023	0.06		
II	L_n dB	78.8	66.4	65.2	56.9	46.4	54.9	79.5	
	L_n dB(A)	59.7	55.6	58.7	52.1	43.2	53		63.5
	$n(\epsilon_n x 10^6)$	0.49	0.99	0.085	0.24	0.1	0.112		
III	L_n dB	73.1	79.1	57.8	66.8	59.1	60.2	80.5	
	L_n dB(A)	54.0	68.3	51.3	62.0	55.9	58.3		70

Figure 20 - Harmonic content of the emitted noise for different magnetostriction curves. I (only positive magnetostriction), II (both positive and negative magnetostriction), III (only negative magnetostriction)

3.4 Clamping torque and normal pressure

In order to keep the lamination stack together, clamps are used. The typical clamps are composed by tightening rods passing through core holes and tightened through nuts. In this way, a pressure perpendicular to the laminations is applied, as already shown in Figure 18. The clamping torque affects noise emission, but the involved mechanism is still not clear. Researchers experimentally found that an optimal value of the clamping torque and so of the clamping pressure can be found. In table 1 some experimental results are shown [18]. Ishida et al. [19] conducted experimental tests measuring the noise level at different pressures applied to the yoke. The trend shown on Figure 21 is not monotone and an optimal value can be found.

Table 1 - Noise measurements (dBA) for different clamping torques at 50 Hz current. [18]

	1.0 T			1.5 T			1.7 T		
Torque/Position	#1	#3	#9	#1	#3	#9	#1	#3	#9
2 Nm	39.9	38.5	36.0	43.3	46.8	40.1	50.3	53.6	46.9
4 Nm	40.4	38.9	35.8	43.4	46.9	39.2	48.9	52.2	46.1
6 Nm	40.3	38.3	36.9	44.8	48.1	42.7	50.5	53.7	47.8

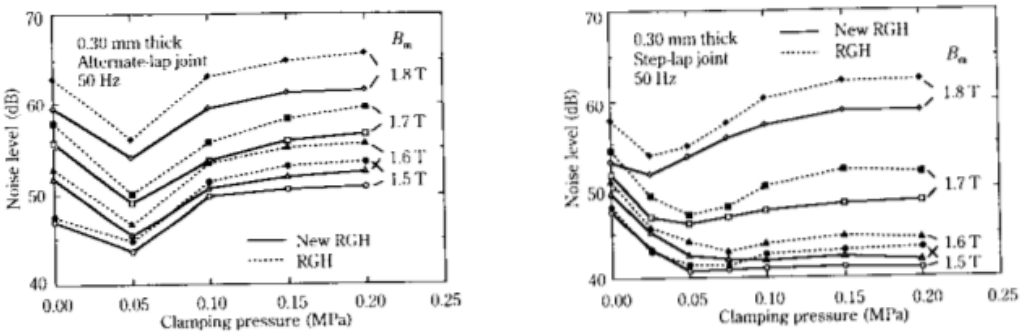

Figure 21 - Influence of clamping pressure on the yoke [19]

3.5 Overlapping techniques in yokes-columns joints

Another important parameter influencing noise radiation is the overlapping technique used to connect the core columns to the yokes. Multi-step-lap technique revealed to be a better choice with respect to single-step-lap technique, leading to minor noise radiation [5] [18]. The two different joint techniques are shown on Figure 22 and Figure 23. Also, the free length of the steel sheet coming out from the core affects noise emission: the longer this is, the higher the vibration and the higher the noise radiation.

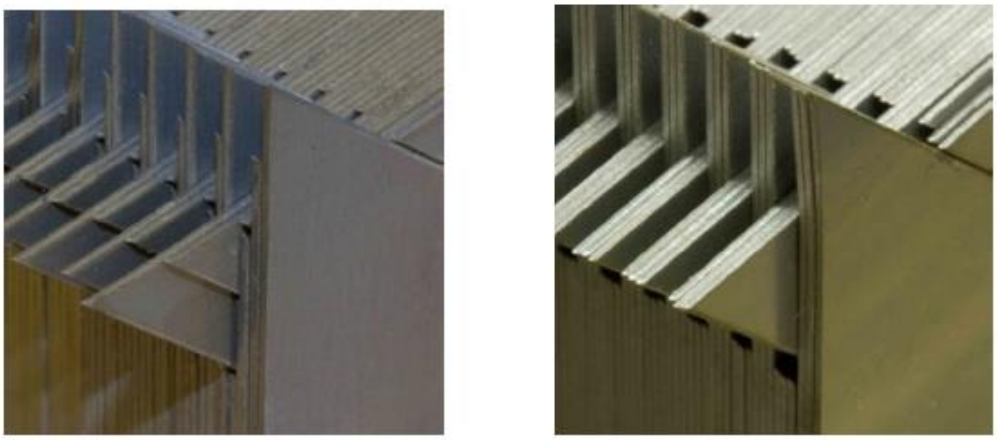

Figure 22 - multi-step-lap (left) and single-step-lap (right) [18]

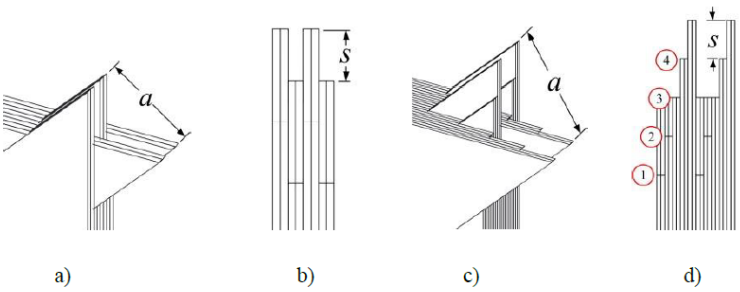

Figure 23 - step-lap (a and b) and multistep-lap (c and d) [18]

4. Noise quantities and measurements

When measuring transformers noise, different techniques and different quantities are available. The three quantities of interest are Sound Pressure, Sound Intensity and Sound Power. Sound Power must be measured indirectly starting from Sound Intensity or Sound Pressure. The different quantities can be measured by means of *walk around* or *point-to-point* techniques. For *walk around* techniques, the operator walks around the source carrying a microphone. A velocity of *0.5 m/s* or lower should be used. The microphone should be mounted on a boom to reduce step noise and cables should be fixed to avoid them to move. Robots can be used to increase measurement quality. For *point-to-point* techniques, microphones are located around the source and then the test is started. A maximum spacing of 1 meter between the microphones should be used [1].

Since the pressure of audible sound ranges from $20\ \mu Pa$ to $20\ Pa$, decibel scale is used, which allows to plot data in a more readable way. Moreover, the A-weighting is applied to measurement to relate the emitted physical sound to the sound perceived by human beings. In fact, human ears act as filters, attenuating out frequencies below 1 KHz or above 3 KHz. Figure 24 shows the A-weighting curve, containing the correction to apply to the measured sound pressure level in order to obtain the perceived one by human beings.

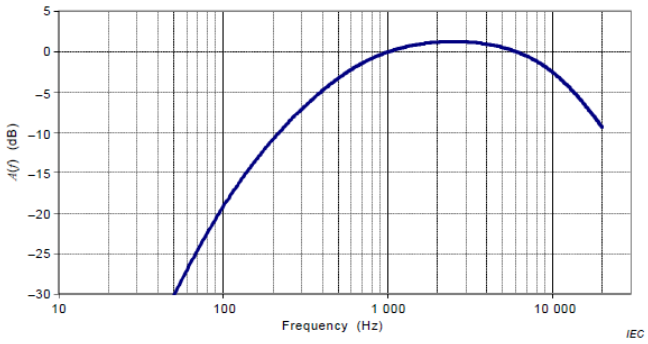

Figure 24 - A-weighting [1]

4.1 Sound pressure

Sound Pressure is defined as the root mean square of the instantaneous pressure perturbation over a time interval. This is a scalar quantity which doesn't take into account the direction of the sound waves and is measured using one single microphone. Figure 25 shows an example of sound pressure microphone. For this reason, Sound Pressure measurements are affected by reflections, background noise, standing waves and near field effects, each of them leading to an overestimation of the Sound Pressure. Background noise and reflection noise have to be measured and they have to be lower than a threshold according to regulations. If this threshold is exceeded, corrections must be applied.

Measurements of Sound Pressure should be performed at a distance of 0.3, 1 or 2 meters from the transformer surfaces [1]. This is a trade-off between signal-to-noise ratio and minimization of near field and P.I. index, which will be discussed later. When measuring noise emitted by forced cooling system, instead, a distance of 2 meters should be used to minimize the effects of turbulence. Sound Pressure Level, i.e Sound Pressure in decibel scale is defined as follows, where p_0 is conventionally taken equal to the minimum audible pressure ($20\ \mu Pa$). Sound Pressure Level in the far-field decreases by 6 dB for doubling distance from the source.

$$L_p = 20 \log_{10}\left(\frac{p_{rms}}{p_0}\right)\ [dB]$$

Figure 25 – Example of Sound Pressure microphone

4.2 Sound intensity

Sound Intensity is defined as the time averaged product of the instantaneous sound pressure and the instantaneous particle velocity in a specific point of the space.

$$\boldsymbol{I} = \frac{1}{T}\int_T \big(p(t)\boldsymbol{v}(t)\big)dt$$

It is a vectorial quantity which considers the direction of the sound wave and for this reason two microphones separated by a spacer are needed to measure it. Figure 26 shows an example of sound intensity probe. The particle velocity is indirectly measured making use of conservation of momentum applied to fluids, i.e. it is calculated as the gradient of pressure between the two microphones. The final expression of the Sound Intensity component parallel to the distance between the two measuring microphones is the following

$$I = -\frac{p_A + p_B}{2\rho} \int \left(\frac{p_A - p_B}{\Delta r}\right) dt$$

where Δr is the distance between the microphones. Since Sound Intensity takes into account the direction of emitted noise, it is not affected by reflections (radiated and reflected sound can be distinguished) or background noise as far as the mean pressure $\frac{p_A+p_B}{2}$ is negligible compared to the pressure gradient. The P.I. index is used to understand if this is the case or not. It is defined as the difference between the uncorrected Sound Pressure Level (which contains disturbances) and the intensity of the sound propagating from the source alone. If P.I. index is greater than 4 dB, Sound Intensity will be excessively underestimated. Sound Intensity is not affected by near-field effects, since active and reactive sound fields can be distinguished based on the information available on pressure and particle velocity: active Sound Intensity is the product of acoustic pressure and the in-phase component of the particle velocity, while reactive Sound Intensity is the remaining part. Knowing the phase between pressure and particle velocity, active and reactive sound can be distinguished. On the other side, Sound Intensity is affected by standing waves. If standing waves are present, pressure and particle velocity are out-of-phase and Sound Intensity becomes null. In the far-field, where pressure and particle velocity are assumed to be in-phase, Sound Intensity Level equals Sound Pressure Level.

Figure 26 - Sound intensity probe

4.3 Sound power

Sound Power is defined as the integral of the component I_n of sound intensity normal to a surface enclosing the source. It is independent on the distance from the source. Once Sound Intensity has been measured on a surface enclosing the source, Sound Power can be computed as follows. No reflecting or absorbing objects must be present inside the enclosing surface.

$$W = \int_S I_n \ ds$$

Sound Power Level, which is defined at the end of this paragraph, can be calculated also from Sound Pressure Level measurements according to the following equation [21], where L_p is the Sound Pressure Level, S is the area of measurement surface and S_0 is equal to $1\ m^2$.

$$L_w = L_p + 10\log_{10}\left(\frac{S}{S_0}\right)$$

According to standards [20] [21], the measurement surface should be a parallelepiped if measurements are performed manually, and each surface composing this parallelepiped should be a rectangle. The minimum distance from the source should be 0.25 m and no absorbing surfaces should be present inside the measurement surface. Reflecting surfaces such as floor or walls can be incorporated but measurement shall not be made on these surfaces, nor their areas included in the evaluation of the source power. A hemispherical measurement surface with a radius at least twice the characteristic length of the source can be also selected, but this is not suggested for manual measurements.

The difference between Equivalent Radiated Power and Sound Power is also worth to be mentioned. Equivalent Radiated Power (ERP) is a measure of the acoustic power generated by the vibrating surface, and is defined as follows, where ρ indicates the air density, c the sound speed, A the radiating surface area and $< v_n^2 >$ the surface averaged mean square velocity.

$$ERP = \rho c A < v_n^2 >$$

Sound Power is the actual power transmitted to the fluid and is defined as follows, where W_0 is conventionally taken equal to $10^{-12}\ W$.

$$L_w = 10\log_{10}\left(\frac{W}{W_0}\right)\ [dB]$$

It depends on the radiation efficiency, which can be defined as the ratio between Sound Power and Radiated Power. Radiation efficiency depends on the source vibration frequency. For frequencies next to or above coincidence frequencies of the source (winding, core or frame's elements), radiation efficiency increases rapidly. Coincidence frequency is the frequency at which the wavelength of the bending deformation of a structure is equal to the wavelength of the generated sound. When the

coincidence frequency is approached and overcame, radiation efficiency increases rapidly. The higher the radiation efficiency, the larger the power delivered from the source to the air. Figure 27 illustrates the concept of coincidence frequency. λ is the sound wavelength, λ_s is the structural bending wavelength, θ is the sound radiation angle. The dots indicate air particles and the bolded line on the right indicates the vibrating panel.

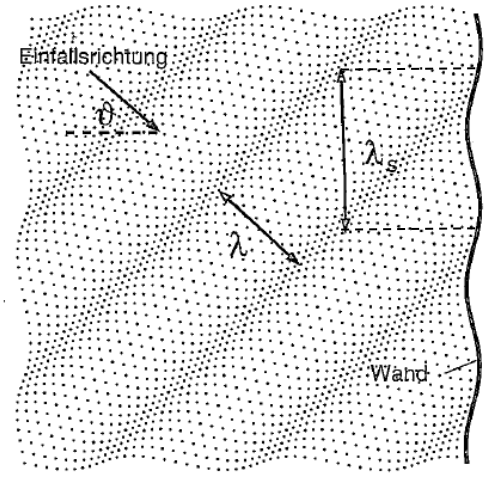

Figure 27 - Concept of coincidence frequency.

4.4 Standards

Some of the requirements from regulations (UNI EN ISO 3744-2009, NEMA ST 20-2014, IMO and IMCO codes for ships) are here reported. Regulations suggest measurement techniques and impose limits to the measurement inaccuracies and to noise emission. UNI EN ISO 3744-2009 [21] provides 3 different levels of measurement accuracy. For each of them, the following parameters must be lower than a threshold.

- ΔL -> Difference between the average Sound Pressure Level L_p measured on the measurement surface and the background Sound Pressure Level. For a very accurate measurement (grade 1) it has to be higher than 10 dB.

$$\Delta L = L_p - L_{background}$$

- K_1 -> *Background correction factor*, calculated according to the following formula, must be lower than 0.4 dB for a grade 1 measurement. It must be subtracted to the measured Sound Pressure. Background noise should be measured before and after the test phase.

$$K_1 = -10 \log_{10}\left(1 - 10^{-0.1\Delta L}\right) dB$$

- K_2 -> *Environment correction factor*, calculated according to the following formula, must be lower than 0.5 dB for a grade 1 measurement. S denotes the area of the measurement surface while A denotes the equivalent absorption area, which can be computed as $A = \alpha \cdot S_{room}$, i.e. the product between the mean absorption coefficient and the surface of the test room.

$$K_2 = 10 \log_{10}\left(1 + 4\left(\frac{S}{A}\right)\right) dB$$

  The higher the absorption coefficient, the lower K_2 and the more accurate the measurement. On the other side, the higher K_2, the higher the reflection of the testing room and the higher the measurement error.

- σ_R -> *Standard deviation*, has to be lower than 1 dB for a grade 1 measurement. Repeatability is a critical aspect for transformer noise measurement. Experience shows that nominally

identical transformer can have up to 10 dB difference in noise measurement due to manufacturing deviations.

NEMA ST 20-2014 [22] provides a table reporting the audible sound (dBA) thresholds applied to transformers for different input power, measured at 1 foot distance from the transformer. The table is shown in Figure 28.

Table 3.9
AVERAGE SOUND LEVEL

	Average Sound Level, Decibels			
	SELF COOLED VENTILATED			SELF COOLED SEALED
	A	B	C	D
Equivalent Winding kVA Range	K Factor = 1 K Factor = 4 K Factor = 9	K Factor = 13 K Factor = 20	Forced Air When Fans Running	
3.00 and below	40	40	67	45
3.01 to 9.00	40	40	67	45
9.01 to 15.00	45	45	67	50
15.01 to 30.00	45	45	67	50
30.01 to 50.00	45	48	67	50
50.01 to 75.00	50	53	67	55
75.01 to 112.50	50	53	67	55
112.51 to 150.00	50	53	67	55
150.01 to 225.00	55	58	67	57
225.01 to 300.00	55	58	67	57
300.01 to 500.00	60	63	67	59
500.01 to 700.00	62	65	67	61
700.01 to 1000.00	64	67	67	63
Greater than 1000	Consult Factory			

Note 1: Consult factory for non-linear requirements exceeding a K-factor rating of 20.
Note 2: When the fans are not running columns A & B apply
Note 3: Sound levels are measured using the A-weighted scale (dB (A))

Figure 28 - Noise emission threshold (dBA) from NEMA ST 20-2014

IMO 468-IS [23] and IMCO Code [24] specify the maximum Sound Pressure Level acceptable in different ships spaces, measured at a distance of 1 meter from the source, greater than 0.5 meters from the room walls and between 1.2 – 1.6 meter from the deck. These specifications are shown on Figure 29. It can be noticed that the lowest noise is required for the most critical rooms such as radio rooms or cabins and hospitals, where communication clearness is fundamental.

4.2 Noise level limits

Limits for noise levels are specified for various spaces as follows:

4.2.1	***Work spaces*** (see 5.1)	***dB(A)***
.1	Machinery spaces (continuously manned)**	90
.2	Machinery spaces (not continuously manned)**	110
.3	Machinery control rooms	75
.4	Workshops	85
.5	Non-specified work spaces**	90
4.2.2	***Navigation spaces***	***dB(A)***
.1	Navigating bridge and chartrooms	65
.2	Listening post, including navigating bridge* wings and windows	70
.3	Radio rooms (with radio equipment operating but not producing audio signals)	60
.4	Radar rooms	65
4.2.3	***Accommodation spaces***	***dB(A)***
.1	Cabins and hospitals	60
.2	Mess rooms	65
.3	Recreation rooms	65
.4	Open recreation areas	75
.5	Offices	65

4.2.4	***Service spaces***	*dB(A)*
.1	Galleys, without food processing equipment operating	75
.2	Serveries and pantries	75
4.2.5	***Normally unoccupied spaces****	*dB(A)*
	Spaces not specified (see 5.1)	90

Figure 29 - Sound Pressure Levels limits in different ships spaces according to IMO 468-IS

4.5 Specifications

Specifications indicate the customer requirements in terms of measurement techniques and admissible noise emissions. Some examples are here reported in order to give more insight on how requirements are specified. *Fincantieri* requires the airborne noise level of transformers to be measure both during workshop test and on board at 1 meter distance from the source surfaces. Sound Pressure Level must not be greater than 68 dBA. Requirements are provided also in terms of structure-borne noise, for which the mean vibration velocity measured below the elastic insulators (on ship foundation) must be lower than the specified values reported below, where a reference velocity of 10^{-9} m/s is used. Figure 30 shows an example of experimental setup for measuring foundation structure-borne noise and the specified vibration velocities from Fincantieri.

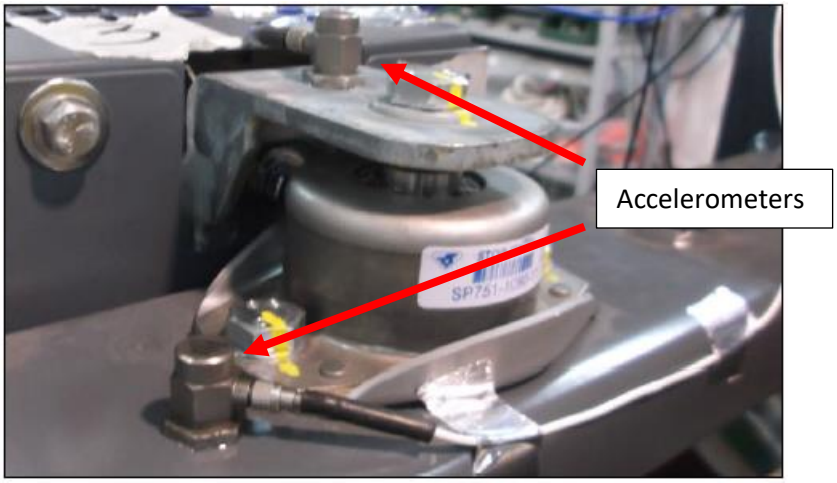

f (Hz)	31.5	63	125	250	500	1K	2K	4K
Lv (dB)	105	102	102	99	93	87	81	75

Figure 30 – Structure-borne noise measurement technique and specified vibration velocity from Fincantieri. Reference velocity = 10^{-9} m/s

Hitachi Rail requires the Sound Pressure Level to be lower than a limit for different operative conditions. When the train is stationary, the arithmetic mean of the Sound Pressure Level must be lower than the values specified by the Noise Rating curve 55 (NR 55). When the train is running at speeds below 50 kph, Preferred Speech Interference Level (PSIL) must be lower than 57 dB in each saloon. When the train is running at speeds between 50 kph and 125 mph the PSIL must be within the range 50-57 dB. When the train is running at speed above 125 mph the arithmetic mean of the measured Sound Pressure Level must be lower than the values specified on Figure 31.

Sound pressure level dB(Lin)								
31.5 Hz	63 Hz	125 Hz	250 Hz	500 Hz	1 kHz	2 kHz	4 kHz	8 kHz
93	84	77	70	64	58	52	48	46

Figure 31 - Hitachi Rail specifications at speeds above 125 mph

5. *Introduction to the methodology*

The following chapter illustrates the methodology adopted for the realization of a multi-physic FE analysis capable to predict noise emissions of a transformer, starting from the numerical computation of electromagnetic forces up to the noise emission to the far-field. The two main sources of transformer noise, load noise and core noise, are considered here. Tank noise, which is the noise generated by the vibration of the tank containing the transformer and filled with oil, is not considered in this work. The modelling choices are driven by the need of obtaining accurate results as well as an easy and fast modeling, in order to integrate the methodology into an automation to be used by Engineering. The two sources of noise, load noise and core noise, are modeled.

Load noise is generated by winding vibration, excited by the application of Lorentz forces. As already mentioned, these forces appear due to the interaction of the magnetic field with the current density inside the winding. When modeling load noise, one important aspect has to be faced: the real winding is composed by several materials (conductor, paper, adhesive tape, covering mat, resin). To improve computational efficiency and modeling time, the winding has to be homogenized, passing from the real multiphase one to a winding considered as made of one single isotropic material, as shown on Figure 35. This is also a diffused solution in literature [25]. Moreover, this speeds up the procedure allowing the user to avoid the modification of CAD drawings coming from mechanical designers, in which the winding is always represented as homogenized. Winding homogenization leads to one challenging question to be answered:

- Which mechanical properties must be assigned to the homogenized winding material in order to reproduce the same mechanical dynamic behavior as the real winding, computing the same emitted noise?

Core noise is generated by two mechanisms inside the core: magnetostriction and Maxwell forces. As already mentioned, magnetostriction is a peculiar characteristic of ferromagnetic materials, in which applying a magnetic field, deformations occur. These deformations generate dynamic forces into the core laminas leading to the generation of vibrations and noise. Maxwell forces, instead, are surface forces concentrated at the free surfaces of the core, where material discontinuities are present. Transformer's core is composed of several packaged laminas. Modeling all the laminas is unpractical from both modeling and computational time points of view, since very fine mesh and hundreds of contacts would be present. For this reason, the core must be modeled as a monolithic solid. This leads to two challenging questions to be answered:

1. How big is the difference between a monolithic core and a laminated one from the electromagnetic point of view?

2. How big is the difference between a monolithic core and a laminated one from the structural point of view?

In order to understand the basics of acoustics modeling, several preliminary studies on analytical acoustic models, i.e. Monopole and Dipole models, have been performed. These studies are presented in the Appendix. These simple models give the possibility to clarify how to model acoustic far-field and how different modeling choices like acoustic domain size, PML (Perfectly Matched Layer non-reflecting boundary condition) region size, number of PML layers and mesh size affect the results, giving a guideline and some rule of thumbs for constructing the final acoustic model.

5.1 Used softwares

The adopted approach is that of a multi-physic simulation, in which electromagnetic, structural and acoustic finite element simulations are coupled. The following list shows the software used for the different steps.

- *Creo 4.0*: geometry creation;
- *Ansys Design Modeler*: geometry defeaturing;
- *Ansys Maxwell*: electromagnetic analysis;
- *Ansys Mechanical*: structural and acoustic analysis.

The Ansys Workbench environment is used for transferring data and results (like importing the loads) between different simulations, and to make use of parametrization to modify modeling variables in a fast and user-friendly way.

5.2 Theoretical formulation

In the following paragraph a detailed theoretical description of the methodology adopted for computing the noise emission of transformers is presented. Electromagnetic dynamic forces (Lorentz, Maxwell and magnetostrictive forces) are computed through electromagnetic simulations in Ansys Maxwell. These forces are mapped onto the structural model representing the structural excitation, vibration velocities are then computed. These velocities are mapped onto the acoustic model representing the acoustic excitation. Acoustic far-field quantities are then finally computed. The workflow is reported on Figure 32. The One-way coupling technique is adopted, which means that no feedback between the different simulations is adopted.

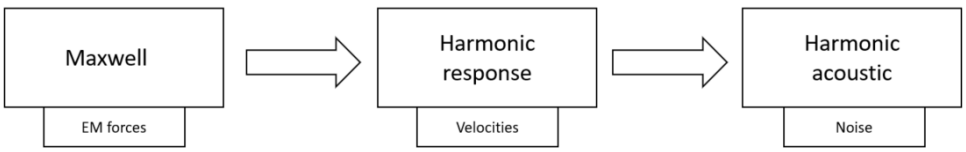

Figure 32 - Schematic of acoustic analysis workflow

Winding forces and core forces are computed using two different electromagnetic models. Winding forces are computed through an Eddy Current analysis (harmonic EM analysis) whereas core forces through a transient analysis. This separation leads to higher accuracy and will be clarified later. The forces coming from the two different models are then imported in the same mechanical model of the full transformer and interpolated onto the relevant component (Lorentz forces onto the winding, core forces onto the core).

5.2.1 Electromagnetism

5.2.1.1 Load noise – winding forces

In the context of load noise, the transformer's component of interest is the winding. The mechanism which generates winding vibration and consequently winding noise is related to Lorentz forces. Winding is travelled by current which generates a magnetic field, according to the Maxwell differential Equations 1 and 2. The interaction between current density and magnetic field generates the so-called Lorentz forces, according to Equation 3. $\boldsymbol{A}$ is the magnetic potential vector $[\frac{V\,s}{m}]$, $\boldsymbol{J}$ is the current density $[\frac{A}{m^2}]$, $\boldsymbol{B}$ is the magnetic flux density, μ is the magnetic permeability $[\frac{H}{m}]$, σ is electric conductivity $[\frac{S}{m}]$, $\boldsymbol{F}$ is the volumetric density of Lorentz forces $[\frac{N}{m^3}]$. $\boldsymbol{A}, \boldsymbol{J}, \boldsymbol{B}, \boldsymbol{F}$ are space and time dependent quantities.

$$\boldsymbol{\nabla} \times \left({}^{1}/_{\mu}\, \boldsymbol{\nabla} \times \boldsymbol{A}\right) + \sigma \frac{\partial \boldsymbol{A}}{\partial t} = \boldsymbol{J} \qquad (1)$$

$$\boldsymbol{B} = \boldsymbol{\nabla} \times \boldsymbol{A} \qquad (2)$$

$$\boldsymbol{F} = \boldsymbol{J} \times \boldsymbol{B} \qquad (3)$$

Developing Equation 3, it can be easily seen that Lorentz forces depend on the square of the current. This means that Lorentz forces magnitude depends quadratically on the current intensity and Lorentz forces frequency is double the current one.

5.2.1.2 Core noise - Core forces

In the context of core noise, the component of interest is the core. The mechanisms which generate core vibration and consequently core noise are related to magnetostriction and Maxwell forces.

Magnetostriction is described by a non-linear hysteretic curve linking deformation to magnetic field, known as butterfly curve due its shape. An example is shown on Figure 10. Analytically, magnetostrictive strain λ depends on the magnetic field strength H by a polynomial in which only even powers are present, which means that magnetostriction has a fundamental harmonic at double the frequency of H plus higher even harmonics. For some electrical steels, magnetostriction is also characterized by a change of the deformation sign during the cycle. Also, magnetostriction is in general anisotropic (transversely isotropic), which means that the constitutive law is different in the rolling and in the transverse directions. Deformations in rolling direction are higher than in transverse. Equation 4 and Equation 5 show how magnetostriction can be expressed analytically, where *x* denotes the rolling direction while *y* and *z* denote the transverse directions.

$$\lambda_x = \sum_i \alpha_i H_x^{2i} + \beta_i H_y^{2i} + \gamma_i H_z^{2i} \qquad (4)$$

$$\lambda_y = \sum_i \phi_i H_x^{2i} + \omega_i H_y^{2i} + \epsilon H_z^{2i} \qquad (5)$$

The hypothesis of isochoric magnetostriction (or incompressible magnetostriction) is assumed by Ansys [26]: the deformation in the transverse directions is supposed to be equal to *-0.5* the deformation in the rolling one. The consequence is that only two curves are needed to completely define magnetostriction: one describing the deformation in rolling direction due to a magnetic field in rolling direction and the other describing deformation in transverse directions due to a magnetic field in transverse direction. The cross couplings are automatically determined applying the hypothesis of isochoric magnetostriction. The two-way coupling between magnetostriction and mechanical stress is

neglected to simplify the procedure. Future work adopting the two ways coupling technique will be done for confirming this assumption.
The calculation of magnetostrictive forces performed in Ansys deserves a brief illustration. Magnetostrictive forces are computed and interpolated on structural nodes as follows. Magnetic field strength *H* is extrapolated from the *B-H* curve after having computed the magnetic flux density *B*. Figure 33 sows an example of the *B-H* curve to be used in Ansys.

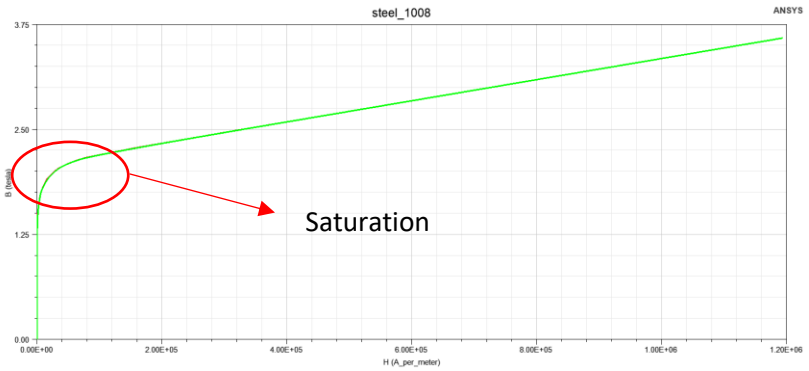

Figure 33 - redefined B-H curve for Steel 1008 in Ansys Maxwell

After having extrapolated the value of *H,* magnetostrictive strains are extrapolated from magnetostriction curve ($\lambda - H$ curve is defined by the in Ansys by the user). Knowing the strain of each element, the volumetric magnetostrictive nodal forces can be computed integrating the mechanical stress generated by magnetostrictive deformations, as shown in Equation 6 [27], where A^T is the derivative matrix which links element deformation to nodal displacement in the context of Finite Element approximation (usually denoted with letter *B* in textbooks), C is the elasticity tensor, λ is the magnetostrictive stress vector. This is a similar procedure to the one used to calculate thermal hyperstatic stresses starting from thermal deformations.

$$\boldsymbol{f}_{ms}^{v} = \int A^T C\, \boldsymbol{\lambda}\, dV \qquad (6)$$

Maxwell forces instead can be computed starting from Maxwell stress tensor, which is defined in Equation 7 [26] and expresses the Maxwell forces as a stress status acting on an ideal cube of material. Volumetric magnetic forces can be then computed as shown in Equation 8, i.e as a variation of the Maxwell stresses and consequently as a variation of the magnetic field.

$$\bar{S} = \frac{1}{\mu_0}\begin{bmatrix} B_x^2 - B^2/2 & B_xB_y & B_xB_z \\ B_xB_y & B_y^2 - B^2/2 & B_yB_z \\ B_xB_z & B_yB_z & B_x^2 - B^2/2 \end{bmatrix} \qquad (7)$$

$$\boldsymbol{f}_{\alpha}^{V} = \sum \frac{\partial}{\partial x_\beta} S_{\alpha\beta} \qquad (8)$$

Looking at Equation 6 and Equation 8, it is clear that magnetostrictive and Maxwell volumetric forces concentrate at regions where higher magnetic field variations occur, i.e. at regions where material discontinuities are present (interfaces between core stacks and air gaps and between core laminas).

$\boldsymbol{f}_{\alpha}^{V} = \sum \frac{\partial}{\partial x_\beta} S_{\alpha\beta}$

5.2.2 Structure

Once the electromagnetic forces have been computed in Maxwell, they can be interpolated on the structural model, each of them on the relevant part. The mechanical response of the structure subjected to electromagnetic forces can be computed according to Equation 9, where M, C, K are the mass, damping and stiffness matrices respectively, $\boldsymbol{u}$ is the displacement vector, $\boldsymbol{F_{Lorentz}}$, $\boldsymbol{F_{ms}}$, $\boldsymbol{F_{Maxwell}}$ are Lorentz, magnetostrictive and Maxwell nodal forces vectors respectively.

$$M\frac{\partial^2 \boldsymbol{u}}{\partial t^2} + C\ \frac{\partial \boldsymbol{u}}{\partial t} + K\boldsymbol{u} = \boldsymbol{F_{Lorentz}} + \boldsymbol{F_{ms}} + \boldsymbol{F_{Maxwell}} \qquad (9)$$

5.2.3 Acoustics

Once the vibration velocities of the structural nodes are computed, they can be imported into the acoustic model, representing an excitation for the air domain which leads to pressure variations. Formally, knowing the structure velocities and making use of Equation 10, expressing the linearized momentum equation with hypotheses of non-viscous fluid, it is possible to compute the pressure of the air at the interface between the vibrating body and the fluid domain.

$$\rho\frac{\partial v_n}{\partial t}|_{\boldsymbol{x}=interface} = -\frac{\partial p}{\partial n}|_{\boldsymbol{x}=interface} \quad (10)$$

This is then used as a Neumann boundary condition for the wave Equation 11.

$$\nabla^2 p = \frac{1}{c^2}\frac{\partial^2 p}{\partial t^2} \qquad (11)$$

$\rho\frac{\partial v_n}{\partial t}|_{\boldsymbol{x}=interface} = -\frac{\partial p}{\partial n}|_{\boldsymbol{x}=interface}$

Here p denotes the sound pressure, c the sound speed, v_n the velocity component normal to the structure surface, x indicates a position in the space. Since the wave equation is a 2nd order partial differential equation both in space and time, another space boundary condition is needed to make the problem well-posed. The 2nd space boundary condition is set at the external boundaries of the acoustic domain. Since the objective of the model is to compute acoustic quantities in the far-field region, this boundary condition has to represent a free non-reflecting field. This can be modeled making use of PML (Perfectly Matched Layer) elements at the end of the modeled acoustic domain and imposing on their external face a simple Dirichlet boundary condition, as in Equation 12.

$$p|_{\boldsymbol{x}=domain\_end} = 0 \quad (12)$$

Figure 34 shows how the acoustic domain is modeled. The radiating body is surrounded by an enclosure (radiation space) and the latter is enclosed by PMLs, which absorb the acoustic waves.

The boundary condition in Equation 12 seems not to be a proper choice, since imposing a null pressure means imposing a null impedance, which leads to unwanted wave reflection. Having a discontinuity of impedance, in fact, generates sound waves reflections. The higher the difference between the impedances of the initial and the final medium, the higher the reflection. But PML elements are finite elements whose shape functions are formulated in such a way that acoustic pressure is exponentially damped and absorbed when passing through them. Absorbing most of the energy of the wave, the Dirichlet boundary condition in Equation 12 generates a negligible reflection. The computed sound pressure has the form in Equation 13, i.e. it has a harmonic behavior in the radiation space and an exponentially decaying behavior in the PML region.

$$p(x,t) = e^{ikx}e^{-\frac{k}{\omega}\int^x \sigma_x(x')dx'} \quad (13)\ [28].$$

x denotes the position in the space (*x=0* at the radiating surface), k is the wave number, ω is the angular frequency, σ is a step function whose units is the same of ω and which is zero before the PML region and *1* inside the PML region [28]. The equation can be seen split in two exponential terms: the first one is a pure harmonic function oscillating around zero at any point of the space, the second one is an exponentially decaying function which is zero in the radiation space, i.e. the wave is exponentially attenuated only in the PML region.

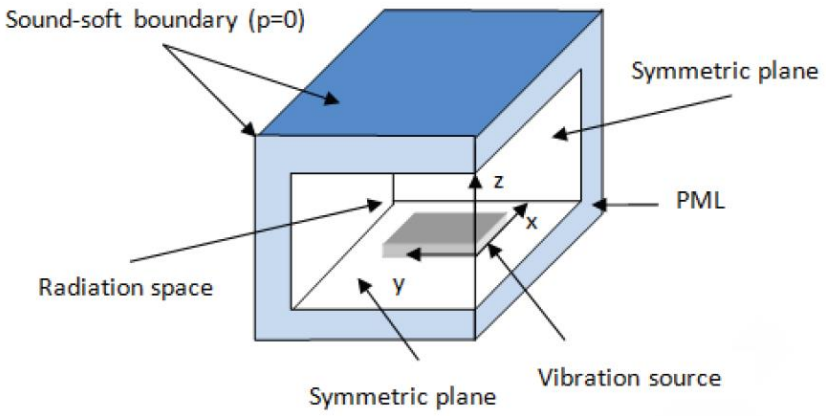

Figure 34 - Acoustic domain modeling [29]

Only the fluid domain is modeled in the acoustic simulation. The structure is not meshed and appears as an empty region in the FE model. The structure surfaces represent reflecting surfaces or exciting surfaces whose velocities are mapped from the results of the previous structural harmonic analysis. This way of modeling assumes that no fluid-structure interaction (FSI) is occurring. The loads generated on the structure by fluid pressure variations are neglected. This assumption can be verified using Equation 14, where ρ_f is the fluid density, c is the sound speed, ρ_s is the density of the structure, t is the characteristic thickness of the structure and ω is the angular frequency of the sound wave.

$$\alpha_c = \frac{\rho_f c}{\rho_s t \omega} \qquad (14)$$

If $\alpha_c < 1$, FSI can be neglected whereas if $\alpha_c > 1$ FSI must be considered. For a traction reactor, α_c is of the order of *0.1,* while for power and distribution transformers it is even lower. Different considerations are valid in the case of tanks, where a FSI must be considered due to the thicknesses of the order of millimeters.

5.2.4 Winding Homogenization

Winding is composed of several materials: conductor, adhesive tape, insulating paper etc. Modeling all the materials explicitly would lead to consistently increasing model size and, consequently, of computational time, due to the small thicknesses of the materials covering the conductor. Also, since only structural displacements are required (stresses are not of interest when dealing with acoustics) and only the global behavior is of interest, having such refined mesh is a waste of resources. For this reason, a homogeneous winding with real dimensions is modeled, in which the whole volume is considered as made of a single isotropic and conductive material. However, the mechanical properties of the homogenized winding material must be chosen in order to have an accurate representation of the real dynamic behavior of the winding and to obtain a negligible error on the computation of the noise emitted in the radial direction, which is the predominant one, due to a winding surface exposed to the radial direction that is much larger than the one exposed to the vertical direction. In other words,

the acoustic power radiated by the winding in the vertical direction is negligible compared to the power radiated in the radial direction, and for this reason the radial deformation is the most important one.

The division in single turns is not needed from the EM point of view nor from the mechanical one. From the EM point of view, a division in turns is needed only if Skin Effect inside the winding is of interest, which is not the case for acoustics. This is better explained in Paragraph 9.1.5. From the mechanical point of view, in the operative situation the winding is a unique body in which the turns are bonded together by cured resin. In conclusion, each section of the winding can be considered as a solid tube, as shown in Figure 36.

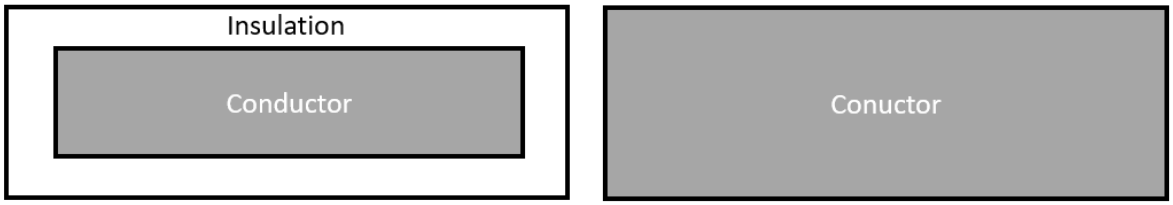

Figure 35 - Real turn cross section (left) vs homogenized one (right)

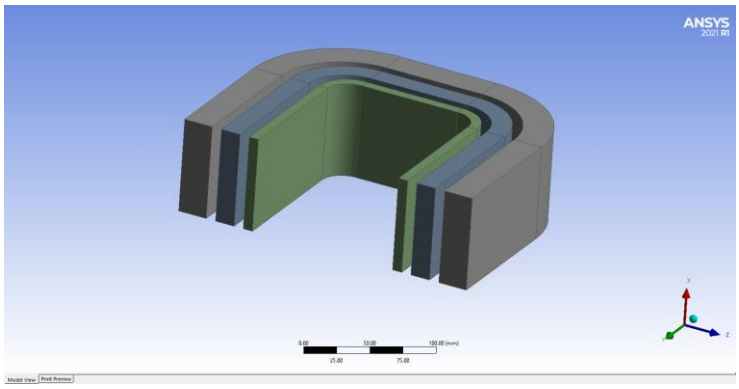

Figure 36 - Homogenized winding

5.2.4.1 Current excitation choice

Current excitation doesn't need any modification when dealing with homogenized winding. A current equal to the real one (datasheet) multiplied by the number of turns must be applied to each section. The reason why a modification of the current is not needed is that to obtain the same resultant Lorentz forces (N), the current must be modified only if the height of the winding is considerably changed with respect to the real one. In fact, a change of the height of the winding leads to a change of the induced magnetic field and consequently to a change of the Lorentz forces. Since this is not the case and the real height is modeled, the current excitation can be set equal to the real one.

5.2.4.2 Winding mechanical equivalent properties

Mechanical winding homogenization is driven by dynamic properties. The mechanical properties of the material assigned to the homogenized winding have to be chosen such that the difference between the Sound Pressure Level emitted in the radial direction by the homogenized winding and that of the real one is smaller than an acceptable error. For doing this, material properties of the homogenized winding can be chosen according to the following procedure, which makes use of a Euler Bernoulli beam model. A complete and detailed explanation of this technique with a worked example is presented in the Appendix 10.1. The reason why a beam model is used to derive mechanical properties

of the winding is that it has been observed that winding turns behave similarly to beams. Figure 37 shows the idea behind this statement. A turn can be seen as an assembly of welded beams.

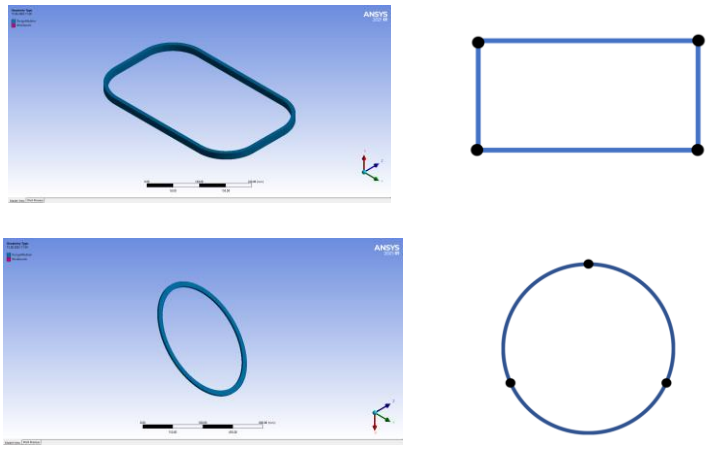

Figure 37 - Winding turn as an assembly of beams

The procedure for computing the equivalent winding material properties can be resumed by the following steps. This applies only to wired winding. Its applicability to foiled winding, i.e. winding composed by foiled sheets of conducting material, will be verified in further developments.

1. A reference beam model with the same cross section and materials of the reference turn is created. All the materials are modeled as shown on Figure 38 and the real material properties are assigned. The length of the beam is chosen equal to 10 times the largest dimension of the cross section, so that Euler-Bernoulli beam theory hypotheses are verified

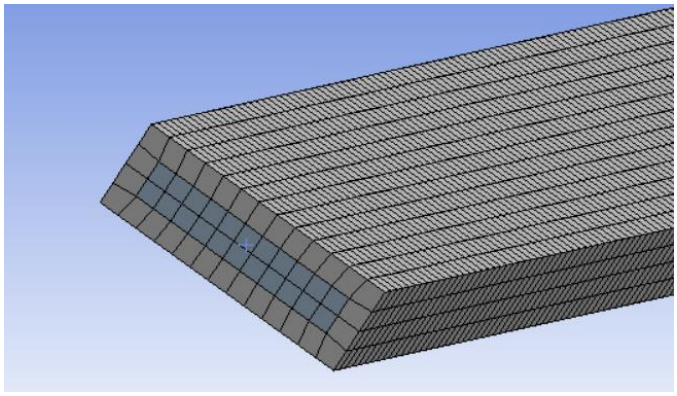

Figure 38 – Beam model with real cross section

2. A modal analysis of the reference beam is performed. The computed eigenfrequencies are used to calculate the Young's modulus of the equivalent homogenized material inverting Equation 15 and Equation 16 [30]. Equation 15 refers to axial modes eigenfrequencies, Equation 16 to bending ones. The user must choose which eigenfrequency to fit. Unfortunately, only one between axial, x-bending and y-bending eigenfrequencies can fit accurately. Choosing to accurately fit one of them, automatically leads to an inaccurate fitting of the eigenfrequencies involving deformation in the other directions. This choice depends on the shape of the winding. The study presented in Appendix shows that for a circular winding, fitting the first axial eigenfrequency leads to the most accurate results in terms of noise emitted in the radial direction compared to a reference model. This is since a circular winding is stretched and compressed by Lorentz forces and the axial stiffness gives the highest contribution to deformation energy. On the other hand, for a rectangular winding, fitting the

bending mode which involves deflection in the radial direction gives accurate results in terms of noise emitted in the radial direction. This is since the sides of a rectangular winding bend under the action of Lorentz forces and so the bending stiffness gives the highest contribution to the deformation in the radial direction. The radial dynamics of the winding is the one of interest since, according to standards, sound power level can be measured from sound pressure measurements performed on a path concentric to the winding, i.e from sound pressures measured in the radial direction.

3. The young modulus E calculated using Equation 15 or Equation 16 is finally assigned to the homogenized winding

$$f = \frac{1}{2}\sqrt{\frac{E}{\rho_{eq} * l^2}} \qquad (15)$$

$$f = \frac{4.73^2}{(2\pi\, l^2)}\sqrt{\left(\frac{EI}{\rho_{eq} A}\right)} \qquad (16)$$

$$\rho_{eq} = \Sigma_i\, \rho_i\, f_i \qquad (17)$$

E is the Young's modulus (the unknown), l is the beam length, A is the total cross-sectional area, I is the second order moment of inertia of the total section, which is chosen as I_x or I_y depending on which direction of the bending mode corresponds to the winding radial direction, ρ_{eq} is the equivalent homogenized material density, calculated using Equation 17, which expresses the rule of mixture, where ρ_i and f_i denote the density and the volumetric fraction of the i^{th} material respectively.

This kind of homogenization technique based on a beam model is needed only for windings whose real cross section is similar to the one on Figure 35, where conductor and insulation are not homogenously distributed on the cross section. If conductor and insulation are homogeneously distributed, as in the case of Figure 39, the rule of mixture can be used for determining the equivalent Young's modulus. This is the case of winding with stranded wires, typical of power transformers.

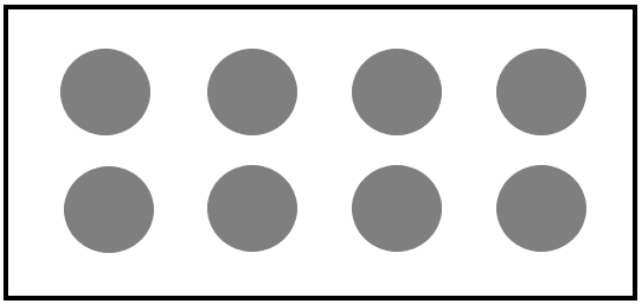

Figure 39 - Conductor and insulation homogeneously distributed

5.2.5 Core Modeling

As already mentioned, transformers core is made of several laminas kept together by the action of the clamping pressure. This leads to the question of if and how the core can be modeled in a simplified way, increasing ease of modeling, computational and modeling efficiency without losing accuracy. The answer to this question is not straightforward, especially due to the many different transformer cores configurations present. A sensitivity study in which the effect of different numbers of laminations on Equivalent Radiated Power (ERP) has been performed on the core of a traction reactor in which a butt-

lap joint is present between columns and yokes is present. Figure 40 shows the difference between a butt-lap and a step-lap joint.

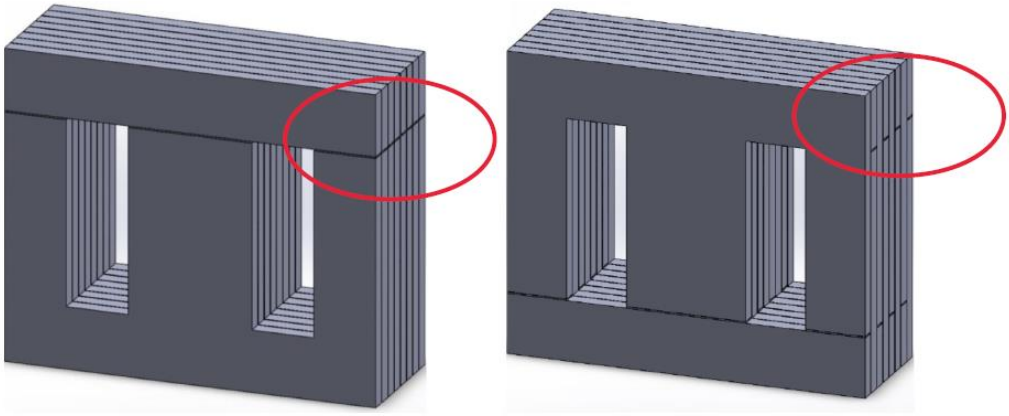

Figure 40 - Butt-lap joint (left) and step-lap joint (right)

The model is the same used to test the methodology and presented later. Butt-lap joint is the simplest joint existing, where no superpositions between leg ang yoke laminas are present. 5 models have been compared in which 32, 16, 8, 4 and no laminations have been modeled. Figure 41 shows the model with 32 laminations.

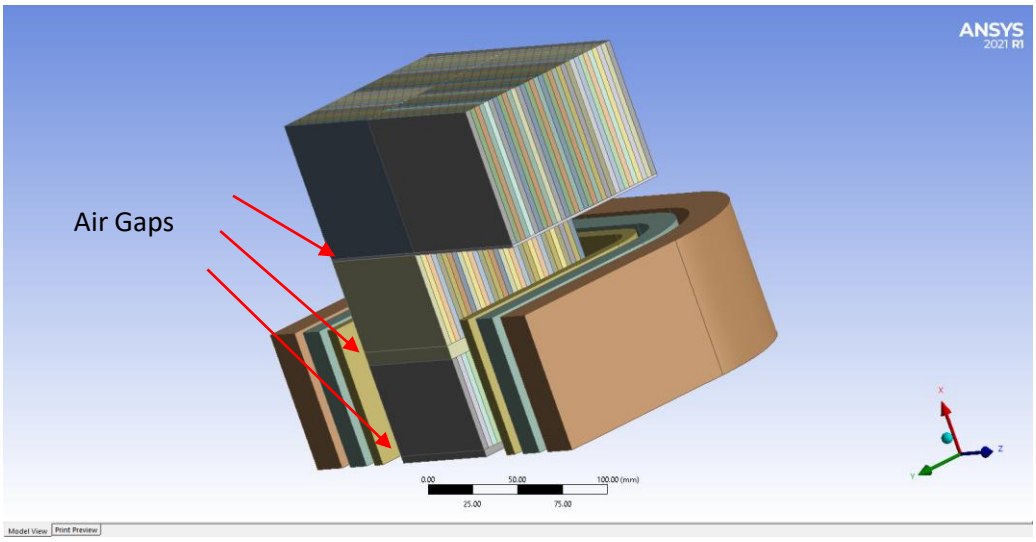

Figure 41 - Model for sensitivity analysis on the influence of number of laminations on Equivalent Radiated Power

All the parts composing the core have been bonded together apart from the central part of the yoke, where the interfaces between laminas and between laminas and air-gaps have been defined as a no separation contact, i.e. they have been left free to slide respectively, as shown on Figure 42. This is the reason why the yoke has been sliced in two different regions (corner and central part). This choice comes from a preliminary non-linear quasi static analysis in which the clamping of the core has been simulated and the contact status of all the parts composing the core has been computed. The model is presented in the Appendix 10.2.

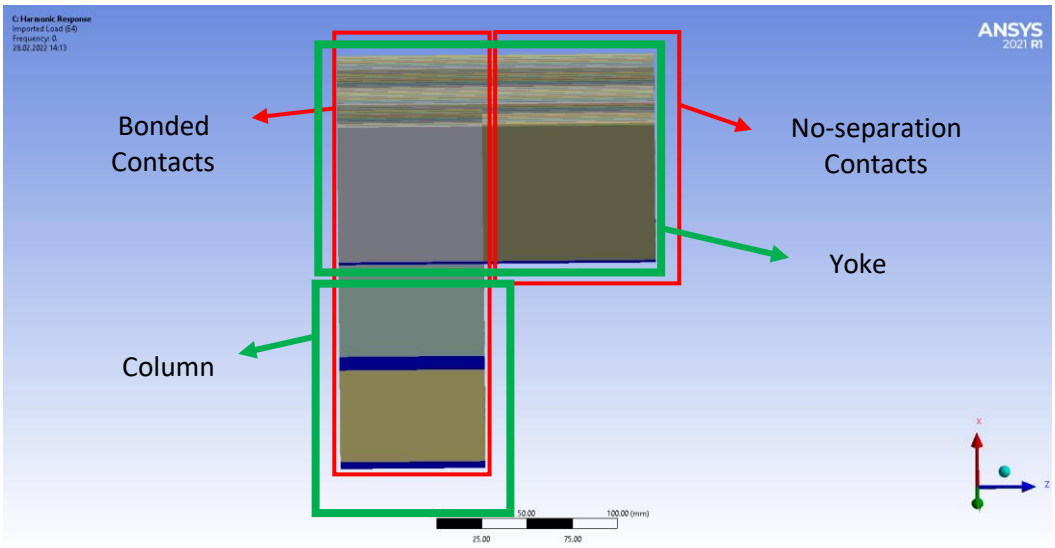

Figure 42 - Contacts definition

From the electromagnetic point of view, changing the number of laminations no difference is occurring in the computation of the magnetic field. Table 2 shows the results obtained from the structural analyses. The study has shown some interesting results: modeling the core as a monolithic solid (0 laminations) leads to the computation of almost the same ERP in x and y directions. ERP in the z direction shows a variability of 2 dB, which is acceptable considering the gain in terms of ease of modelling and computational efficiency. Also, it worth noticing that the total ERP shows a variability of only 1 dB. Finally, the model with a monolithic solid (0 laminations) with no separation contacts is compared with the one with bonded contacts in the central region of the yoke, which is the faster and more user-friendly modeling choice. The results are basically identical.
It must be admitted that this study has been affected by some hardware limitations which made impossible to choose a mesh fine enough to obtain a perfect force interpolation, especially for the models with higher numbers of laminations. For increasing laminations, a lower interpolation quality and a higher elements distortion was accepted. This could be the reason why a non-monotonic behavior of the solution was observed. For this reason, this study has to be intended as a first tentative of understanding the influence of modeling core laminations, which however gave some preliminary interesting and encouraging results suggesting that, regardless the uncertainty of the results, a monolithic core is the best modelling choice in the case of a butt-lap joint, due to the low variability observed in the computation of the total ERP.

The conclusion of this study is that modeling the core as a monolithic solid in which all the parts are bonded together is an acceptable choice at this stage, and it will be adopted in the first version of the automation.

In further developments, the same study will be performed using HPC. Moreover, it will be extended to different kinds of columns-yokes joints (single-step lap and multi-step lap joints) to understand if substantial differences are present in those cases.

Table 2 - Results of the number of laminations sensitivity analysis

N laminations	ERP [dB]	ERP [W]	Total ERP [dB] (uncoherent sum)	Force reaction magnitude [N] and orientation [°]
32	x 35.533 y 27.836 z 28.282	3.57e-9 6.07e-10 6.73 e-10	36.86	4.2808e+03 α = 1.6640 β = 89.0579 γ = 88.6285
16	x 34.945 y 27.429 z 28.645	3.12e-9 5.53e-10 7.3e-10	36.44	4.2843e+03 α = 1.2942 β = 89.6332 γ = 88.7589
8	x 34.758 y 27.571 z 27.837	2.99e-9 5.71e-10 6.07e-10	36.20	4.2930e+03 α = 1.4492 β = 89.2634 γ = 88.7520
4	x 34.513 y 27.491 z 26.776	2.82e-9 5.61e-10 4.76e-10	35.87	4.2551e+03 α = 1.2964 β = 89.2117 γ = 88.9709
0	x 35.206 y 27.739 z 26.689	3.31e-9 5.94e-10 4.66e-10	36.41	4.3166e+03 α = 1.3642 β = 89.6648 γ = 88.6776
0 (bonded)	x 35.184 y 27.739 z 26.739	3.29e-9 5.94e-10 4.72e-10	36.41	4.3154e+03 α = 1.3742 β = 89.6532 γ = 88.6683

6. Model development for methodology testing

The following chapters describe the model considered for applying and testing the methodology. The on-board XA3823B single-phase 700 KVA traction reactor produced by Hitachi Energy - Trasfor SA is analyzed. The same machine will be used for experimental validation of the methodology, on which experimental modal analyses in free-free conditions and noise tests in anechoic chamber will be performed. The reason for choosing this machine is the relatively lower complexity compared to other machines and dimension compatibility with the available anechoic chamber. Dimensions of the reactor are 500 x 400 x 400 mm.

The winding of the reactor has a rectangular shape and is composed of a solid aluminum conductor surrounded by epoxy resin. The core is made of laminated grain oriented electrical steel (M6T35) and is divided in sheets separated by air-gaps made of fiber glass, whose function is that of increasing the reluctance of the magnetic circuit and consequently reducing the magnetic field into the core. In the operative condition the reactor is enclosed in a steel box and connected to the train through it. The box is not considered in the simulation. The whole assembly is kept together by a frame made of AISI 304 and A4 70 structural steels. The CAD geometry of the transformer has been created using Creo 4.0 software by mechanical designers and imported in ANSYS Design Modeler. Winding is modeled as homogenized while core is modeled as a monolithic solid, based on the considerations mentioned before. Figure 43 shows the selected model.

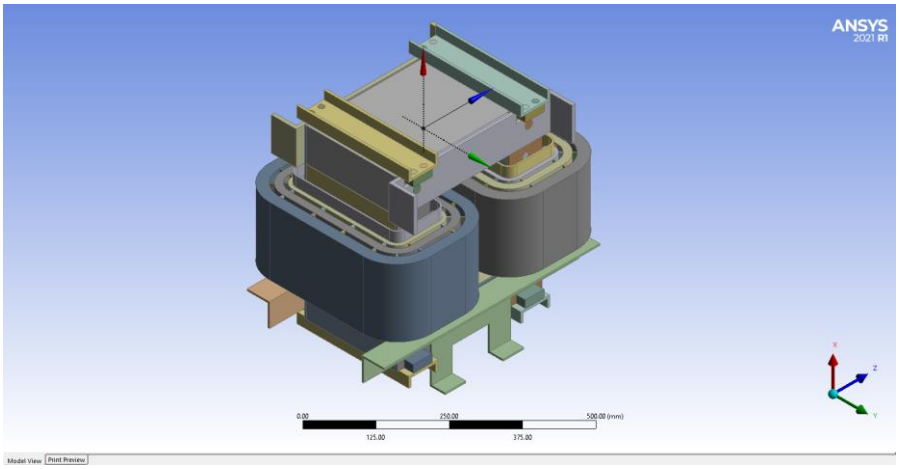

Figure 43 - XA3823B traction transformer

6.1 Electromagnetic model

6.1.1 Geometry

After having created the geometry, the latter is connected to two different Maxwell simulations into the Workbench project page, as shown on Figure 44. One of them is an Eddy Current simulation (electromagnetic harmonic simulation) and it is used for computing Lorentz forces on the winding as well to perform an automatic mesh refinement. The auto-refined mesh is then used as the mesh of the second Maxwell simulation, i.e. a transient analysis from which core forces are computed.

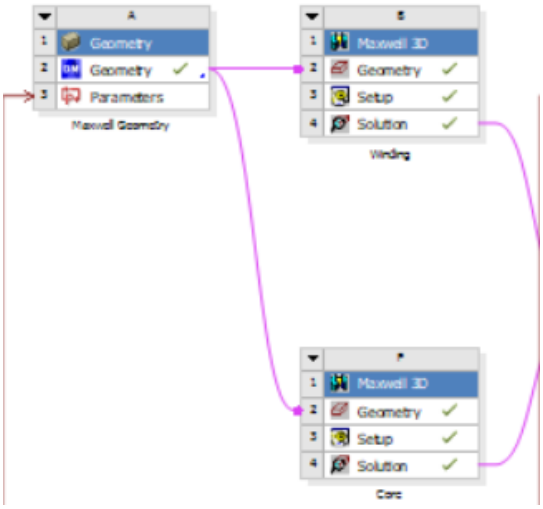

Figure 44 – Maxwell simulation set up in Workbench project page

Before starting the modeling, a defeaturing activity is needed to delete all the transformer components which are not relevant to the electromagnetic analysis. Only the winding and the core are required. The same geometry for both the Eddy Current and transient simulations is used. A homogenized winding and a monolithic core are modeled. Core holes are defeatured. Figure 45 shows the geometry used for the electromagnetic simulations, in which $1/8^{th}$ symmetry (which is valid here from the EM point of view) has been exploited. This optimizes the computational efficiency and allows to use a finer mesh leading to increasing accuracy.

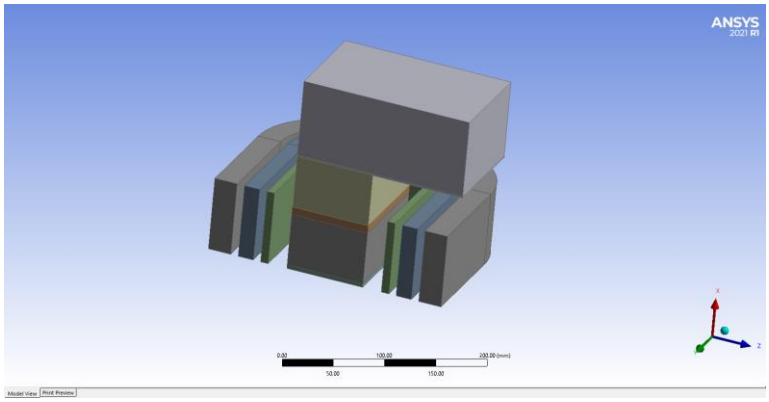

Figure 45 – EM model geometry

When performing electromagnetic simulations, the enclosure domain representing the surrounding fluid (air in this case) is also modeled. this is modeled as a rectangular box in a 3D simulation and as a rectangle in a 2D simulation. The transformer must be at the center of the enclosure. As a rule of

thumb, if core is present the length of the enclosure edges should be at least two times the characteristic length of the transformer in the same direction. For example, if the vertical dimension of the transformer is L, the vertical edges of the enclosure should be $2L$. The same applies to the other dimensions. These considerations have been deducted by sensitivity studies on the influence of the enclosure domain size. Figure 46 shows the modeled enclosure box.

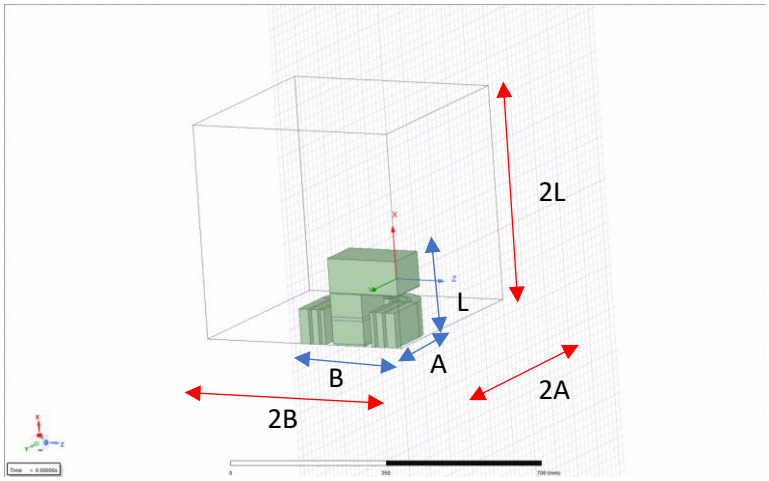

Figure 46 – 3D Enclosure dimensions for transformers with core

If core is not present like for the air-core reactors, which is not the case for this model, the contour vertical sides should be at least three times the winding height while the two other (radial) dimensions should be at least three times the winding radius length in the same direction. Figure 47 shows the domain dimension for an examined model of a 2D axisymmetric winding without core. The reason why a smaller enclosure is used when the core is present is that in that case the magnetic field is basically contained in the core only.

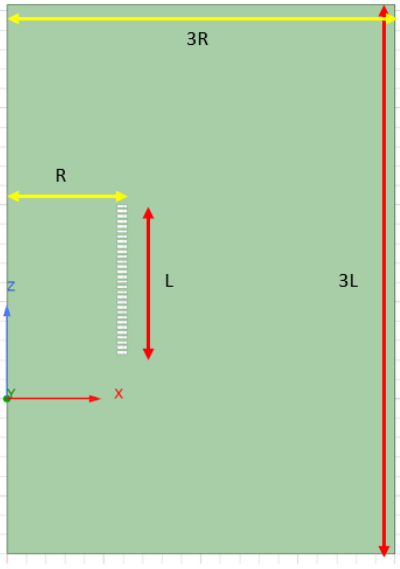

Figure 47 - Enclosure dimension for transformer without core. L is the height of the winding, R is its radius.

6.1.2 Analysis type

The following hypotheses are assumed for the electromagnetic simulation used for Lorentz forces computation:

- Linearity (linear dependance between magnetic potential/flux and current, constant magnetic permeability of conductor and core materials). Saturation is not considered
- Isotropic material (magnetic permeability equal in all the directions)
- Harmonic excitation
- Only steady state is considered.

For this reason, a harmonic analysis is performed for Lorentz forces computation, i.e. an *Eddy Current* analysis in Maxwell. The hypothesis of constant magnetic permeability deserves some observations. Magnetic permeability μ links magnetic field strength *H* to the magnetic flux density *B* according to Equation 18.

$$\boldsymbol{B} = \mu_0 \boldsymbol{H} \qquad (18)$$

In general, the link between *B* and *H* is described by the non-linear B-H curve, already shown on Figure 33. Looking at this curve, it is evident that the hypothesis of constant magnetic permeability, which actually is the slope of the curve, is valid only for a relatively low induction, i.e. when saturation is not reached, where the B-H curve can be reasonably considered linear. For the specific case of the model considered here, a preliminary magnetostatic analysis has been performed from which a magnetic field of approximately 1.0 T has been computed, as shown on Figure 56. Since for this level of induction the B-H curve can be considered linear, a constant permeability has been used for further analyses.

B-H curve is also characterized by hysteresis. However, taking in consideration hysteresis would lead to an increasing complexity of the simulation, with high order odd harmonics introduced in the magnetic flux *B,* which makes results difficult to be interpreted. For this reason, hysteresis has been neglected.

$$\boldsymbol{B} = \mu_0 \boldsymbol{H}$$

The following hypotheses are assumed for the electromagnetic simulation used to compute core forces:

- Constant magnetic permeability of the core steel
- Linearity and absence of hysteresis in magnetostriction
- Isotropic material (magnetostriction and magnetic permeability equal in all the directions)
- Harmonic excitation (input current as a sum of sinusoids)

For this reason, a transient analysis is performed to compute core forces. The hypothesis of isotropic material is not actually realistic, since the electrical steel used in the here analyzed traction transformer is a grain-oriented steel. Properties in the rolling directions are different from the ones in the transverse directions. Magnetic permeability in the transverse direction should be approximately considered 10 times lower than the permeability in rolling direction. Same considerations are valid for magnetostriction, which in general varies in the different directions. However, for the same reason of making the simulation as simple as possible to easily judge the results, the assumption of material isotropy is used. Further development will take into consideration anisotropies, which however are straightforward to be implemented.

Regarding simulation time and time steps for defining solver parameters, one entire cycle of the current is simulated. Time step is chosen in order to have sufficiently smooth signals in time domain

and to avoid aliasing. The minimum time step is calculated according to Shannon theorem, i.e. Equation 19, where f_{max} denotes the maximum force frequency expected.

$$time\ step \leq \frac{1}{2f_{\max}} \qquad (19)$$

As a rule of thumb, if saturation is not considered (linear B-H curve, i.e. constant permeability or non-linear B-H curve with low magnetic field), the loads are expected to have only one harmonic at double the frequency of the current, i.e. $f_{max} = 2 * f_{current}$. If saturation is considered, a sensitivity analysis is needed to understand how different time steps influence the different harmonics. In fact, predicting the harmonic content of the forces in this case is not straightforward.

6.1.3 Materials

Materials properties assigned to the different parts should be taken from supplier datasheets. In the model here considered, the winding conductor is made of aluminum while the core is made of M6T35 grain oriented electrical steel. Same materials have been assigned in the two different electromagnetic simulations. The predefined aluminum material available in Ansys is assigned to the conductor, since it is representative of different types of aluminums, while for the core, material properties have been manually set. A constant and isotropic relative permeability equal to *1500* is used for the core material, which is a reasonable value for an electrical steel used in transformers cores. The material assigned to the enclosing air is the predefined *air* in Maxwell. Finally, since the air-gaps inserted in the core are made of fiber glass and since this material has insulating electromagnetic properties similar to the air, *air* is assigned to them. Table 3 resumes the material properties used for the different materials.

Table 3 - Material properties used in the model

Material	Relative permeability	Bulk Conductivity [S/m]
Aluminum	1.000021	38000000
Core Steel	1500	2000000
Air	1.0000004	0

For the model used to compute core forces, magnetostriction must be defined. Since the magnetostriction curve for the M6T35 electrical steel was not available, the selected curve is here considered as a quadratic relation between magnetostrictive deformation and magnetic field strength *H.* This means that the magnetostriction curve used is a parabola whose coefficients have been selected to achieve reasonable values of magnetostriction. Figure 48 shows the selected magnetostriction curve for the electromagnetic simulation. The curve has been defined for the range of *H* equal to *0-1500 A/m,* after having checked that the maximum *H* reached in the core is about *1000 A/m* while the average value is approximately *500 A/m*. For *500 A/m* magnetic strength, magnetostriction is equal to *0.5 ppm.* Unless these are reasonable values for magnetostriction of electrical steel, magnetostrictive forces computation has to be considered affected by uncertainty and the real curve should be experimentally measured for an accurate estimation of those forces. The curve has been created in Matlab and then imported in Maxwell, in order to obtain a smooth curve. Having a smooth curve is important for the following reason: since a harmonic analysis is used for the structural simulation, an FFT of the core forces obtained from the transient EM analysis is computed. The obtained spectrum is then used as the excitation in the structural model. Having a smooth magnetostriction curve avoids aliasing on the FFT computation of the magnetostrictive forces due to curve discretization. Another important material property regarding the computation of magnetostrictive forces is the Young's modulus assigned the core steel, since it is involved in the

computation of the same forces starting from magnetostrictive deformation, as shown in Equation 6. In this case, a Young's modulus of *200 GPa* is chosen.

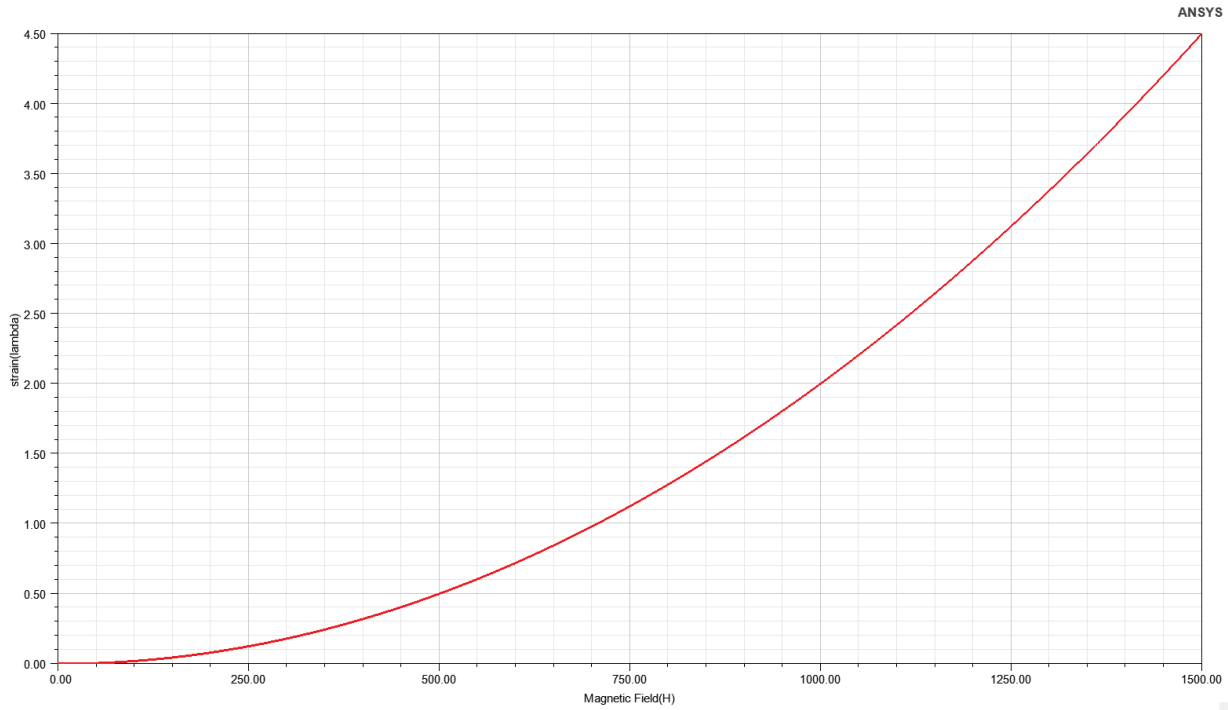

Figure 48 – Selected magnetostriction curve for the EM simulation

6.1.4 Mesh

Ansys Maxwell makes use of tetrahedral elements only and performs an automatic refinement when an Eddy Current simulation is performed. However, some mesh parameters are set in order to obtain a more regular mesh and to help convergence. The auto-refined mesh output from the Eddy Current simulations is then used as the mesh of the transient analysis, in which mesh auto-refinement is not supported. For this reason, the Eddy Current simulation is run first and the transient analysis later. This explains why two different electromagnetic analyses are used.

The initial mesh settings for the Eddy Current simulation are chosen to obtain a relatively refined mesh on both the winding and the core. In fact, unless an auto-refinement is performed, if the initial mesh is too coarse convergence takes longer. Figure 49 shows the initial mesh and the auto-refined one. Since in this case core air-gaps are present, and since they generate high gradients of the magnetic field distribution in the regions close to them, the initial mesh assigned to the core is finer than the one assigned to the winding. It is shown that after the auto-refinement, the mesh is refined in correspondence of the air-gaps. As already said, the auto-refined mesh is used as the mesh of the transient analysis for core forces computation.

Figure 49 - Initial electromagnetic mesh (left) and auto-refined mesh (right)

6.1.5 Excitations and boundary conditions

For both the electromagnetic models, a current intensity or a current density excitation can be assigned to the winding. Peak values have to be assigned in Ansys Maxwell. The values of the excitation are set equal to the ones reported in the specifications, which provide the current passing through each turn. Since a homogenized winding is used, the current excitation must be set equal to the current passing through a single cable multiplied by the number of turns contained in the modeled portion of the winding. This is the correct procedure to compute the resultant Lorentz forces and the magnetic field. Table 4 shows the current values provided by specifications and the current excitation assigned in the model to each winding section. *10.7, 21.4* and *32.1* turns are contained in the first, second and third sections of the winding respectively. A non-integer number of turns is present because the first (or the latter) turns, i.e. the more external ones, are not completed during manufacturing (they are not rounded for 360°, but for a smaller angle). Since half of the height of the winding is modeled due to symmetries, half of the turns are considered. This means that the current assigned to the first section is equal to $190\ A_{rms}\ x\ \sqrt{2}\ x\ 5.35\ turns = 2875\ A$. Same logic is used for assigning the current to the remaining winding sections. For simplicity, only the harmonic at 50 Hz is considered in this model. Further developments will consider all the harmonics. Figure 49 shows the current excitation assignment, the current in time domain and the contour of the current density.

Table 4 - Current excitation

Frequency [Hz]	Current Specifications	Current Model (section 1 – 2 – 3) [A]
50	190 Arms	1437.5 – 2875 – 4312.5
1500	20 A	107 – 214 - 321
1900	20 A	107 – 214 - 321

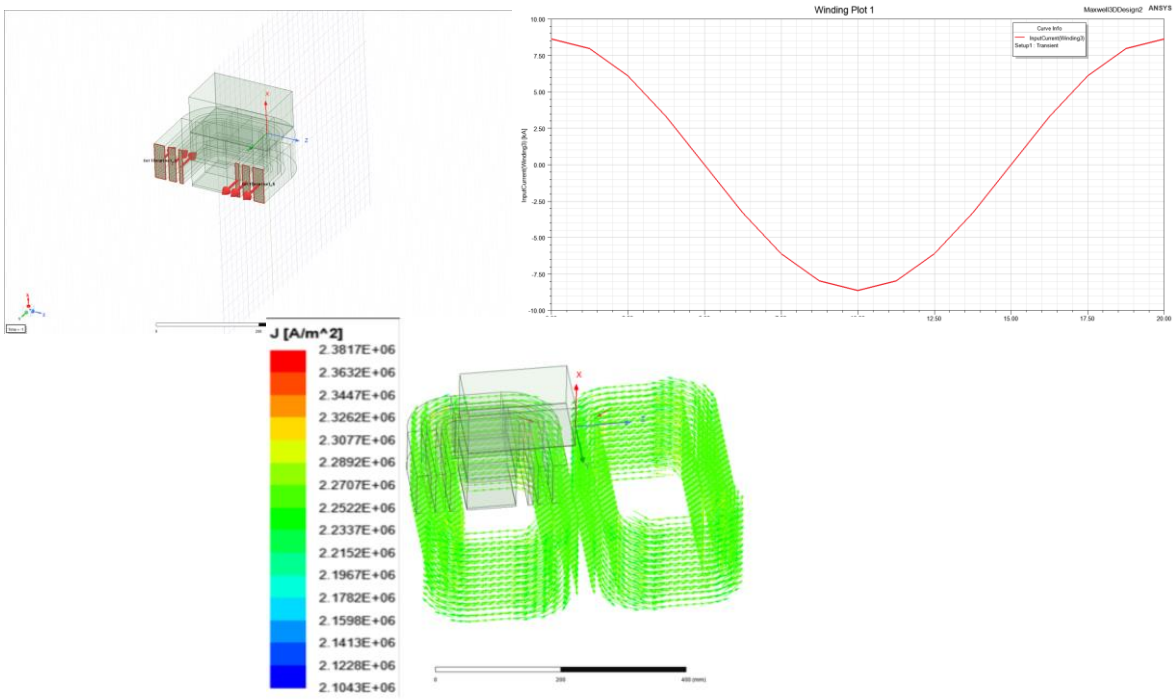

Figure 50 - Current excitation at each section (top) and computed current density (bottom)

Some considerations on Skin Effect are here needed since this is affected by different choices in assigning the excitation in Ansys. Skin Effect is a non-uniform distribution of current density across the conductor's section, in which current concentrates at the edges of the conductor section for increasing frequencies. Assigning a current density as excitation, Skin Effect cannot be taken into account, since a uniform current density distribution is defined. Skin Effect can be captured only using a current or a voltage excitation. When using a current excitation, as in this case, two options for defining the type of conductor are available in Maxwell: *solid* or *stranded.* Figure 51 shows the difference between a solid and a stranded conductor.

- Using the *solid* option, the modeled conductor is considered as a solid and Skin Effect is visible

- Using *stranded* option, the modeled conductor is considered as made of multiple cables. Since this is equivalent to imposing a more uniform current density across the section, Skin Effect is not visible.

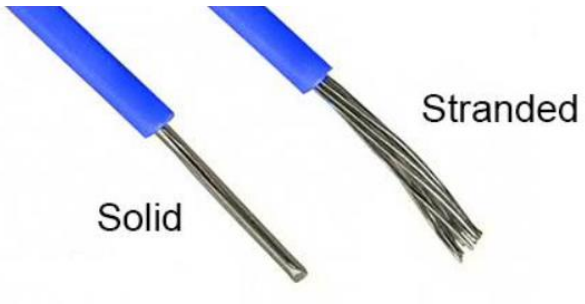

Figure 51 - Solid vs stranded conductor.

If Skin Effect is of interest, all the turns must be modeled, and the current must be assigned on each turn cross section. A zero-thickness insulation boundary condition on the turns' skin must be also

assigned, in order to avoid the current density to flow across different turns, as wrongly happens on Figure 52.

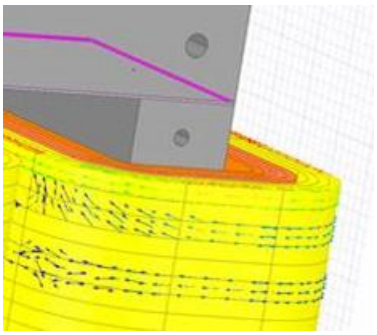

Figure 52 - Current density wrongly flowing across different turns

However, Skin Effect can be neglected when dealing with acoustics. Skin Effect generates a redistribution of the current density on each turn section, but this doesn't affect its direction nor its integral, i.e. the intensity of the total current remains the same. Skin Effect only affects the distribution of the volumetric Lorentz forces $[\frac{N}{m^3}]$. The direction and the intensity of the resultant Lorentz forces [N], which are the interesting one when dealing with acoustics (only the global behavior is of interest), are not modified by Skin Effect. This is the reason why the winding can be completely homogenized as it was the case for this model. Since Skin Effect is not of interest, the *Stranded* option is used in order to avoid it. shows the excitation assignment for each section and the resulting current density inside the winding. A way to check if the current has been assigned correctly, is to calculate the expected current density by simply dividing the current intensity assigned to each section by the cross-sectional area of the considered section. The result of this operation must be equal to the computed current density.

Another important choice which deserves some considerations is whether or not Eddy Effects, i.e. induced currents, have to be considered inside the core. When a magnetic field travels through the core, parasitic currents are induced. These induced currents rotate around an axis parallel to the direction of the magnetic field but with an orientation such that they produce a magnetic field which opposes to the external one. This phenomenon is described by the well-known Lenz law. The reason why the core of a transformer is made of laminated steel sheet is that this reduces the induced currents, leading to decreasing core losses due to Joule effect. Since in the model here described a monolithic core is considered, Eddy effects must not be computed, since the induced current intensity would be unrealistically high. For this reason, Eddy Effects are not selected. Figure 53 shows an example of induced current inside the core of a model in which the core has been divided in 4 slices. Upper and lower parts represent the cross-sectional areas of the yokes, while the inner part represent the columns.

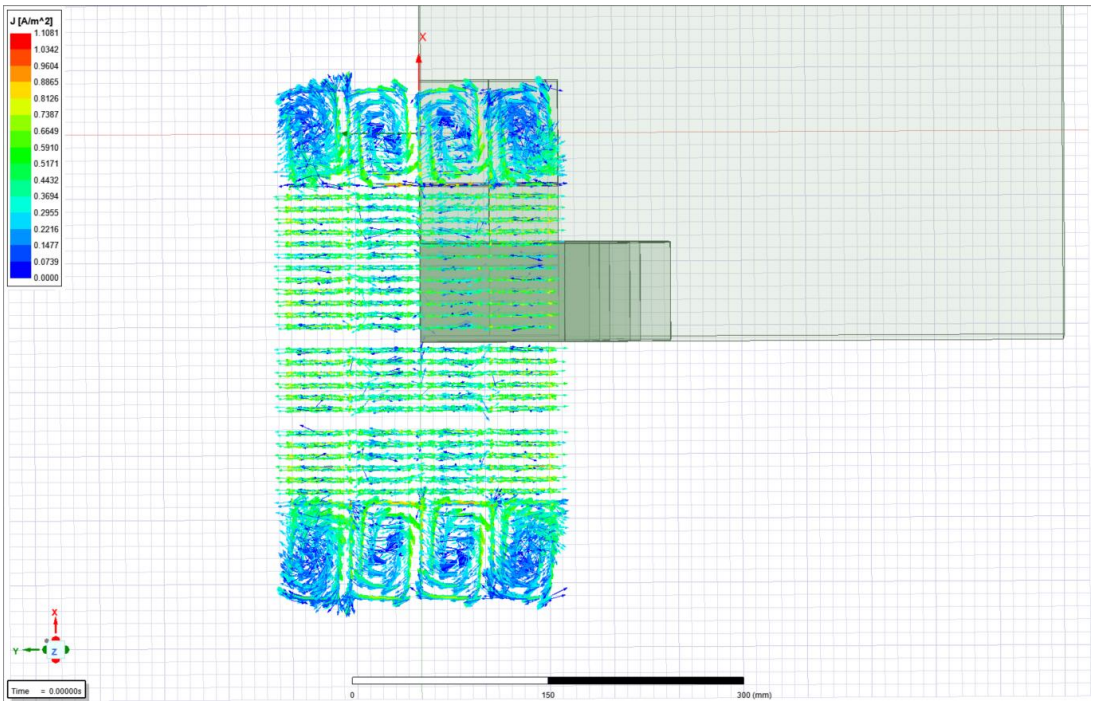

Figure 53 - Induced current inside the core

Two main boundary conditions are applied to the model:
- The non-reflecting boundary condition assigned to the domain boundaries, as shown on Figure 54. The *Zero Tangential H Field* boundary condition can be used in Ansys, which represents full absorption, i.e. an infinite permeable boundary. However, when core is present, as in this case, since the magnetic field is basically completely contained into the core, the boundary condition set on the enclosure boundary has no influence on the results

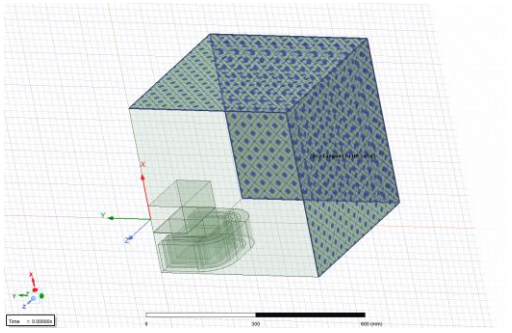

Figure 54 - Zero tangential H-field boundary condition

- The symmetries. Two types of symmetries are used: a *flux normal* is assigned to faces lying on symmetry planes where the magnetic flux must be normal, while a *flux tangent* is assigned to faces lying on symmetry planes where the magnetic flux must be tangential. In the presented model, the normal flux symmetry is assigned to the faces lying on XY and YZ planes, while the tangential flux symmetry is assigned to the faces lying on XZ plane. Symmetry boundary conditions must not be defined where an excitation has been defined. Figure 55 shows how the boundary conditions have been applied.

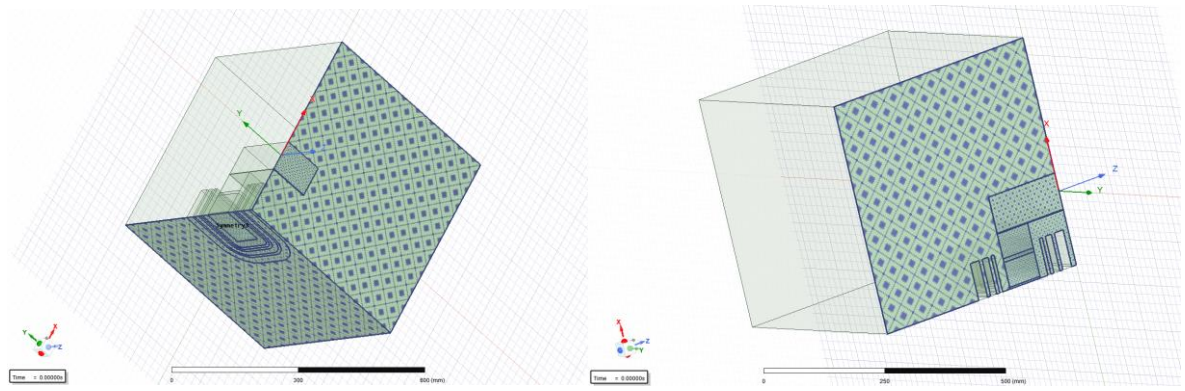

Figure 55 - flux normal boundary condition (left) and flux tangential boundary condition (right)

6.1.6 Post processing

During the post-processing it is important to check that the model is behaving as expected. A first check is that of computing the magnetic flux density *B* inside the core using an analytical model. This can be done using Equation 20 and Equation 21, which reasonably assumes that the reluctance of the air gaps is much higher than the core's one and the magnetic permeability of the same air-gaps equal to the one of the air. ϕ denotes the magnetic flux [*Wb*], n the number of turns, i the current intensity, l_i the thickness of the i-th air-gap (in this case the two air gaps between the column and the yokes have a thickness of $1.5\ mm$ while the ones inserted in the columns have a thickness of $8\ mm$), A_i the area of the air gaps normal to the magnetic flux and A the cross sectional area of the core, which in this case is equal to A_i and corresponds to $8600\ mm^2$. The calculated magnetic flux density B in this case is equal to *0.8 T,* while the computed magnetic flux density inside the central region of the columns is approximately equal to *0.9 T,* as shown in the right picture of Figure 56. The magnetic flux density into the yokes is underestimated by the analytical model due to the redistribution occurring in these regions.

$$\phi = \frac{n*i}{\sum_i R} = \frac{n*\ i}{\sum_i \frac{l_i}{\mu_0 A_i}} \qquad (20)$$

$$B = \frac{\phi}{A} \qquad (21)$$

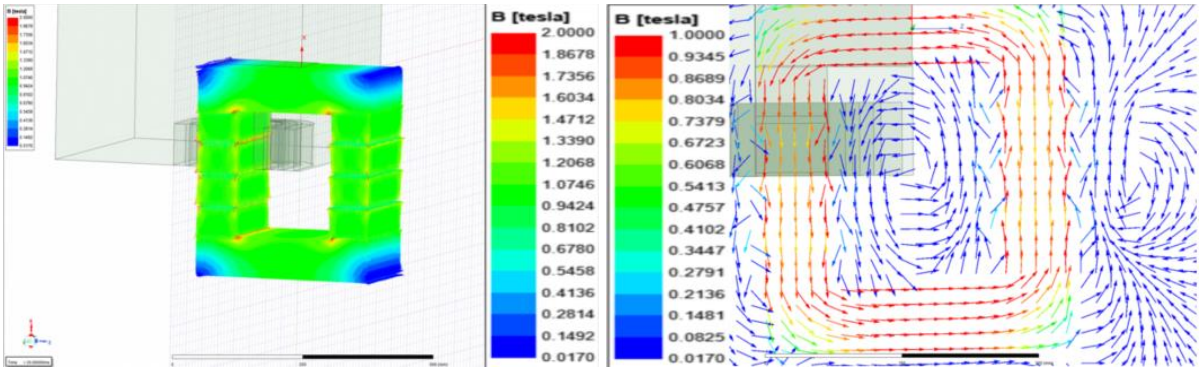

Figure 56 - Magnetic flux density B 3D distribution (left) and magnetic flux density distribution on XZ plane (right).

A second check is that of computing the FFT of electromagnetic quantities for which the harmonic content is expected. Since an excitation at 50 Hz is here used, performing an FFT of the current a band in correspondence of 50 Hz only is expected. Figure 57 shows the current excitation in time domain and the respective FFT computed with rectangular windowing. Only the 50 Hz harmonic is present.

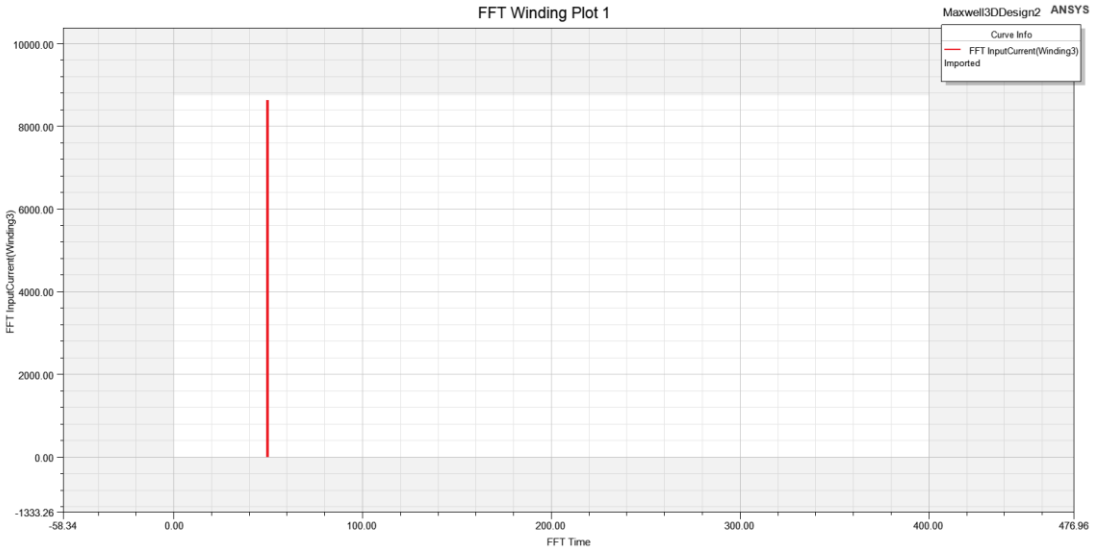

Figure 57 - Current excitation FFT

Another check is that of performing the FFT of the magnitude of the forces into the core and the winding in the transient analysis (Lorentz forces are computed also in the transient analysis). Since saturation and hysteresis are not considered, magnetic flux density has the same harmonic content of the current (50 Hz). Since a perfectly quadratic magnetostriction is here implemented and Maxwell forces depend on the square of the magnetic flux density by definition, the core forces are expected to have a DC component (0 Hz) and a harmonic at double the frequency (100 Hz) of the exciting current. Figure 58 confirms this statement. For the same considerations made before on the magnetic flux density, Lorentz forces are expected to have the same harmonic content of core forces. Figure 59 confirms this statement.

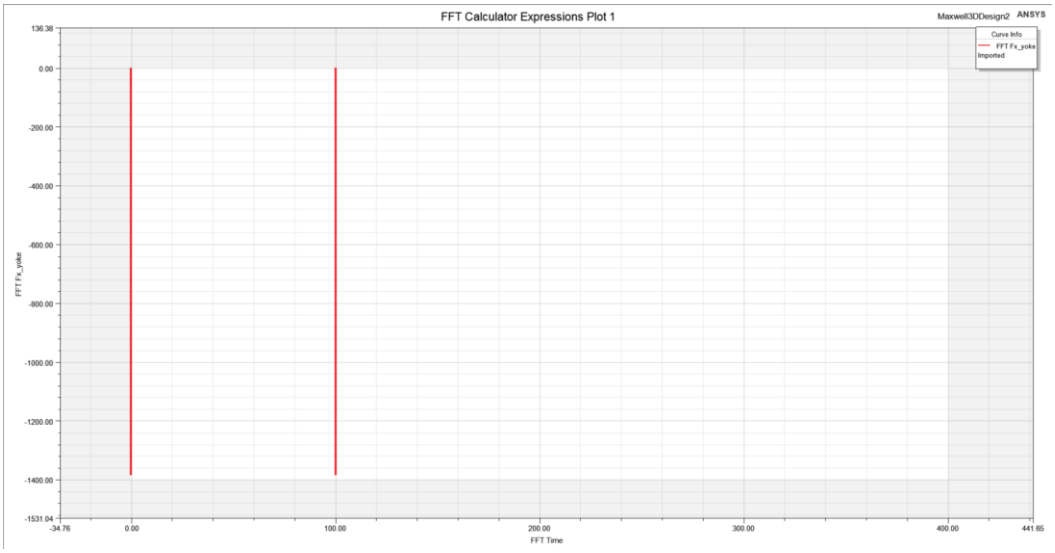

Figure 58 – Vertical component of the force on the yoke FFT

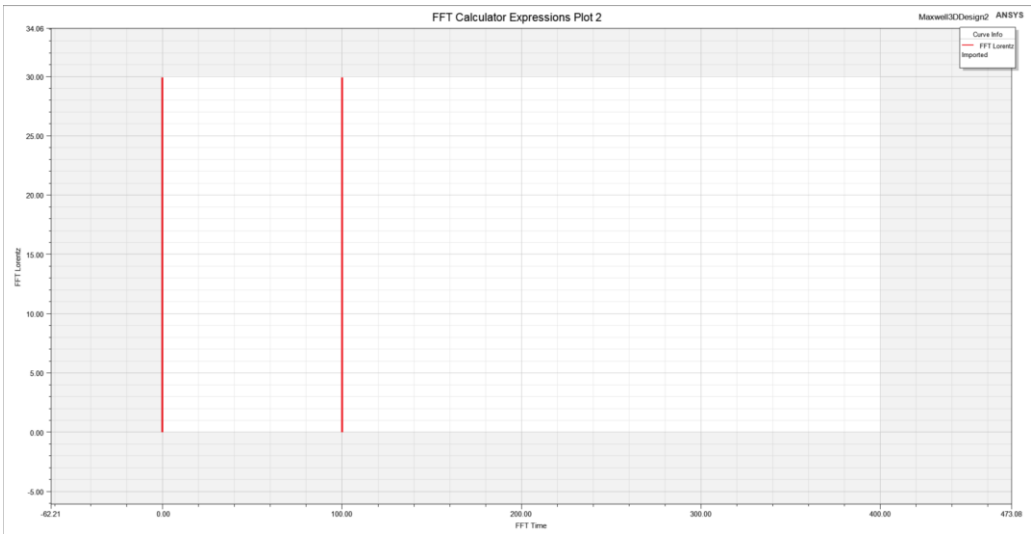

Figure 59 - Lorentz forces magnitude on the outer section FFT

For completeness, the effect of saturation on the harmonic content of the magnetic flux density B is presented. The B-H curve shown on Figure 33 is used and an excitation double the real one is used to artificially induce saturation. A magnetic field greater than *1.8 T* is reached in the model, which means that saturation is achieved. The effect of saturation is that of introducing higher odd harmonics as shown on Figure 60. In this specific case, the 3rd, 5th and 7th harmonics have 4.6%, 1.2% and 0.3% amplitude of the fundamental harmonic.

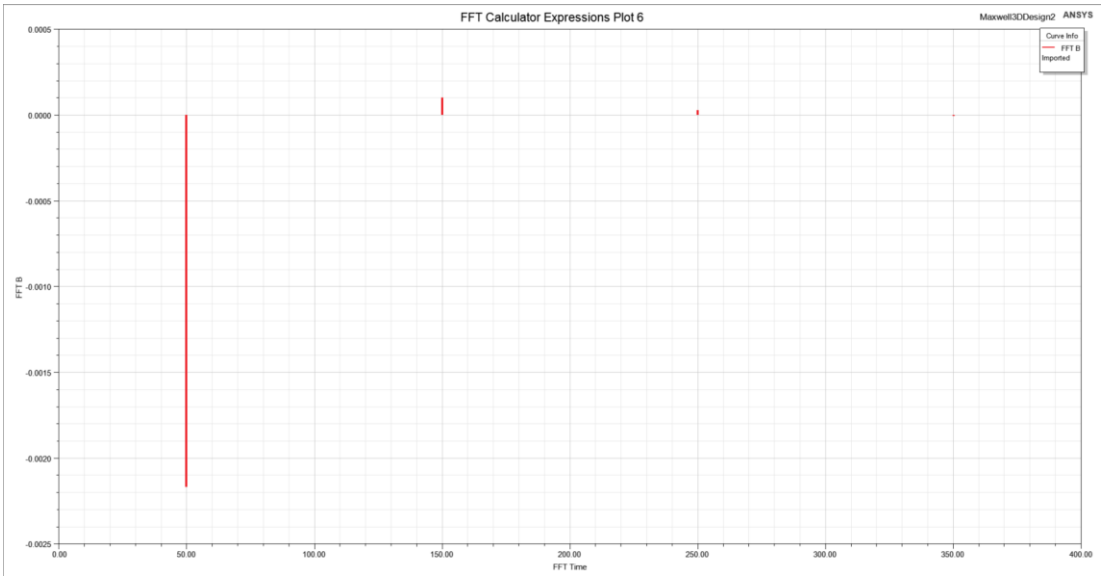

Figure 60 - Magnetic flux density B FFT (right)

The last point which is interesting to investigate is which electromagnetic force is the dominating one. It worth mentioning that Ansys Maxwell doesn't allow to compute magnetostrictive forces alone. Only two options are available: computing Maxwell and magnetostrictive forces together or computing Maxwell forces only. However, a technique for separating the contributions of the different forces to the Sound Power is available. It is presented in Appendix 10.4. From the model here analyzed it has been obtained that Maxwell forces and magnetostrictive ones are comparable, as shown in Table 5, where the magnitude of the forces on the relevant bodies are reported. The magnitude of magnetostrictive forces can be calculated by subtracting the 2nd column to the 3rd one. However, it must be noted that uncertainties on the definition of magnetostriction curve are present. Also, this conclusion is valid only for the here considered model, in which air gaps are present. Intuitively, it could

be stated that if air-gaps are not present Maxwell forces inside the core will be much lower. Further development analyzing different configuration of cores will give a clearer understanding. Finally, it is evident that Lorentz forces are negligible compared to the core ones. This is due to the presence of the core, where most of the magnetic field is contained. On the winding, i.e. outside the core, the magnetic field is low, leading to low Lorentz forces. For coreless transformers, winding forces are expected to be much higher.

Table 5 - Comparison between Maxwell, magnetostrictive and Lorentz forces resultant magnitude

	Maxwell only [N]	Maxwell + magnetostriction [N]	Lorentz [N]
F_yoke [N]	2795	6836	
F_column_upper [N]	5150	7403	
F_column_lower [N]	4816	7240	
Section 1 (inner)			50
Section 2 (middle)			81
Section 3 (outer)			59

Figure 61 shows the distribution of Lorentz and core forces (Maxwell + magnetostriction). Lorentz forces present intensifications in regions near the air-gaps, where the magnetic field is actually concentrating. Maxwell and magnetostriction forces are concentrated on the air-gaps due to material discontinuity, which leads to high gradient of the magnetic field and consequently to high gradients of Maxwell and magnetostriction stresses. Since in the context of the weak formulation of the momentum equation volumetric forces are directly dependent on the variation of stresses, namely on the divergence of the stress tensor (in this case stresses due to Maxwell stresses and magnetostrictive strains), volumetric forces are higher where stress variations are higher.

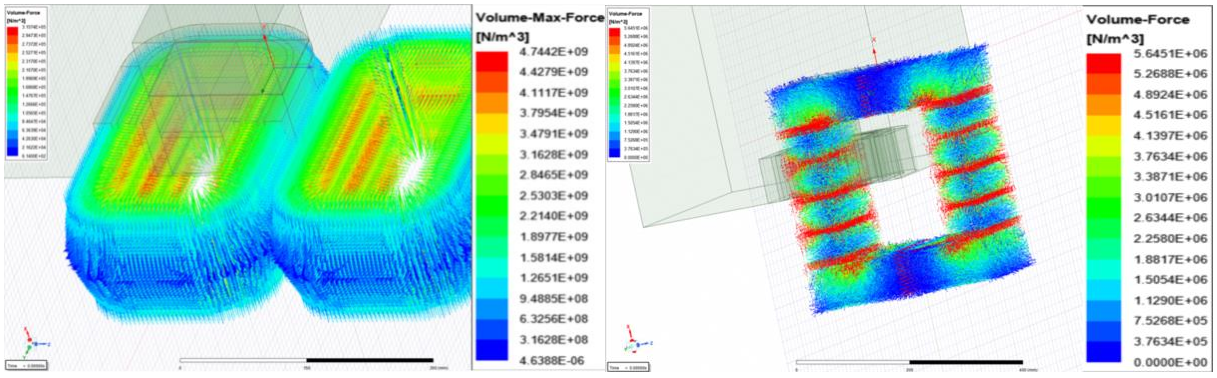

Figure 61 - Lorentz forces (left) and core forces, Maxwell + magnetostrictive (right)

6.2 Structural model

The updated Workbench project page once the structural model is introduced is shown on Figure 62. Electromagnetic forces computed in Ansys Maxwell are imported into a structural harmonic analysis through the connection between Maxwell Solution and Harmonic Response Setup. In this chapter, the structural model used to compute the vibration velocities of the structure is be presented.

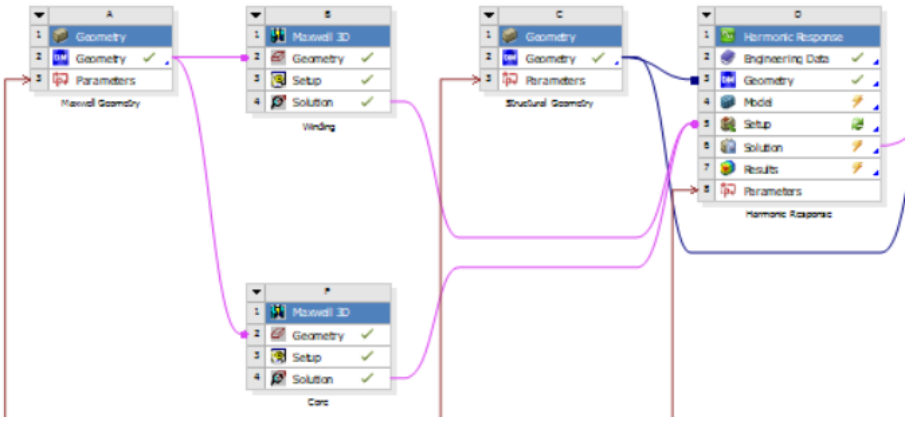

Figure 62 - Workbench project page for structural analysis

6.2.1 Geometry

The same geometry used for electromagnetic analyses must be used for performing the structural analysis for consistency. In fact, force interpolation in Ansys is topology-based. To simplify the structural meshing and to increase the computational efficiency, a defeaturing operation is also needed for the structural model. Features which are not important for the analyses, like bolts, washers, tie rods, fillets, holes are removed. Also, it is important to avoid geometries which would lead to singularities into the acoustic domain, since the geometry used for the structural model is used to create the acoustic domain geometry. An example is that of the sticks used for cooling channels between the winding sections. In many cases, these sticks have a dog-bone shaped cross section, which creates a cuspid in correspondence of the contact region between spacers and winding, as shown on Figure 63. This geometry corresponds to a geometrical singularity in the acoustic domain, which would lead to meshing and convergence issues. For this reason, the stick cross section must be modified from a dog-bone like shape to a rectangular one. The correspondent stiffness modification must be considered and if it is non-negligibly modified, it should be recovered assigning an equivalent material property which leads to same dynamic behavior of the real stick, with a procedure similar to the one used for winding homogenization. The flectional stiffness in the radial direction of the winding should be accurately reproduced.

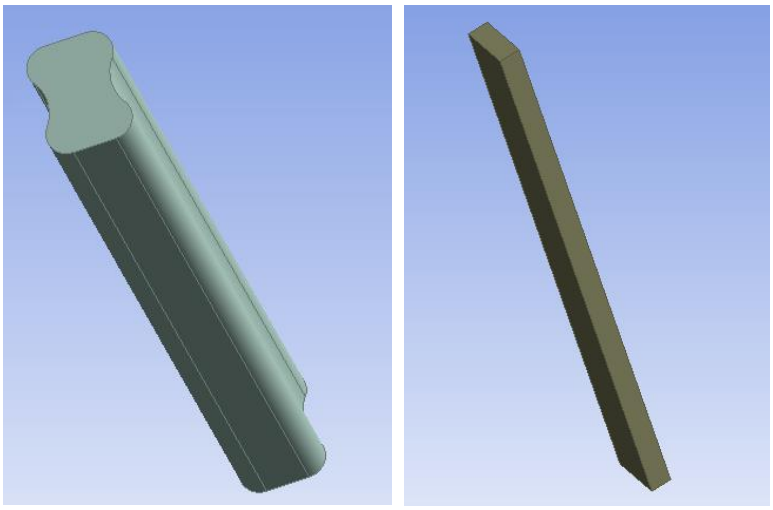

Figure 63 - Sticks geometry simplification

Figure 64 shows the geometry used for the structural model, in which 1/4th symmetry (valid here from the mechanical point of view) has been exploited. The reader would have now noticed that in the electromagnetic model 1/8th symmetry has been exploited while in mechanical one 1/4th is exploited. Although this seems to be non-compatible for a topology-based interpolation, this can be done in Ansys. Ansys automatically performs the interpolation on the parts of mechanical geometry which has not been used in the electromagnetic model, based on the symmetry boundary conditions specified in the electromagnetic model. This is a useful feature which allows simulation time to exponentially decrease, allowing to exploit all the symmetries, even if they are different between the electromagnetic and the structural model.

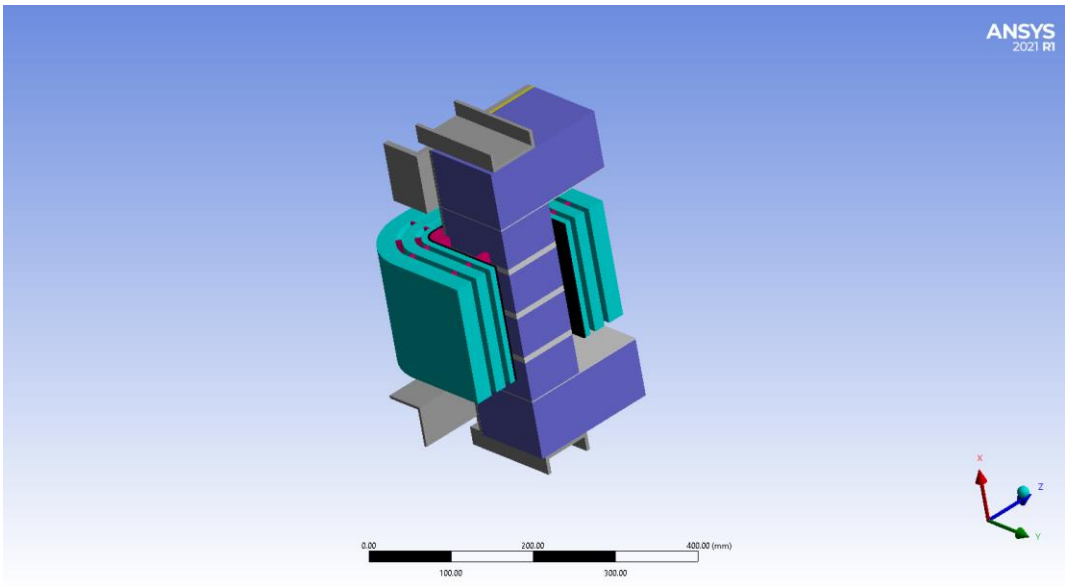

Figure 64 – Geometry used for structural analysis

6.2.2 Analysis type

The following assumptions are made:

- Linear behavior (linear dependance between displacements and forces, linear material mechanical behavior)
- Harmonic excitation (periodic Lorentz and Maxwell forces, magnetostriction decomposed in periodic contributions at different frequencies)
- Only steady state is considered.
- Initial deformation due to DC component of forces is neglected due to software limitations
- Temperature is supposed to be 22 °C for all the parts

For this reason, a harmonic analysis is performed. The hypothesis of harmonic excitation deserves some observations. As already mentioned, core forces are computed through a transient electromagnetic analysis, this in order to take into account magnetostriction non-linearities. However, only a harmonic analysis is performed for the structural model. An FFT of the core forces is automatically performed by Ansys and the computed spectrum is given in input as the excitation of the structural model. Using this approach introduces some errors due to the FFT computation of discretized time signal but largely improves the computational efficiency of the workflow and makes the results easier to be judged using the frequency domain. The equation of motion is solved in the Laplace domain according to Equation 22 making use of FEM approximation.

$$s^2\mathrm{M}\boldsymbol{u} + s\mathrm{C}\boldsymbol{u} + \mathrm{K}\boldsymbol{u} = \boldsymbol{F_{Lorentz}} + \boldsymbol{F_{ms}} + \boldsymbol{F_{Maxwell}} \qquad (22)$$

All the electromagnetic forces, each of them with its harmonic content, are applied to the relative structural component. Vibration velocities on the whole structure are computed. These are then used as the excitation in the acoustic model.

$s^2\mathrm{M}\boldsymbol{u} + s\mathrm{C}\boldsymbol{u} + \mathrm{K}\boldsymbol{u} = \boldsymbol{F_{Lorentz}} + \boldsymbol{F_{ms}} + \boldsymbol{F_{Maxwell}}$

The damping coefficient is calculated according to the Rayleigh model, for which a damping proportional to the mass and the stiffness of the structure is assumed. The proportionality coefficients, which are required in Ansys, are calculated according to Equation 24, where the damping ratios ξ_i and ξ_j are assumed equal to *0.02,* the lower limit ω_i of the frequency range considered is assumed equal to $2\pi\,\frac{rad}{s}$ (frequency equal to 1 Hz), the higher limit ω_j of the frequency range considered is assumed equal to $2\pi 100\,\frac{rad}{s}$ (frequency equal to 100 Hz, which is the frequency of the electromagnetic loads). The following mass and stiffness proportionality coefficients are then calculated: $\alpha = 12.6\frac{1}{s}$ and $\beta = 6.3\ e-5\ s$.

The initial deformation due to the DC component, is not here considered due to software limitations which don't allow the user to introduce a pre-stress to an harmonic analysis if some loads are imported from Maxwell, as in this case. This limitation will be overcame in future Ansys releases and for this reason will be taken into account in further developments.

Considering a constant temperature at ambient values is also an approximation which could lead to substantial differences from the real situation, where temperatures are higher due to Joule effect heating. Experience shows that noise emissions are different at different temperatures because of the differential thermal expansion between parts, and for this reason this assumption will be removed in further developments.

Since only the current harmonic at 50 Hz has been considered in the electromagnetic simulation and since the electromagnetic forces have double the frequency of the current, i.e. 100 Hz, the analysis is run at 100 Hz only.

6.2.3 *Materials*

The materials assigned to the different parts composing the structure of the transformer are copied from the datasheets provided by suppliers. The properties of the material assigned to the winding are calculated through the beam model already mentioned in Paragraph 7.4.2 and described in Appendix. All the materials are assumed isotropic. Table 6 resumes the properties assigned to all the materials.

Table 6 - Mechanical properties of materials

Component	Material	Young's modulus, E [GPa]	Poisson ratio, ν	Density, ρ $[\frac{Kg}{m^3}]$
Winding	Homogenized	31.7	0.3	2230
Core and Frame	Structural Steel	200	0.3	7850
Air-Gaps and Tube	G11_fiberglass	24	0.3	1900
Sticks	PRFV fiberglass	40	0.3	2000
Compensating plate	GPO3 fiberglass	11	0.3	1800

6.2.4 *Mesh*

Ansys Mechanical allows to use both tetrahedral and hexahedral elements. The choice of mesh elements is driven by both results accuracy and force interpolation quality. Hexahedral quadratic mesh is known to be the best choice in terms of accuracy and convergence. For this reason, it is assigned to all the parts, apart from the core, which is meshed with tetrahedral quadratic elements. The choice of a tetrahedral mesh for the core deserves some observations. Force interpolation on the core is critical in this model, due to the fact that Maxwell and magnetostrictive forces are mainly concentrated close to the air-gaps. To obtain an acceptable error in the force interpolation (< 5%), the mesh has to be very refined in these regions. If a structured hexahedral mesh is used, the number of elements will be huge. A transitioning tetrahedral mesh, refined close to the air gaps and coarser far from them, has been proven to be the best choice in terms of model size and solution accuracy. In order to verify that the accuracy of the model is not affected by the usage of tetrahedral mesh, a modal analysis has been performed and compared to a reference modal analysis in which only hexahedral elements have been used. The computed difference between the first 20 eigenfrequencies of the two models has been found to be lower than 0.2%, as shown on Figure 65.

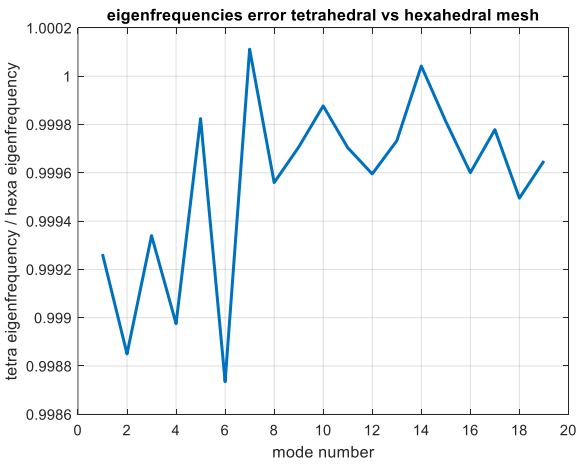

Figure 65 – Ratio between eigenfrequencies computed with tetrahedral and hexahedral core mesh

The mesh quality is checked looking at the Jacobian computed at the Gauss points of the elements. Elements of the frame parts (vertical plates and clamping profiles) are intentionally chosen with a relatively high aspect ratio to reduce the model size. However, a sensitivity analysis on the mesh of each structural part based on modal analyses has been performed and such element distortion has been proven to be acceptable. The structural mesh is shown on Figure 66.

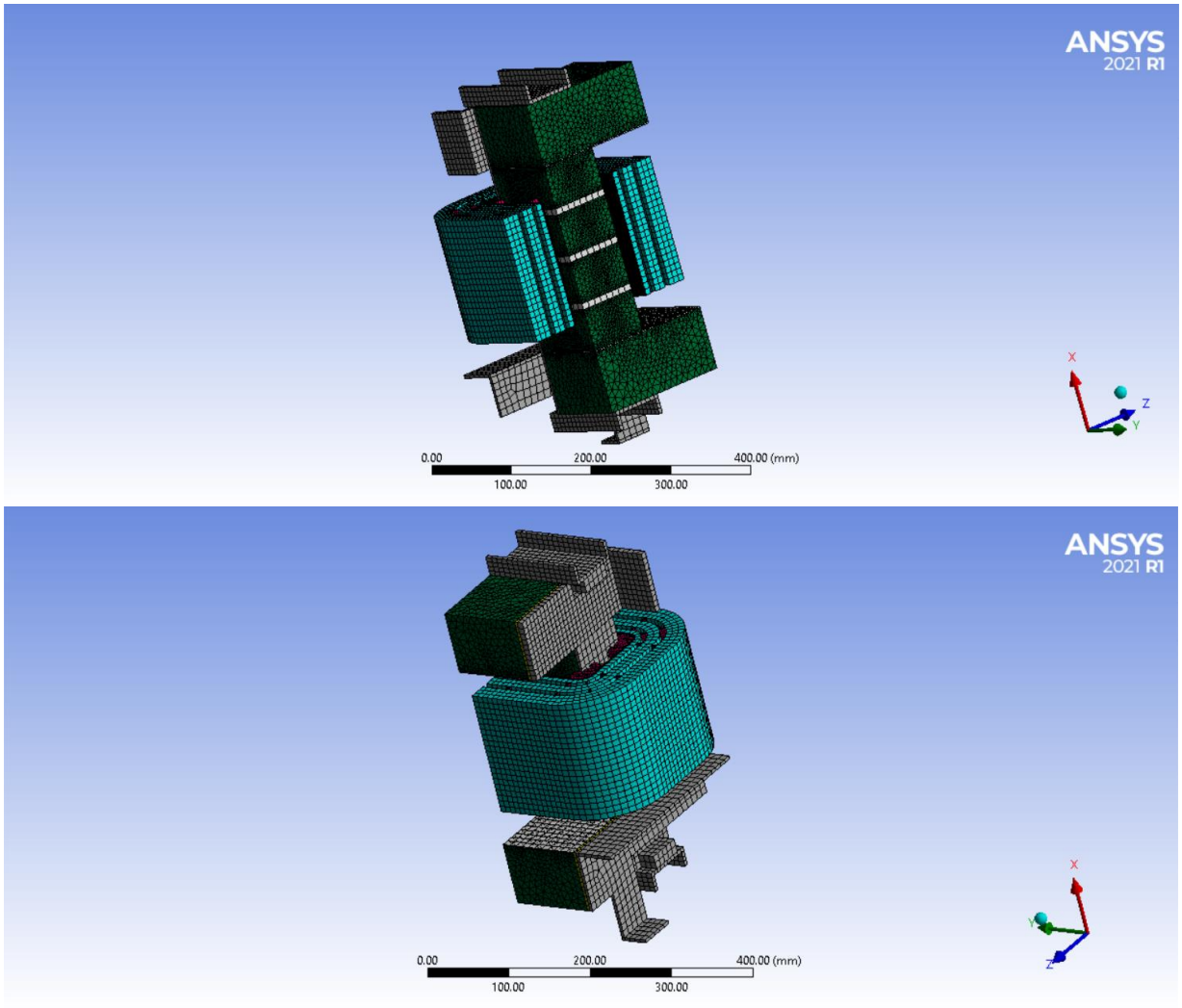

Figure 66 - Structural Mesh

6.2.5 Loads and boundary conditions

The loads applied to the structure when performing harmonic analysis are imported and mapped from the Maxwell simulation. Nodal volumetric forces are mapped taking into account the volumetric distribution of the forces. Multiple load import commands can be defined. For each of them the Maxwell simulation from which the loads have to be imported as well as the geometry on which the loads have to be mapped can be arbitrarily chosen. Two load import commands are needed: one for Lorentz forces, which are mapped from the Eddy Current simulation used to compute the Lorentz forces onto the winding geometry, the second one for magnetostrictive and Maxwell forces into the core, which are mapped from the relative Maxwell simulation into the core geometry. After having imported the loads, the quality of the interpolation can be checked. Ansys provides a table in which the ratio between the resultants calculated in Maxwell and the resultants of the interpolated loads is computed, as shown on

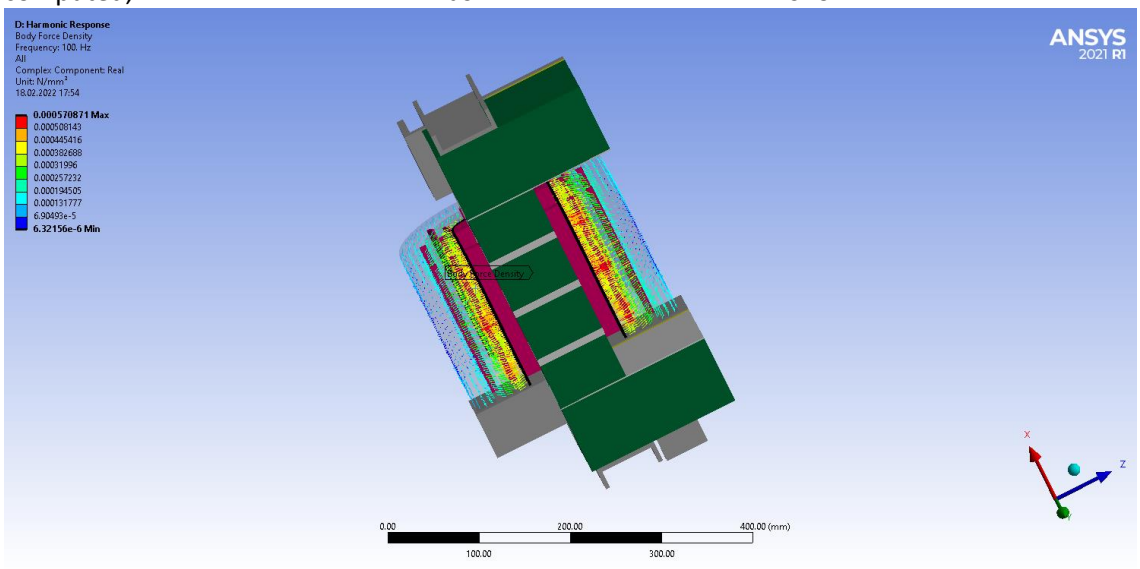

Have Force option

Exporting Volume Force Density Without Scaling...

Object	Total Force From Maxwell 3D	Total Force Mapped	Ratio
Winding_Homogenized_Solid	((0N, 0N), (-63.177N, -5.71862E-09N), (22.1405N, 2.0091E-09N))	((-0.390361N, -3.5642E-11N), (-61.9714N, -5.61115E-09N), (21.8356N, 1.98233E-09N))	1.01883
Winding_Homogenized_Solid_1	((0N, 0N), (-117.876N, -1.05984E-08N), (9.62166N, 8.7071E-10N))	((-0.0638941N, -5.99224E-12N), (-118.511N, -1.06554E-08N), (9.47912N, 8.58184E-10N))	0.994777
Winding_Homogenized_Solid_2	((0N, 0N), (-66.2243N, -5.9495E-09N), (2.81998N, 2.5468E-10N))	((0.269383N, 2.41219E-11N), (-67.5203N, -6.06592E-09N), (2.44182N, 2.20791E-10N))	0.981046

Figure 67. The resultants are calculated in Maxwell as the integral of the volumetric forces on the volume of the considered solid. Acceptable ratios are those between 0.95 and 1.05, i.e. only interpolation errors below 5% are conventionally acceptable.

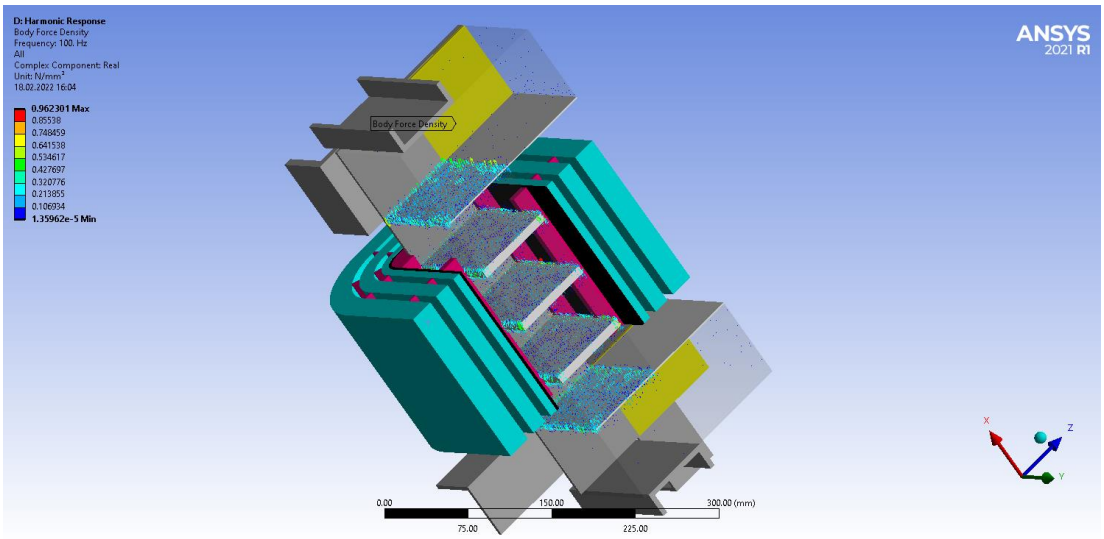

Have Force option

Exporting Volume Force Density Without Scaling...

Object	Total Force From Maxwell 3D	Total Force Mapped	Ratio
Solid	((-5388.22N, -4.83572E-07N), (11.5508N, 5.90031E-10N), (-129.399N, -1.20983E-08N))	((-5344.71N, -4.79611E-07N), (12.0971N, 6.29949E-10N), (-164.955N, -1.53528E-08N))	1.00795
Solid_1	((1037.42N, 9.31899E-08N), (1.64304N, 2.26376E-10N), (37.107N, 3.30669E-09N))	((1019.31N, 9.1561E-08N), (0.925783N, 1.59353E-10N), (35.4995N, 3.16001E-09N))	1.0178
Solid_2	((-106.494N, -1.11681E-08N), (-52.0202N, -5.33934E-09N), (1.1029N, 1.97132E-09N))	((-110.164N, -1.15547E-08N), (-49.1972N, -4.98422E-09N), (2.04536N, 2.06141E-09N))	0.982248

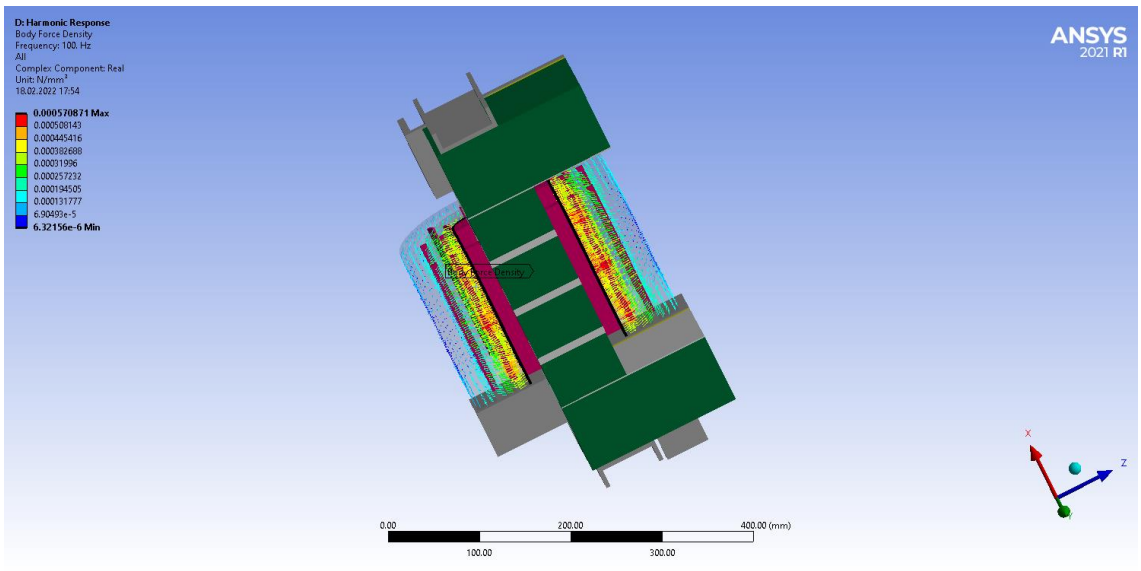

Have Force option

Exporting Volume Force Density Without Scaling...

Object	Total Force From Maxwell 3D	Total Force Mapped	Ratio
Winding_Homogenized_Solid	((0N, 0N), (-63.177N, -5.71862E-09N), (22.1405N, 2.0091E-09N))	((-0.390361N, -3.5642E-11N), (-61.9714N, -5.61115E-09N), (21.8356N, 1.98233E-09N))	1.01883
Winding_Homogenized_Solid_1	((0N, 0N), (-117.876N, -1.05984E-08N), (9.62166N, 8.7071E-10N))	((-0.0638941N, -5.99224E-12N), (-118.511N, -1.06554E-08N), (9.47912N, 8.58184E-10N))	0.994777
Winding_Homogenized_Solid_2	((0N, 0N), (-66.2243N, -5.9495E-09N), (2.81998N, 2.5468E-10N))	((0.269383N, 2.41219E-11N), (-67.5203N, -6.06592E-09N), (2.44182N, 2.20791E-10N))	0.981046

Figure 67 - Core forces interpolation (top) and Lorentz forces interpolation (bottom)

Concerning boundary conditions, the structural model must be constrained to avoid rigid body motions letting at the same time the structure to deform according to its operative deformation shapes. In this case, the two symmetries with respect to XY and XZ planes are exploited constraining the normal

displacements of the faces leading on the same planes, i.e. imposing a *frictionless support*. This constrains rigid body motions in the Y and Z directions. The rigid motion in the X direction is finally constrained imposing a null displacement of the lower clamping profile surface parallel to the YZ plane, as shown on Figure 68. This almost corresponds to suppose the transformer leaning on the ground.

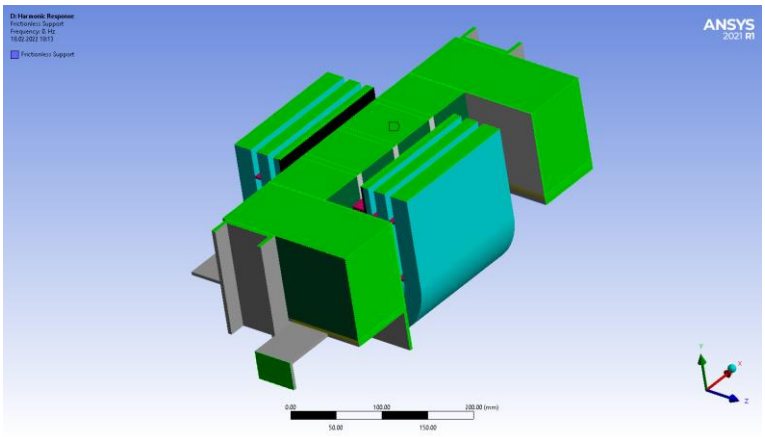

Figure 68 - Frictionless support boundary conditions

Finally, contacts between the different parts must be defined. In principle, the interaction between the different parts of a transformer is not straightforward. The contacts between the frame and the core, where different clamping pressures lead to different contacts status, are not intuitive. As already mentioned in Paragraph 7.5, in order to choose these contacts in a reasonable way, a model in which the effect of the pressures applied through the tightening torques is simulated, in order to visualize the contact status between all the different structural parts after the clamping. The model is presented in Appendix. The results of the analysis show that bonding between all the part seems to be a reasonable choice, except for the central region of the yokes, where a *no-separation* contact seems to be a more realistic choice. This is due to the lower pressure applied in this central region of the yoke. However, the sensitivity analysis run to understand the influence of different number of laminations on the ERP has shown that bonding everything together gives acceptable results (last row of Table 2). In conclusion, all the parts are considered bonded together. After having defined the contacts, the summary of the initial status of the contacts can be output in order to check if some excessive penetration or gap are present, as shown on Figure 69.

Initial Information

For additional options, please visit the context menu for this table (right mouse button)

Name	Contact Side	Type	Status	Number Contacting	Penetration (mm)	Gap (mm)	Geometric Penetration (mm)	Geometric Gap (mm)	Resulting Pinball (mm)	Real Constant
Contact Region 2	Contact	Bonded	Inactive	N/A	N/A	N/A	N/A	N/A	N/A	47.
Contact Region 2	Target	Bonded	Closed	330.	7.9199e-028	0.	4.6419e-006	2.3325e-006	1.0135	48.
Contact Region 3	Contact	Bonded	Inactive	N/A	N/A	N/A	N/A	N/A	N/A	49.
Contact Region 3	Target	Bonded	Closed	42.	6.0373e-028	0.	0.	1.9676e-006	2.4432	50.
Contact Region 4	Contact	Bonded	Inactive	N/A	N/A	N/A	N/A	N/A	N/A	51.
Contact Region 4	Target	Bonded	Closed	159.	1.0682e-019	0.	5.2355e-006	5.5065e-006	1.6472	52.
Contact Region 6	Contact	Bonded	Inactive	N/A	N/A	N/A	N/A	N/A	N/A	53.
Contact Region 6	Target	Bonded	Closed	2508.	1.7308e-027	0.	2.5742e-007	2.7981e-006	0.90595	54.
Contact Region 11	Contact	Bonded	Closed	1197.	5.8651e-014	0.	5.6843e-014	4.888e-005	0.73338	55.
Contact Region 11	Target	Bonded	Inactive	N/A	N/A	N/A	N/A	N/A	N/A	56.
Contact Region 13	Contact	Bonded	Closed	42.	3.7941e-028	0.	8.5265e-014	5.6843e-014	1.0388	57.
Contact Region 13	Target	Bonded	Inactive	N/A	N/A	N/A	N/A	N/A	N/A	58.
Contact Region 14	Contact	Bonded	Closed	180.	2.8422e-014	0.	5.6843e-014	5.6843e-014	1.0388	59.
Contact Region 14	Target	Bonded	Inactive	N/A	N/A	N/A	N/A	N/A	N/A	60.
Contact Region 15	Contact	Bonded	Inactive	N/A	N/A	N/A	N/A	N/A	N/A	61.
Contact Region 15	Target	Bonded	Closed	18506	1.9499e-027	0.	1.7053e-013	1.7053e-013	0.69771	62.
Contact Region 17	Contact	Bonded	Closed	280.	1.1369e-013	0.	1.1369e-013	1.1369e-013	1.2723	63.
Contact Region 17	Target	Bonded	Inactive	N/A	N/A	N/A	N/A	N/A	N/A	64.
Contact Region 18	Contact	Bonded	Closed	336.	8.3141e-028	0.	1.4578e-006	7.159e-006	1.	65.
Contact Region 18	Target	Bonded	Inactive	N/A	N/A	N/A	N/A	N/A	N/A	66.
Contact Region 19	Contact	Bonded	Closed	336.	2.8422e-014	0.	4.2633e-014	4.2633e-014	1.	67.
Contact Region 19	Target	Bonded	Inactive	N/A	N/A	N/A	N/A	N/A	N/A	68.
Contact Region 20	Contact	Bonded	Inactive	N/A	N/A	N/A	N/A	N/A	N/A	69.
Contact Region 20	Target	Bonded	Closed	1452.	5.8601e-014	0.	3.8207e-005	7.7256e-006	0.81867	70.
Contact Region 21	Contact	Bonded	Closed	1728.	5.9417e-014	0.	1.7276e-005	2.7624e-005	0.66666	71.
Contact Region 21	Target	Bonded	Inactive	N/A	N/A	N/A	N/A	N/A	N/A	72.

Figure 69 - Ansys Contact Tool initial information

6.2.6 Post processing

For postprocessing activity, some checks can be run in order to understand if the model is behaving as expected. Unfortunately, analytical models to predict the response of such complex structures are not available. However, some general behaviors are expected. As a first step, a visual inspection of the deformation of the structure should be run to check that all the contacts are behaving as expected. Excessive penetration of two different parts suggest that the contact hasn't been defined correctly or a finer mesh is needed. Figure 70 shows the deformed shape of the traction reactor and the velocity contour. A maximum and a minimum vibration velocity of *0.176 mm/s* and *0.039 mm/s* are computed. These values will be compared with the interpolated velocity on the acoustic model to judge the interpolation quality of velocities.

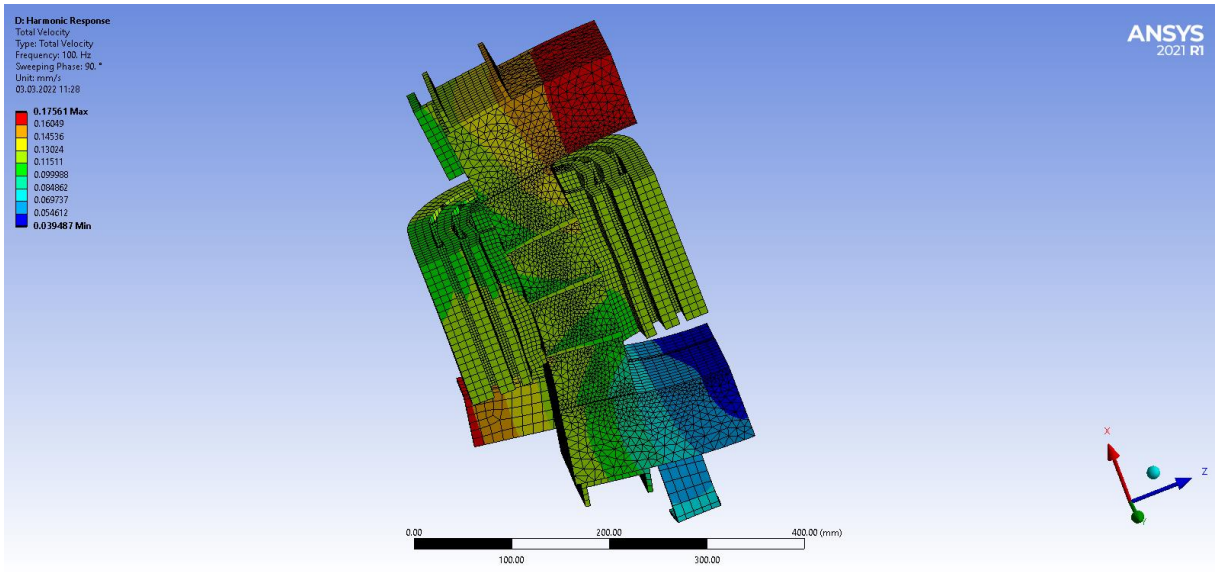

Figure 70 -Deformed shape and velocity contour of the structural model. 6.3e+6 scale. Max velocity = 0.173 mm/s

A useful quantity to look at is Equivalent Radiated Power (ERP) defined in Equation 23, which is an integral measure of the acoustic power generated by the vibrating structure at each considered frequency. ρ is the density of the fluid surrounding the transformer, c is the sound speed in the fluid, A is the vibrating surface area, $< v_n^2 >$ is the surface averaged mean-square-velocity. ERP is automatically calculated by Ansys once it is requested as output.

$$ERP = \rho c A < v_n^2 > \quad (23)$$

Comparing it with the Sound Power Level (which is computed later in the acoustic analysis), the radiation efficiency σ can be calculated using Equation 24. Radiation efficiency is a measure of how much of the power generated by the source is actually delivered to the air. This gives an idea of which frequencies are the most critical ones in terms of noise emission.

$$\sigma = \frac{SPL}{ERP} \quad (24)$$

Table 7 reports the ERP of all the radiating surfaces. It is evident that ERP in x direction is dominating. This is due to the fact that core forces are mainly directed in x (vertical) direction. The vertical component of core forces is more than one order of magnitude higher than the other components. The reason why force along x direction is predominant is the following: both Maxwell and magnetostrictive forces are mainly directed along x because the higher magnetic field variations occur in x direction. Maxwell stress and magnetostrictive deformation (and so magnetostrictive stress) both depend on magnetic field. In the context of the weak formulation of the mechanical problem, volumetric forces are linearly dependent on the space variation (divergence) of stresses. If x direction is the direction where the highest variation of *B* occurs, then it is also the direction along which the highest variation of Maxwell and magnetostrictive stresses occur. Concluding, volumetric forces are predominant in x direction.

A particular result is that the upper and lower surfaces (oriented as x direction) of the winding generate an ERP higher than the lateral surfaces. However, this is not due to the Lorentz forces, but it is due to the transmission of the vertical movement of the core to the winding. An analysis in which only Lorentz forces are applied have been run. An ERP for the upper and lower winding surfaces equal to *16.727 dB* has been computed and an ERP equal to *35.758 dB* for the lateral surfaces. This proves that the ERP from the upper and lower surfaces of the winding generated by Lorentz forces is negligible compared to the one from the lateral surfaces. The ERP generated by the upper and lower surfaces is completely dominated by the coupling with the core. It can be concluded that choosing an equivalent material of the winding for computing accurately only the noise emitted in radial direction, as it has been done, seems to be a good choice.

$ERP = \rho c A < v_n^2 > \sigma = \frac{SPL}{ERP}$

Table 7 - Computed ERP for different parts in different directions

Surfaces	ERP [dB]
Winding x	50.725
Lateral Winding	38.355
Core x	50.633
Core y	27.983
Core z	35.994

As a final step, a modal analysis of the core and of the winding has been run to understand which the frequencies of the most participating modes are and if they lead near to the excitation frequencies. This allows to better judge the obtained results in terms of vibration velocity at different excitation frequencies. Figure 71 shows the core and winding modes which can be reasonably considered the most participating ones. It can be noticed that for the computation of the core eigenfrequencies, some clamping profiles have been removed. This has been done in order to avoid local modes which would lead to the needing of computing an excessive number of modes to capture the interesting one. For this reason, the resonance frequencies of the whole core assembly are probably slightly underestimated, but acceptable for the purpose of the analysis. The computed eigenfrequencies of the core and the winding are *1658.3 Hz* and *2233.6 Hz* respectively.

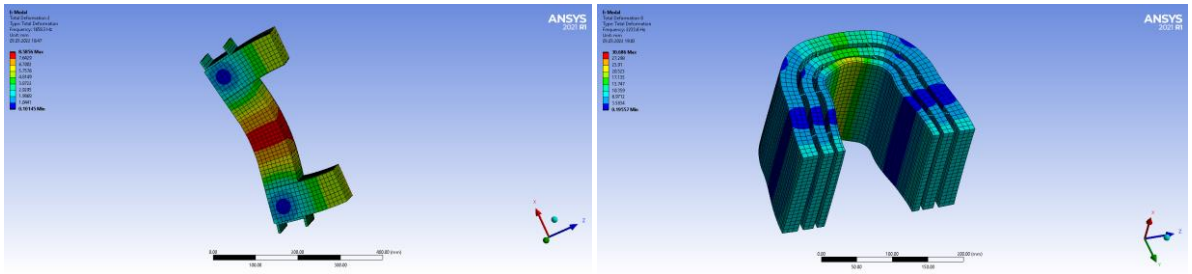

Figure 71 - Core and winding eigenmodes and eigenfrequencies

6.3 Acoustic model

When dealing with acoustic model, multiple models have to be set up for different subranges of frequencies. This is due to the fact that acoustic domain modeling, in particular its dimension and the mesh size, depends on the frequency range under study. For low frequencies, the acoustic domain should be larger and the mesh coarser, whereas for high frequencies the acoustic domain should be smaller but the mesh finer. It is intuitive to understand that if the range of frequency is wide (from low to high frequencies), the model will require a relatively big acoustic domain (for low frequencies) with a relatively fine mesh (for high frequency), leading to a computationally heavy model. For this reason, dividing the frequency range in more subranges, using different acoustic domain for each subrange, is more computationally efficient.

The Workbench project page including the acoustic model is shown on Figure 72. Surface velocities of the structure computed in the harmonic analysis are imported into the acoustic model through the connection between Harmonic Response Solution and Harmonic Acoustic Setup. In this chapter, the model used to compute the acoustic response of the structure is presented.

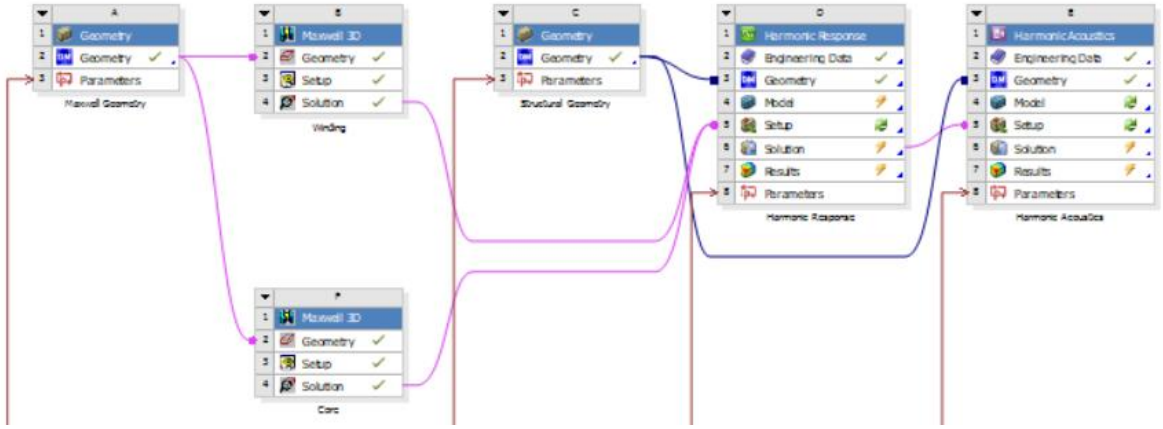

Figure 72 - Complete Workflow for acoustic analyses

6.3.1 Geometry

In the context of acoustic analyses, the external fluid domain must be modeled. A box enclosing the structure is modeled and the structure geometry is subtracted from the same box. Since the same structural geometry is used for doing this, care must be taken when preparing the geometry for the structural model, avoiding discontinuities in the air domain, as already mentioned in Paragraph 9.2.1. Several sensitivity studies based on Monopole and Dipole models have been performed to understand which dimension and shape of the acoustic domain should be used to optimize computational efficiency and accuracy. These studies are presented in Appendix 10.3. An acoustic domain with a box shape and the usage of PML elements has been proven to be the best solution in terms of accuracy and convergence. The acoustic domain geometric center must be coincident with the geometric center of the structural model. As a rule of thumb, the shortest distance between the radiating surface and the inner surface of PML region should be at least 2/3 of the largest acoustic wavelength. The PML region should be such that at least 2 layers of non-distorted PML elements can be used. Figure 73 shows the acoustic geometry in which $1/4^{th}$ symmetry has been exploited.

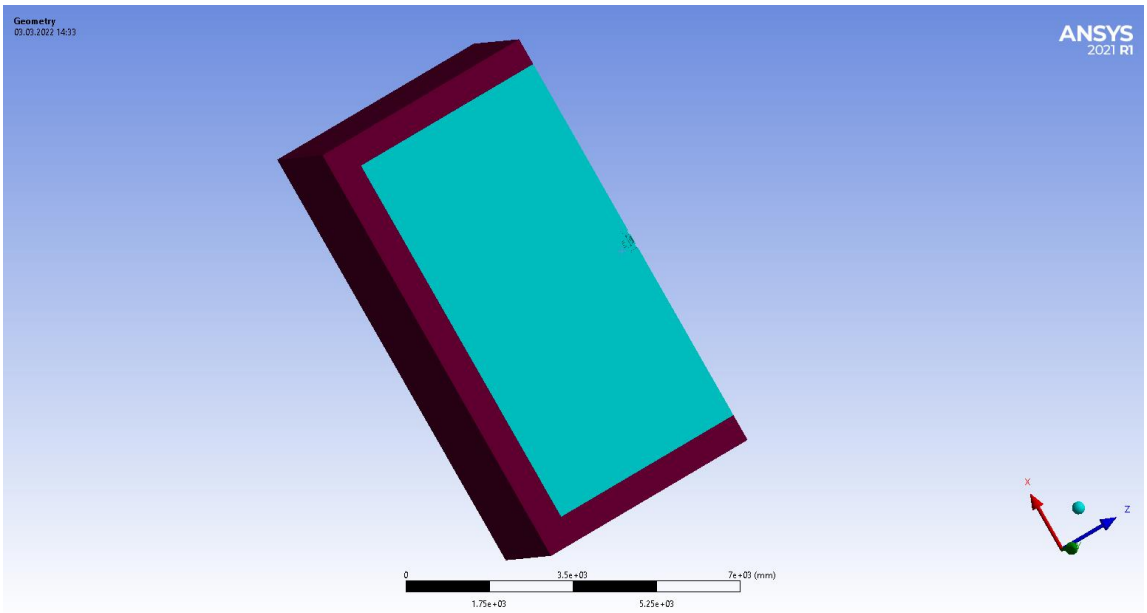

Figure 73 - Example of acoustic domain

6.3.2 Analysis type

The following assumptions have been made:

- Linear behavior (linear dependance between velocity and pressure, constant material properties, small pressure variations)
- Harmonic excitation (periodic velocity excitation)
- No fluid-structure interaction (FSI) – one way coupling
- Compressible and non-viscous fluid
- Irrotational flow
- Adiabatic and reversible pressure change
- Only steady state is considered.

For this reason, a harmonic acoustic analysis is performed. The hypothesis of small pressure variations is a typical hypothesis for subsonic problems, in which discontinuities like shock waves are not expected. This is of course an acceptable approximation when dealing with vibro-acoustics in the context of transformers.

The hypothesis of no FSI is a reasonable hypothesis in cases in which the pressure variations are not expected to exert a significant force on the structure. As already mentioned in Chapter 7.3, Equation 14 can be used to know a-priori if FSI should be modeled. In this case, α_c is equal to *0.1*, which means no FSI is needed. This hypothesis is the reason why the structural bodies don't have to be modeled and can be suppressed in the acoustic analysis. Only their surfaces, where the velocities are mapped from the harmonic structural analysis are needed.

The hypothesis of compressible fluid is mandatory when dealing with acoustic. By definition, a wave is a variation of pressure in space and time. Only considering a compressible fluid, such pressure variation can occur.

The hypothesis of non-viscous fluid applies to all the fluid-dynamics problems where only the solution far from the body surfaces are of interested, being the viscous effects limited to a thin layer next to

the body surfaces (boundary layer). Since in this case only the far-field solution is of interest, viscous effect can be neglected. This means that only the velocities normal to the surfaces generate noise.

6.3.3 Materials

The material assigned to the enclosure and the PML region is air. Reference pressure is set equal to *2e-11 MPa,* which correspond to the minimum audible pressure variation. This quantity is used as the reference pressure to compute sound pressure level in dB scale. The reference static pressure, instead, is set equal to *0.010132 MPa*. Finally, density and sound speed are set equal to $1.225\ \frac{Kg}{m^3}$ and $346.25\ \frac{m}{s}$ respectively.

6.3.4 Mesh

When dealing with acoustic analyses, both quadratic hexahedral (*FLUID 220*) and quadratic tetrahedral (*FLUID 221*) elements are available. The finite elements used in acoustics when fluid-structure interaction is neglected are elements with 1 degree of freedom only per node, i.e. acoustic pressure. Meshing the acoustic domain using hexahedral elements is not straightforward and usually leads to high mesh distortion, due to the complexity of the geometry close to the structural surfaces. For this reason, tetrahedral quadratic elements have been proven to be an acceptable compromise in terms of accuracy and convergence, based on the studies on Monopole and Dipole. As a rule of thumb, the element size should not be greater than 1/4th of the shortest acoustic wavelength. In this case an element size equal to *200 mm* (1/17th) of the sound wavelength is used since it doesn't affect negatively the computation time (the most of the computational time is spent in the electromagnetic and structural analyses).

Conformal mesh must be used, since contacts decrease the accuracy of the solution introducing reflections. Same consideration is valid for wedges and pyramids elements, which can introduce reflections due to the change of shape functions. Finally, care must be taken to the meshing of the surfaces on which velocities are mapped, since it influences the quality of the interpolation. As a rule of thumb, same elements dimension as the one used in the structural analysis should be used for such surfaces. Figure 74 shows the acoustic domain mesh.

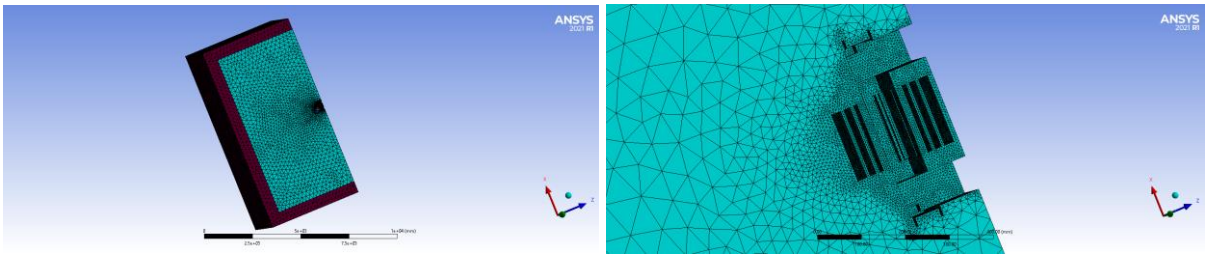

Figure 74 - Acoustic domain mesh

Mesh quality is checked in terms of element Jacobian evaluated at the Gauss point. Jacobian is a measure of the element distortion and should be always under control. In this case, as shown on Figure 75, almost all the elements have a Jacobian near to 1, which means a high-quality mesh is obtained.

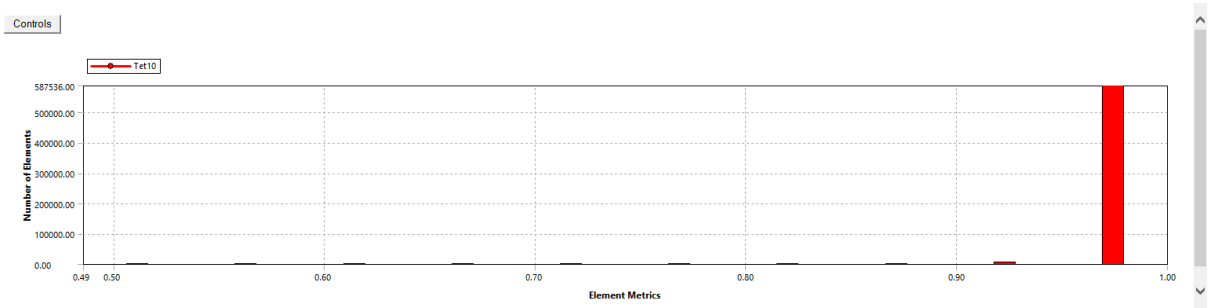

Figure 75 - Elements Jacobian evaluated at the Gauss points

6.3.5 Excitations and boundary conditions

The excitation is provided by the vibration velocities of the transformer surface, mapped from the harmonic structural analysis. Once the velocities are imported from the structural harmonic analysis, they can be mapped and interpolated on the exciting surfaces. As in the case of force interpolation, the user should check that the difference between the velocities computed in the structural harmonic analysis and the ones here interpolated is negligible. An easy and quick way is to check the maximum and minimum values only, which are displayed in the contour plots. Also, Ansys provides a summary of the interpolation showing if some nodes are not mapped or if some source nodes are outside the target geometry. A number of these nodes different from zero indicates that some error has occurred in the acoustic meshing. Figure 76 shows the interpolated velocity and the mentioned summary. A maximum and minimum interpolated velocity of *0.176 mm/s* and *0.039 mm/s* are obtained, which are identical to the computed values in the structural harmonics analysis. Same consideration is valid for all the values showed in the contour legend. This means that velocities interpolation is performed accurately.

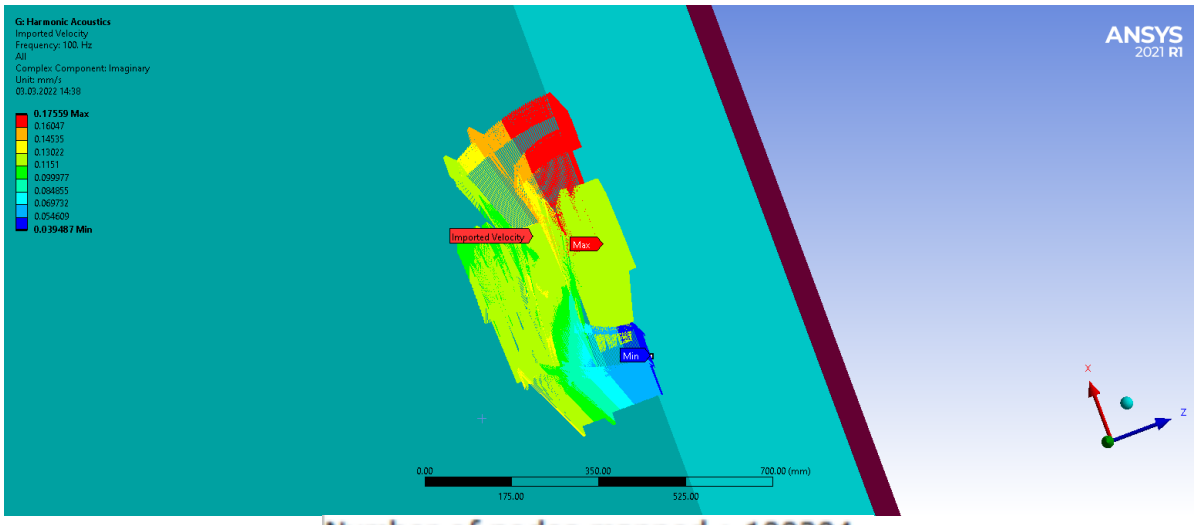

Figure 76 - Velocity interpolation

Regarding boundary conditions, if no boundary conditions are defined on a surface, Ansys automatically imposes a perfectly reflecting boundary condition (rigid wall). For this reason, it is not needed to define any boundary condition on the exciting surfaces (natural boundary conditions), since they act as exciting and reflecting surfaces. PML region must be defined explicitly selecting which region has to be meshed with such elements. The Dirichlet boundary condition $p = 0$ is automatically imposed on the PML external surfaces once the PML region is defined. Finally, symmetries are defined

on the faces lying on symmetry planes. Figure 77 shows the selected faces for symmetry boundary conditions.

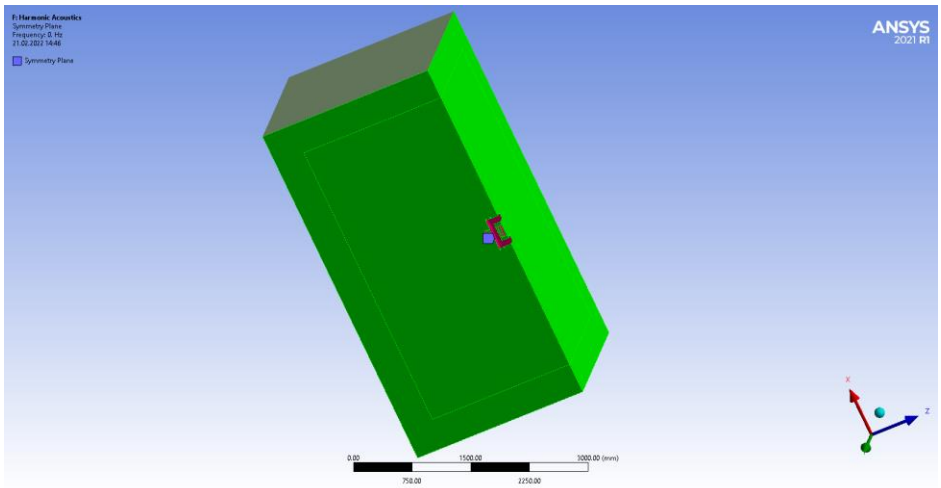

Figure 77 - Symmetry planes

6.3.6 Post processing

Unfortunately acoustics analytical models for this specific case are not available due to the complexity of the problem. However, some checks can be run in order to understand if the general physical mechanisms are violated. The first check is that of computing the pressure phase, defined in Equation 25, where $Im(p)$ and $Re(p)$ indicate the imaginary and the real part of the acoustic pressure respectively and the *atan2* function is used instead of the *tan* function to avoid infinite values in points where imaginary and real part of the pressure are out-of-phase. The acoustic pressure phase shows the shape of the wavefronts. This should have a regular pattern in the whole domain and it should approach a spherical shape far from the source, as shown on Figure 78.

$$\phi = atan2\big(Im(p), Re(p)\big) \qquad (25)$$

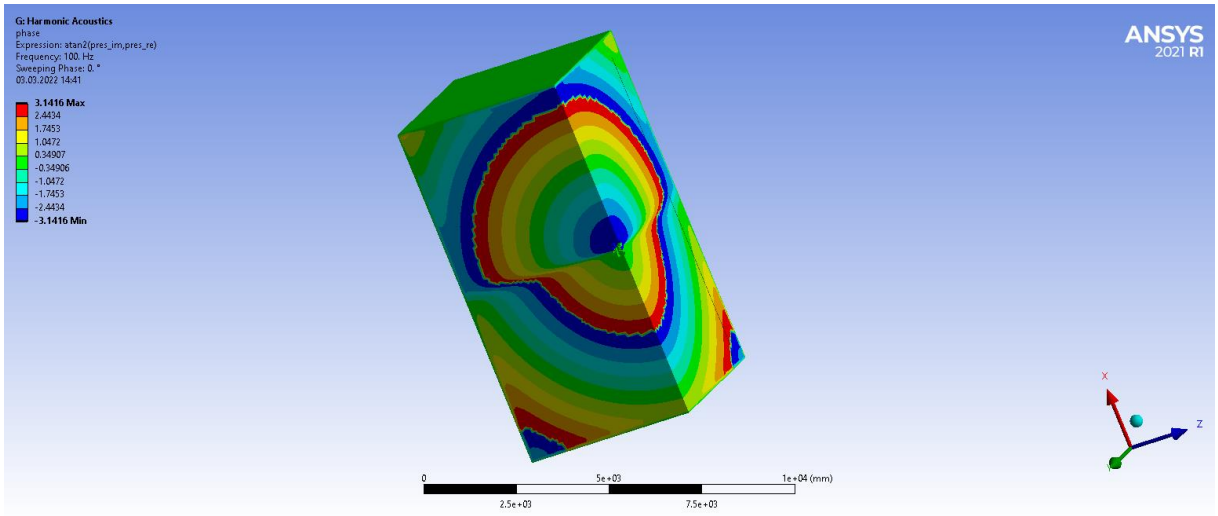

Figure 78 - Phase contour

A second check is that of plotting the Sound Pressure Level along some arbitrary paths. Keeping two points on this path far enough from the source but still inside the enclosure (not in the PML region)

and one at double the distance of the other one, a difference of 6 dB should be observed. If this happens, it means that the noise propagation in the far-field is correctly simulated in the modeled domain. In this case, SPL is plotted along the path shown on Figure 79. In the specific example the SPL computed at *3110 mm* from the source is *15.677 dB* while the SPL computed at *6220 mm* is *9.79 dB*, i.e. almost exactly 6 dB lower, as expected.

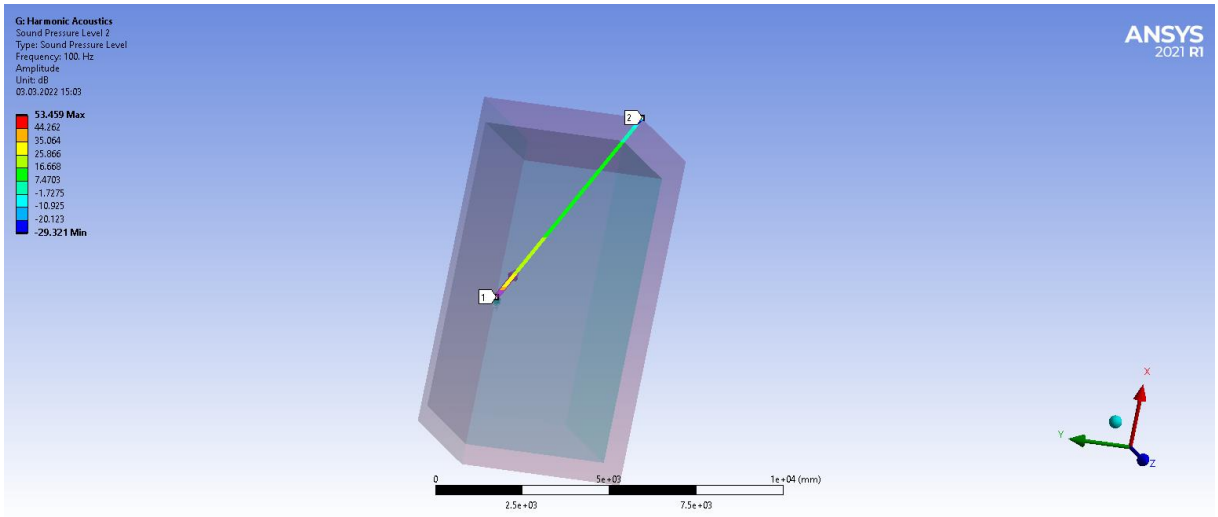

Figure 79 - Path along which SPL is computed

Far-field quantities as Sound Power, SPL, Directivity, can be computed in an arbitrary point outside the modeled acoustic domain. Far-field quantities are computed making use of the Equivalent Source Method, which allows to calculate acoustic quantities in a point outside the domain knowing the results on a surface inside the modeled domain, called Equivalent Source Surface. Figure 80 shows a schematic of the method. The Equivalent Source Surface is automatically set by Ansys and the user has only to choose which result to compute and where to compute it.

$$p(\vec{r}) = \oiint_{S[V]} \left[p(\vec{r}_s) \frac{\partial G(\vec{r}|\vec{r}_s)}{\partial n} - G(\vec{r}|\vec{r}_s) \frac{\partial p(\vec{r}_s)}{\partial n} \right] ds_s$$

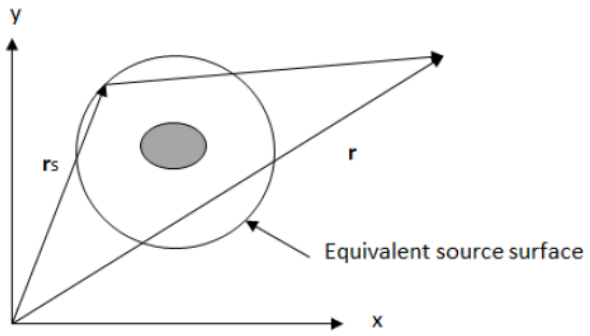

Figure 80 - Equivalent Source method

Figure 82 shows the directivity plot on a circular path enclosing the source. The lobes obtained are in accordance with the SPL contour, shown on Figure 81. Finally, the Sound Power is provided and a value of *35.981 dB* (*3.96e-9 W*) is computed. Applying the numerical technique presented in Appendix 10.4 for separating the contributions to the Sound Power, the results in Table 8 are obtained. The results show that the power generated by magnetostriction is higher than the one generated by Maxwell forces. This is an expected result, since magnetostrictive forces have been shown to be larger than

Maxwell forces. As a verification check, it can be easily noted that the sum of the 2nd, 3rd and 4th columns (after having opportunely transformed the values in physical units) gives the 1st column, i.e. the total Sound Power.

Table 8 - Contributions to Sound Power

Total Sound Power [dB]	Magnetostriction Sound Power [dB]	Maxwell Sound Power [dB]	Cross Sound Power [dB]
35.981	31.814	28.652	32.335

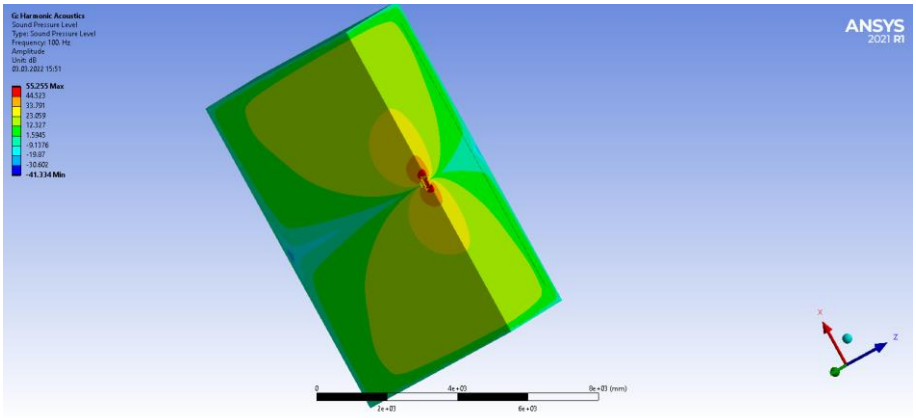

Figure 81 – Sound Pressure Level contour at 100 Hz

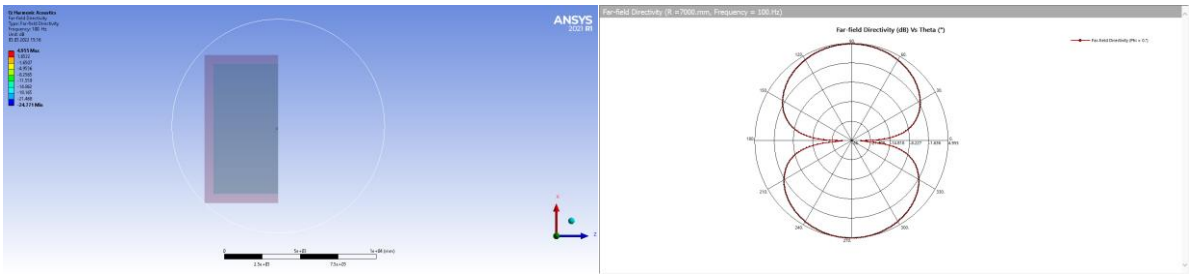

Figure 82 – Directivity plot at 100 Hz

At this point, it is possible to compute the radiation efficiency. The ERP emitted by all the external surfaces of the structure in contact with the air has been computed in the structural harmonic analysis. A value of *56.838 dB* (*4.82e-7*) is computed. A radiation efficiency $\sigma = 0.0082$ is calculated according to Equation 24.

The reason is associated to the coincidence frequencies. Figure 83 shows the analytical solution for the radiation efficiency of a monopole and a dipole, where ω_k denotes the coincidence frequency of the same. Since the solution obtained is actually similar to the dipole solution (two symmetric lobes), the dipole analytical solution gives a rough idea if a high or low radiation efficiency is expected.

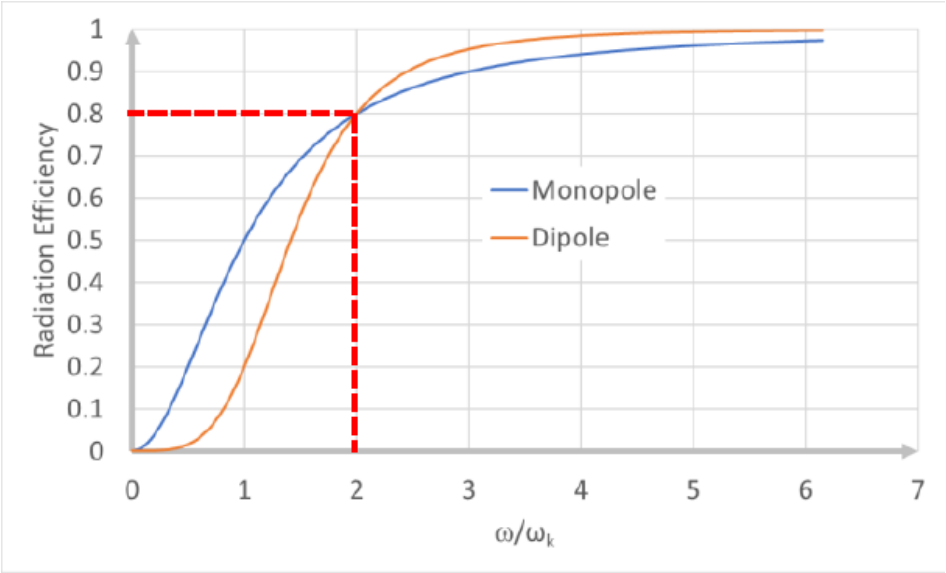

Figure 83 - Radiation efficiency of monopole and dipole. ω_k is the coincidence frequency.

In this case, bending of the winding and of the core (both yokes and columns) are involved, as it is visible on Figure 70. From the same figure it can be noticed that the wavelengths of the bending deformation of the columns and the yokes are equal to twice the length of the column (i.e. the vertical length of the core, equal to *400 mm*) and of the yokes (equal to *175 mm*). In other words, the deformed shapes of the yokes and the columns are showing half a bending wavelength. For this reason, the wavelength of the yokes and the columns bending modes can be considered twice the length of the same (*800 mm* and *350 mm*). Consequently, the coincidence frequencies of the core can be calculated according to Equation 26, where f_c denotes the coincidence frequency, c is the sound speed and $\lambda_{bending}$ is the wavelength of the bending deformation. In this case, coincidence frequencies are estimated to be *430 Hz* (columns) and *1000 Hz* (yokes). This means that the coincidence frequency of the columns is near to the excitation frequency, which should lead to a higher radiation efficiency. However, the noise produced by the bending of the columns is almost completely reflected by the winding and for this reason it is not radiated in the far-field. Instead, the coincidence frequency of the yoke, which is freely radiating along the x direction (no reflecting surfaces are present above and below the yokes), is 1/10th of the excitation frequency and a low radiation efficiency is expected. Finally, concerning winding, its higher bending wavelength can be considered as twice the length of the longer side of the winding (*220 mm*) and so its lower coincidence frequency can be estimated to be equal to *800 Hz.* However, has already shown, winding vibration is negligible compared to the core one.

$$f_c = \frac{c}{\lambda_{bending}} \quad (26)$$

For completeness, a transient analysis with two current harmonics (50 and 100 Hz) at the same amplitude has been run. The force spectrum show on Figure 84 is obtained, where harmonics at double the frequencies of the current (100 and 200 Hz) and harmonics equal to the sum and the difference of the current harmonics (150 and 50 Hz) are obtained, as expected. Computing the radiation efficiency for each frequency, the plot on Figure 85 is obtained. Radiation efficiency increases with the exciting frequency, since coincidence frequencies are approached. The shape of the curve is also similar to the Dipole's one.

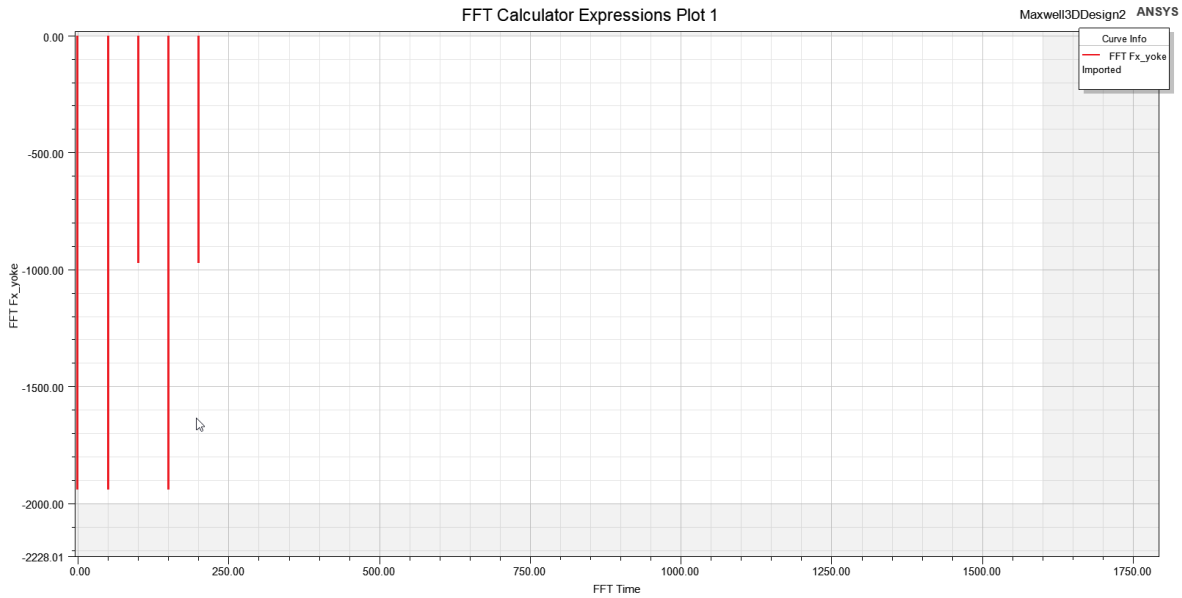

Figure 84 - Core forces FFT. Exciting current with harmonics at 50 and 100 Hz with same amplitude

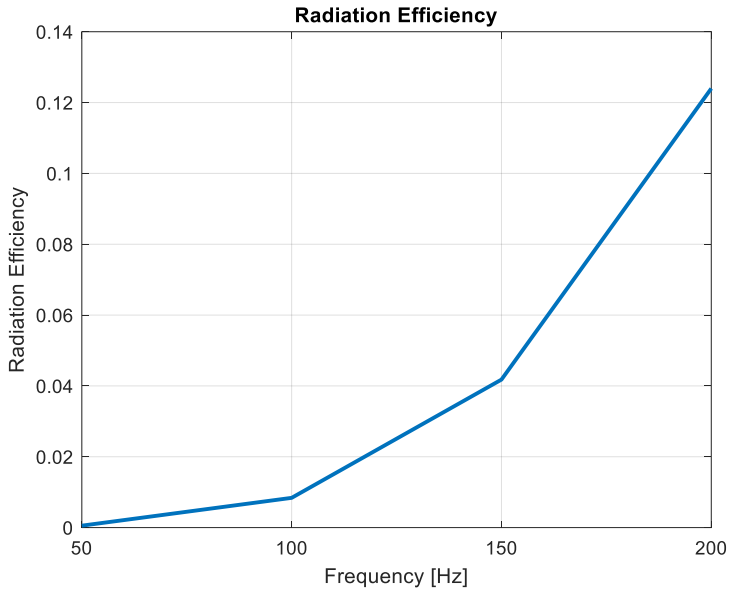

Figure 85 - Radiation Efficiency at different frequencies

7. Structure-Borne Noise

The following chapter briefly presents the mechanism of structure-borne noise for transformers and reactors, including an illustration of the theoretical background, as well as modeling and experimental techniques. Structure-borne noise is of absolute interest in transformers industry, since these machines are installed on trains, ships and submarines, where transformer vibrations are transmitted to the structure, leading to the generation of noise from the vibrating structural elements. As seen in the previous chapter, for the analyzed traction reactor the excitation at 100 Hz is not really critical from the air-borne noise point of view, due to low radiation efficiency in air. However, it could be critical in terms of structure-borne noise if the vibration is transmitted to a structural component whose eigenfrequencies lead near to the excitation frequency, generating resonances which amplify the excitation leading to increasing noise emission. Same is valid for coincidence frequencies. Moreover, trains, ships and submarines are closed environment which act as a resonance box, leading to an additional noise amplification through the generation of standing waves. Structure-borne noise is clearly related to the characterization of the noise sources presented in this work.

7.1 Theoretical background

The scope of structure-borne noise modeling and measurement, i.e. of the prediction and measurements of the transmitted vibrations from the source (transformer) to the structure to which it is attached, is that of choosing or designing an isolator to reduce the transmission of vibrational power in the operating conditions, fulfilling standards and specifications requirements. Isolators provide a de-coupling between the source vibration and the vibration of the structure to which the source is attached.

The main concept related to isolators is the so-called *Transmissibility,* defined in Equation 27. Transmissibility is defined as the ratio between the vibration amplitude of the structure and the source, i.e. as the ratio between the dynamic output to the dynamic input [32] [33]. If it is equal to *1*, all the energy will be transmitted from the source to the structure in a rigid way.

$$T = \frac{Y(f)}{X(f)} \qquad (27)$$

In general, output and input functions can be chosen arbitrarily. However, usually the measured quantities are accelerations or forces, due to the well-developed measuring systems as accelerometers and load cells, as well as their ease of use and their large bandwidths. The ratio between output acceleration and input force takes the name of *Inertance.* However, in structure-borne noise applications the most interesting quantity to be measured is the vibration velocity, since through them scalar quantities as power and kinetic energy can be computed. The ratio between output velocity and input force is defined as *Mobility* and it is usually computed indirectly through the derivative of Inertance. Standards and specifications for ships are defined in terms of mobility, as shown in Figure 30. Figure 86 shows the typical transmissibility curves for different damping ratios of isolators with viscous damping properties. To reduce the transmission of vibrations, the system has to be excited with frequencies above the resonance frequency of the isolator, i.e., on the right side of the plot (the so-called *isolation* region). This shows how the choice of an isolator deserves attention. The spectrum of the excitation has to be accurately characterized before choosing an isolator. It also worth mentioning that the installation of insulators leads in any case to an increase of the total weight of a system, which is a drawback in the field of transportation.

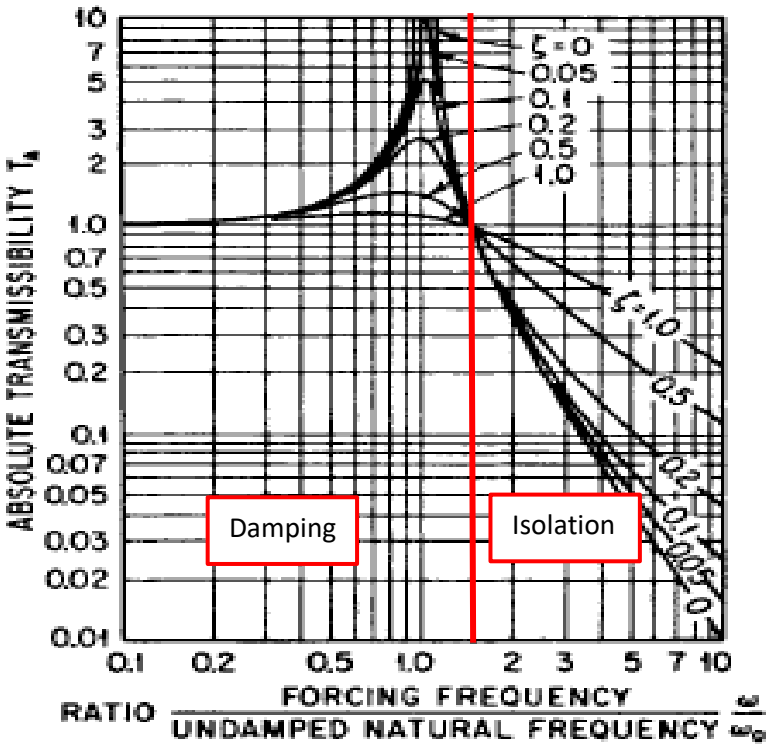

Figure 86 - Transmissibility of a viscous damper as function of frequency and damping ratio for single degree of freedom system [32]

Isolators are usually made of viscoelastic material, which also provide damping to the whole system, dissipating energy by means of friction or viscoelastic material deformation. The latter is the most common solution due to the relatively high damping capabilities of viscoelastic materials generated by the large hysteresis involved during their deformation, which leads to the transformation (dissipation) of mechanical energy into heat. An example of the stress-strain curve for a viscoelastic material is shown on Figure 87.

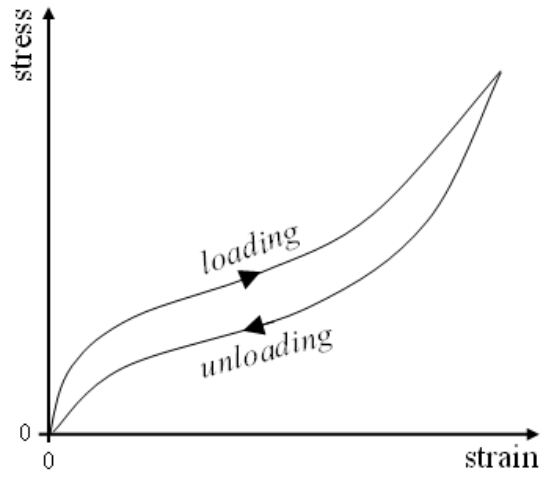

Figure 87 – Stress-strain curve of viscoelastic materials

Viscoelastic materials are characterized by a phase shift between stress and strain, i.e. the modulus of a viscoelastic material is a complex quantity that can be defined as in Equation 28, where E denotes the tensile modulus, E' is the tensile storage modulus, E'' is the tensile loss modulus, σ_0 is the

amplitude of the applied stress , ϵ_0 is the amplitude of the strain and δ is the phase shift between stress and deformation [34]. The term $\tan(\delta)$ gives a measure of the damping of the material. The same idea applies to the shear modulus. Viscoelastic materials are usually characterized through the temperature-frequency nomograms, in which the storage modulus, the loss modulus and the tangent of the phase are plotted as function of temperature and frequency, as shown on Figure 88

$$E = E' + iE'' \qquad (28.a)$$

$$E' = \frac{\sigma_0}{\epsilon_0}\cos(\delta) \qquad (28.b)$$

$$E'' = \frac{\sigma_0}{\epsilon_0}\sin(\delta) \qquad (28.c)$$

$$\tan(\delta) = \frac{E''}{E'} = \frac{G''}{G'} \qquad (28.d)$$

Figure 86 shows that higher damping ratios lead to lower transmissibility (higher isolation) near resonance frequency while transmissibility is larger for higher frequencies. Inverse considerations are valid in the case of low damping. This suggests that having a higher damping is not always a good choice, since transmissibility in the isolation region is increased.

7.2 Experimental methods

One of the most challenging problem regarding structure-borne noise is that of understanding which the energy flow paths in complex structures are and how energy is dissipated due to damping. The most diffused method is the *Statistical Energy Anal*ysis (SEA), especially in cases of complex structures with a high modal density, i.e. a high number of modes involved in the operative frequency range. SEA provides a strategy to identify the damping of a structure composed by several substructures based on the measuring of average quantities such as power *P* and average kinetic vibration energy *E.* The two parameters identified with this method are the *damping loss factor* η*,* i.e. the damping ratio and the *coupling loss factor* η_{ij}*,* which gives a measure of the energy dissipated when transferring vibrational energy from a subsystem *i* to a subsystem *j*. According to SEA, the power externally input into the subsystem *i* can be written according to Equation 29, where ω denotes the considered angular frequency, P_i the power dissipated by subsystem *i* due to its own damping, P_{ij} the power transferred to subsystem *j,* E_i and E_j the average kinetic energy of the subsystems *i* and j respectively [35].

$$P_{in,i} = P_{i,diss} + P_{ij} = \omega\eta_i E_i + \sum_{ij}^{n} \omega(\eta_{ij}E_i - \eta_{ji}E_j) \qquad (29)$$

At this point, the following procedure can be followed to identify the damping factors. For each subsystem *i* a power P_i is input and the power equilibrium expressed above is written in matrix form as following, where E_{ij} denotes the average kinetic energy of subsystem *i* when only subsystem *j* is excited. The equation can also be normalized dividing by the power input in the subsystem *i.*

$$\begin{Bmatrix} P_1 \\ 0 \\ \vdots \\ 0 \end{Bmatrix} = \omega \begin{bmatrix} \eta_{11}^0 & \eta_{12}^0 & \cdots & \eta_{1n}^0 \\ \eta_{21}^0 & \eta_{22}^0 & \cdots & \vdots \\ \vdots & \vdots & \ddots & \vdots \\ \eta_{k1}^0 & \cdots & \cdots & \eta_{kn}^0 \end{bmatrix} \begin{Bmatrix} E_{11} \\ E_{21} \\ \vdots \\ E_{k1} \end{Bmatrix} \xrightarrow{\text{Normalization}} \begin{Bmatrix} 1 \\ 0 \\ \vdots \\ 0 \end{Bmatrix} = \begin{bmatrix} \eta_{11}^0 & \eta_{12}^0 & \cdots & \eta_{1n}^0 \\ \eta_{21}^0 & \eta_{22}^0 & \cdots & \vdots \\ \vdots & \vdots & \ddots & \vdots \\ \eta_{k1}^0 & \cdots & \cdots & \eta_{kn}^0 \end{bmatrix} \begin{Bmatrix} E_{11}^n \\ E_{21}^n \\ \vdots \\ E_{k1}^n \end{Bmatrix}$$

The same procedure is applied to each subsystem, finally obtaining the following equation.

$$\begin{bmatrix} 1 & 0 & \cdots & 0 \\ 0 & 1 & 0 & 0 \\ \vdots & \vdots & \ddots & \vdots \\ 0 & 0 & \cdots & 1 \end{bmatrix} = \begin{bmatrix} \eta_{11}^0 & \eta_{12}^0 & \cdots & \eta_{1n}^0 \\ \eta_{21}^0 & \eta_{22}^0 & \cdots & \vdots \\ \vdots & \vdots & \ddots & \vdots \\ \eta_{k1}^0 & \cdots & \cdots & \eta_{kn}^0 \end{bmatrix} \begin{bmatrix} E_{11}^n & E_{12}^n & \cdots & E_{1k}^n \\ E_{21}^n & E_{22}^n & \cdots & E_{2k}^n \\ \vdots & \vdots & \ddots & \vdots \\ E_{k1}^n & \cdots & \cdots & E_{kn}^n \end{bmatrix}$$

Measuring the power input in each subsystem and the average kinetic energies and inverting the equation, all the damping factors η can be computed. The power input can be indirectly computed measuring the force $f(t)$ and vibration velocity $v(t)$ at the same excitation point. In the frequency domain, it can be proved that the power input can be calculated using the measured single sided cross-spectrum of the force and acceleration at the excitation point, denoted as S_{af}.

$$P_{in} = \frac{1}{T}\int_0^T f(t)\,v(t)\,dt \quad \xrightarrow{\text{Frequency domain}} \quad P_{in} = \frac{1}{\omega}\,\mathrm{Im}\int_{\omega_1}^{\omega_2} S_{af}(\omega)\,d\omega$$

The average kinetic energy can be computed from the measured vibration velocity as following, where M denotes the mass of the subsystem, N the number of response measurements and *i the i-th* measurement. In the frequency domain, it can be proved that the average vibration energy can be calculated using the measured single sided auto-spectrum of the acceleration at the *i-th* point $S_{i,aa}$.

$$\langle \overline{E} \rangle \cong \frac{M}{N}\frac{1}{T}\sum_{i=1}^{N}\int_0^T v_i^2(t)\,dt \quad \xrightarrow{\text{Frequency domain}} \quad E = \frac{M}{N}\frac{1}{\omega^2}\sum_{i=1}^{N}\int_{\omega_1}^{\omega_2} S_{i,aa}(\omega)\,d\omega$$

Another aspect of interest in the context of structure-borne noise is the characterization of a viscoelastic isolator. When the structural designer has to choose the appropriate isolator for a specific application, information on its stiffness and damping are mandatory. This information is collected in the temperature-frequency nomograms shown on Figure 88. The nomogram is obtained performing dynamic tests at different frequencies and temperatures, known as *Dynamic Mechanical Analysis (DMA)*. DMA consists of an experimental procedure in which a sinusoidal controlled stress is applied to the specimen and deformation is measured (or vice-versa). Knowing the stress and the strain, Equation 28 can be used for computing the complex tensile and shear moduli of the material. The tests are performed at different frequencies and temperatures [36]. It can be noticed that both storage modulus (red curve) as well loss modulus (blue curve) increase with increasing frequency and decreasing temperatures. The tangent of the phase, i.e. the damping of the material (green curve in the figure) increases with frequency and with temperature up to a certain temperature, after which it starts to decrease.

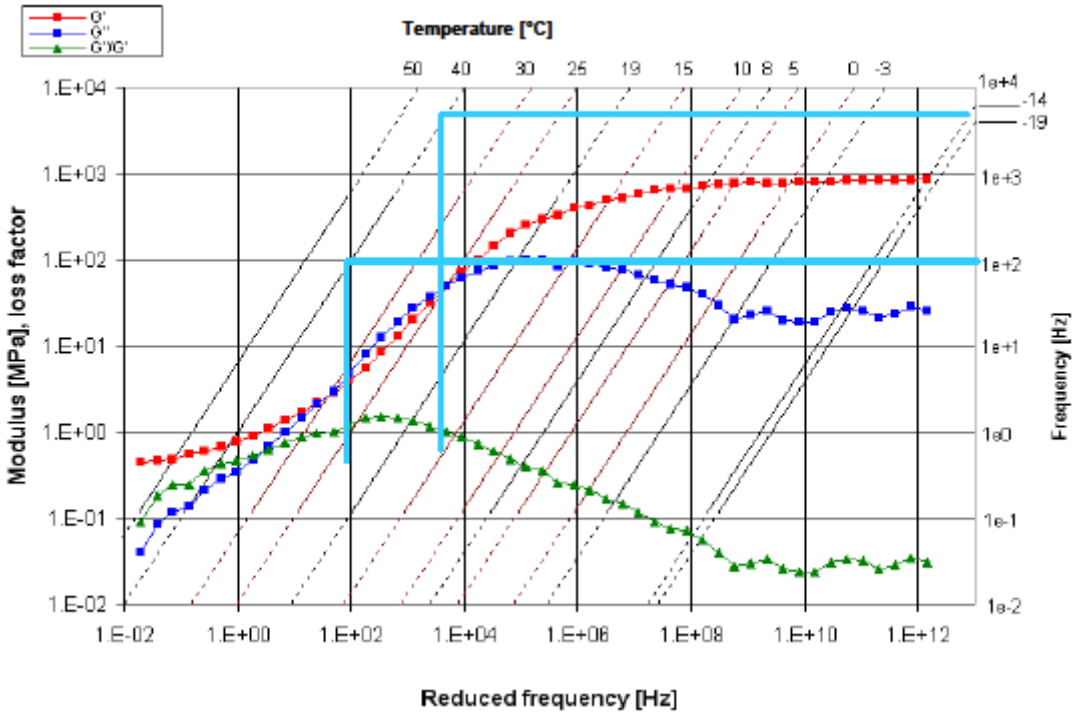

Figure 88 - Temperature-frequency nomogram for a viscoelastic material [37]

Figure 89 shows an example of a simple experimental setup used to measure the dynamic stiffness of a viscoelastic isolator [38]. A flexible stinger is placed between the shaker (not visible in the figure) and the load cell to avoid the transmission of non-longitudinal forces. The sample is connected to two steel disks for stability reasons. The disks can be considered rigid and the force perfectly transmitted to the sample. Below the sample, i.e. between the sample and the ground, an accelerometer is placed. From the acquired accelerations, displacements are calculated. Knowing the applied force from the load cell measurement and the displacements, dynamic stiffness can be computed.

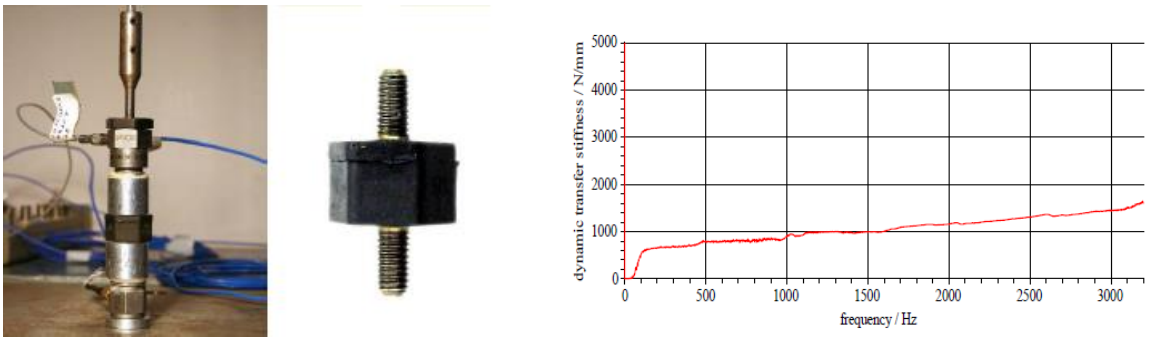

Figure 89 - Experimental setup for dynamic stiffness measurement of viscoelastic isolator [35]

Dynamic stiffness of a viscoelastic material is also influenced by prestress. A prestress increases the tensile storage modulus (the tensile stiffness) due to the increasing cross-section area after pre-deformation [36]. Figure 90 shows measurements of the storage modulus E' of a rubber damper for different frequencies and pre-stress.

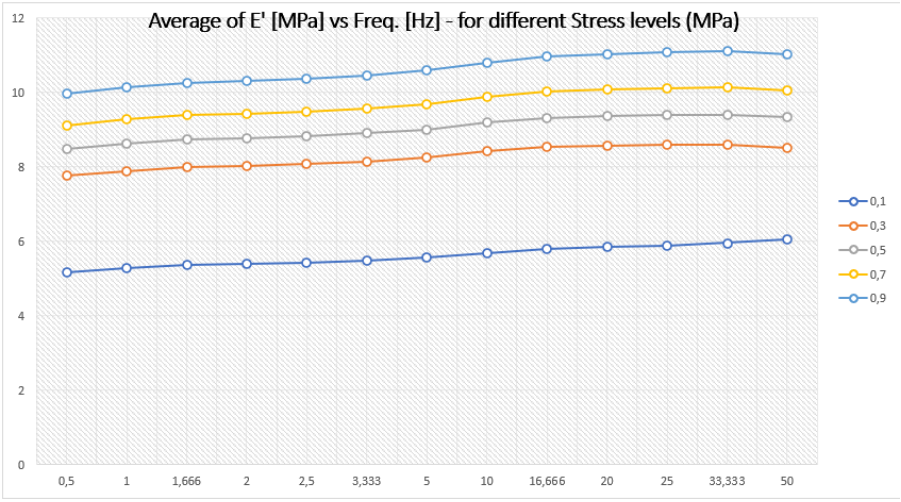

Figure 90 - Average storage modulus vs frequency for different prestress levels of a rubber damper

Figure 91 shows an example of experimental setup used to measure the damping coefficient of an elastomer [37]. A known mass is glued on the sample. The system represents a mass-damper-spring system where damper and spring are connected in parallel. An accelerometer has been positioned on the mass and the system has been hit by means of a hammer excitation. The free response has been measured and from it the damping ratio is extrapolated using logarithmic decrement analytical formulas. Finally, the viscous damping coefficient has been calculated from the well-known Equation 30, where *m* is the mass, ξ is the damping ratio and ω_n is the natural frequency of the system, which is known once the static stiffness of the viscoelastic sample is measured through a simple static compressive test.

$$c = 2m\xi\omega_n \qquad (30)$$

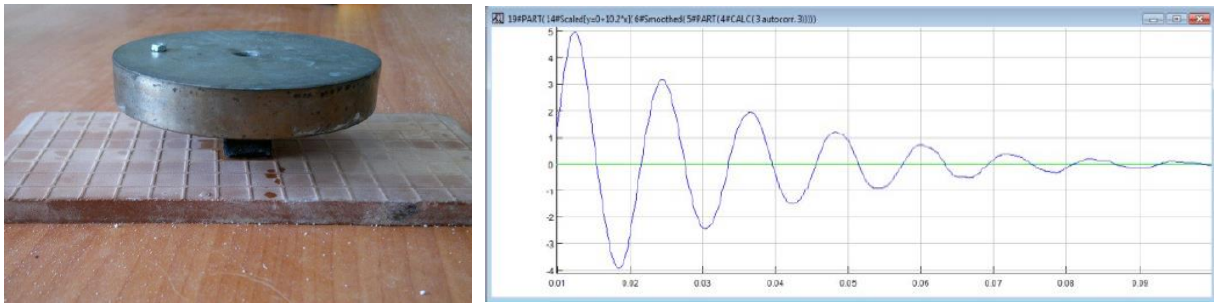

Figure 91 - Experimental setup for damping ratio measurement [37]

7.3 Numerical methods

Two different numerical methods can be used in the context of structure-borne noise. The first one is SEA, based on Statistical Energy Analysis formulation already presented. In this case, the different structural subsystems are modeled using simple models like beams or shells whose shape functions can support bending, longitudinal and shear waves deformations. The different subsystems are connected by joints to which coupling loss factors are assigned based on experience or experimental SEA. This method is best suited for high-frequency problems, in which exploited wavelengths are considerably small compared to the subsystems dimension and each subsystem contains several modes in the analyzed frequency band. In fact, this permits to capture these modes without using an excessive number of degrees of freedom as in the case of a 3D FEM model.

The second applicable numerical method is FEM. Using FEM, a more detailed model of the structure can be achieved and damping properties can be assigned to all the materials based on experience or damping coefficient measurements. In Ansys, for example, damping ratio or structural damping can be assigned. Although FEM provides higher accuracy and gives the possibility to take into account non-linear effects like large deformations in viscoelastic materials, it needs many more degrees of freedom. For high-frequency problems in which large and complex structures are analyzed, FEM inevitably leads to increasing model size due to the finer mesh needed for capturing small wavelengths. For this reason, FEM is best suited for low frequency problems. Figure 92 shows a comparison between the FEM and SEA model of a beam-tractor frame connection [38].

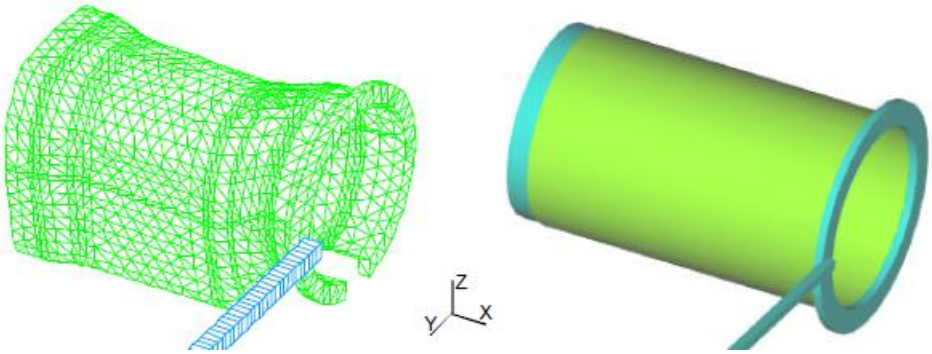

Figure 92 - FEM (left) and SEA (right) models of a beam connected to a tractor frame [38]

A simplified way of modeling isolators in a FE model is that of using spring elements to which stiffness and viscous damping (linear or non-linear) are assigned after having measured them using the procedures described above. This is an efficient modeling solution in cases where local solutions on the elastic isolator are not of interest and only the response of the structure is needed. Figure 93 shows an example in which rubber mounts have been modeled using spring elements whose stiffness has been measured through a static compression test and viscous damping [Ns/m] has been calculated using damping ratio extrapolated from logarithmic decrement of the free response, as shown in Figure 91 [37].

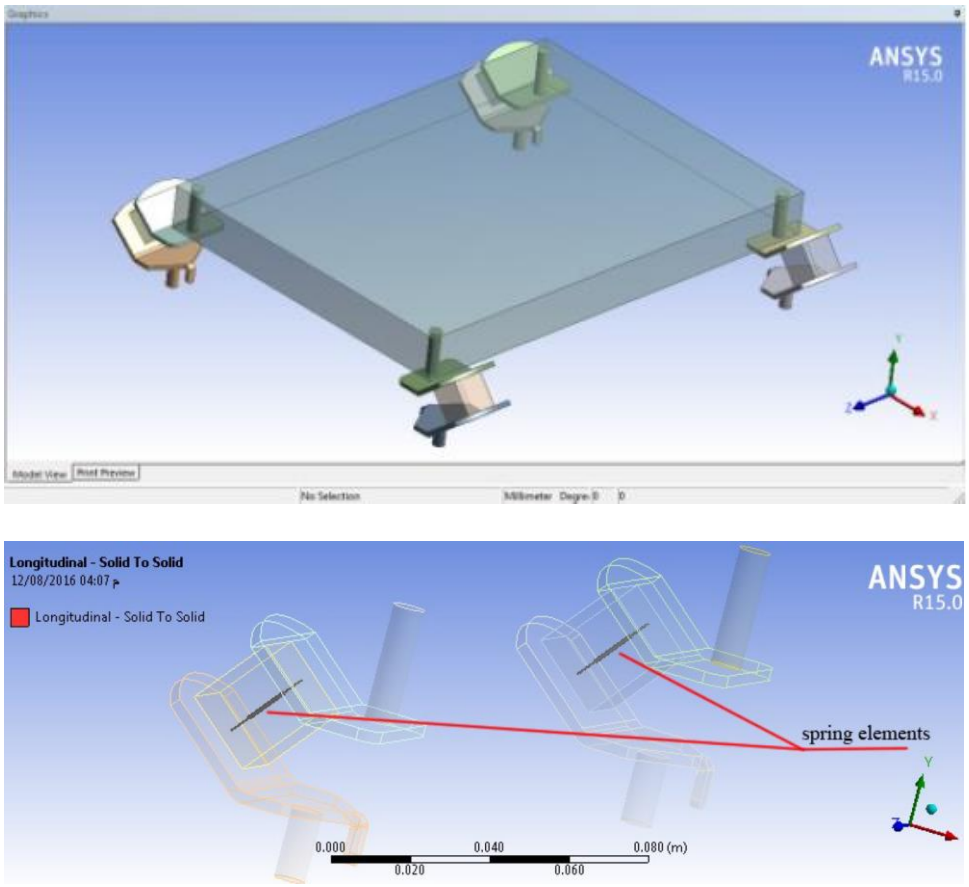

Figure 93 - Rubber mounts modeling through spring elements [37]

8. Conclusions and future works

The present work proposes a methodology for computing acoustic emissions of a dry-type transformer based on a Multi-physics Finite Element procedure. The proposed workflow demonstrates the capability of such procedure of obtaining all the interesting acoustic quantities which can be also measured by experimental tests. Also, the development of this methodology gave the possibility to study other interesting topics, such as the effect of core saturation, the influence of the explicit modelling of core laminations, the effect of clamping pressure on the interaction between the frame and the core and the development of a homogenization technique for simplifying the winding modeling.

The methodology has been simplified as much as possible and specific assumptions have been adopted to be able to judge the results. Since the methodology is the starting point of a roadmap which will take to the redaction of a technical standard to be used for future transformers designs, it is extremely important to have the certainty that all the models are behaving as expected. For this reason, starting from the simplest modeling as possible is a must.

Further developments will aim to the relaxation of the strongest assumptions, such as material isotropies, neglection of DC force component or the limitation to the ambient temperature. Also, others different transformers designs will be object of study, giving the possibility to investigate, for example, step-lap joints, which have been not analyzed in this work.

A prototype of the modeled traction reactor, TRASFOR design XA3823B, has been recently manufactured for purpose of validation. Experimental measurements of magnetostriction on the core steel will be performed in a dedicated laboratory of Hitachi Energy. Acoustic experimental tests will be performed in the following months in anechoic chamber, to validate the whole procedure. Two acoustic tests will be performed: one with the winding only, to characterize the load noise, and one with the whole reactor assembled, from which the total sound power will be measured.

The next step will be that of creating a FE automation (Shell) based on the proposed methodology. After having built an automation, different transformers could be analyzed in a quick and user-friendly way, speeding up the design process. Multiple sensitivity analyses will be performed to understand how different parameters affect noise emissions and design rules will be derived. Finally, the first version of a technical standard containing modeling guidelines and design rules for dry-type transformers will be delivered. A schematic of the roadmap is shown on Figure 94.

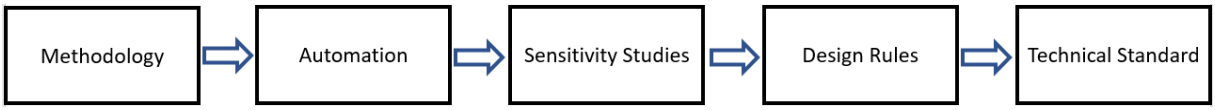

Figure 94 - Roadmap to the vibroacoustics technical standard

After the completion of the first version of a technical standard, the methodology will be improved for analyzing oil-type transformers as well. This will give the possibility of understanding the mechanisms involved in the tank vibration, such as the transmission of the loads through the oil and the magnetic forces acting on the tank. After this, the final version of a technical standard will be delivered to the engineering. The whole roadmap is expected to last at least 3 years.

9. Appendix

9.1 Beam model for homogenized winding equivalent material derivation

A more comprehensive presentation of the beam model used to derive the Young's modulus assigned to the homogenized winding is here reported. The results of two different models used for checking the method are presented and a comparison between the real and homogenized winding is shown. The two models represent a circular and a rectangular winding respectively.

9.1.1 Circular winding

In the first example, a circular winding is considered. The first step is that of modeling a beam with the same cross section of the real winding turns, representing all the materials with a non-negligible stiffness, as shown on Figure 95. This is the reference model. In this example, the winding turns are made of a central aluminum conductor surrounded by resin, whose properties are reported in Table 9. The length of the beam is chosen equal to 10 times the longer dimension of the cross section to respect the assumptions of the Euler-Bernoulli beam.

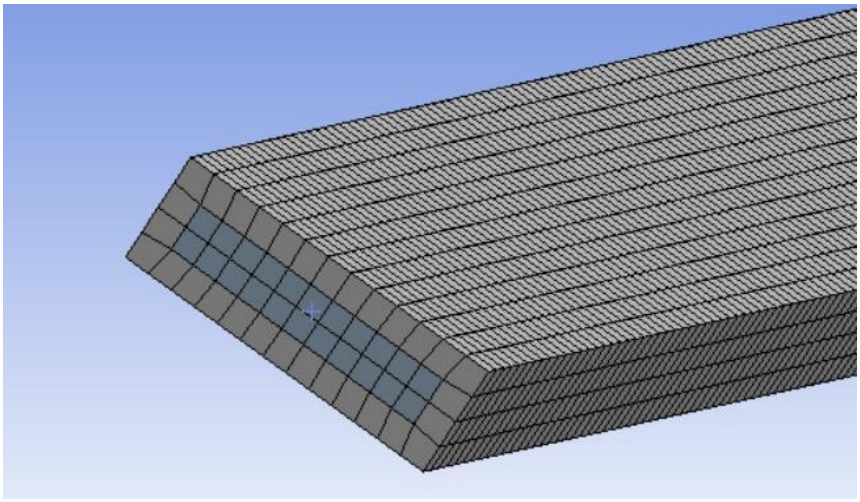

Figure 95 – Reference beam mesh

Table 9 - Properties of materials composing the winding

	$E\ [MPa]$	ν	$\rho\ \left[\frac{Kg}{m^3}\right]$
Aluminum	70000	0.31	2700
Resin	7600	0.35	1304

A conformal mesh is used, assuming that all the materials are perfectly bonded together. A free-free modal analysis is run and the eigenfrequency of the first axial eigenmode is extracted, as shown on Figure 96, in this case equal to *8603.3 Hz*. This frequency is substituted in Equation 15, where $i = 1$ and ρ is calculated with Equation 17, and E is calculated. Geometric parameters in the equations are set equal to the external dimensions of the winding turns, i.e. equal to the homogenized ones. The following material properties are calculated:

- $\rho = 1809 \frac{Kg}{m^3}$
- $E = 30169\ MPa$
- $\nu = 0.3$ (can be chosen arbitrarily)

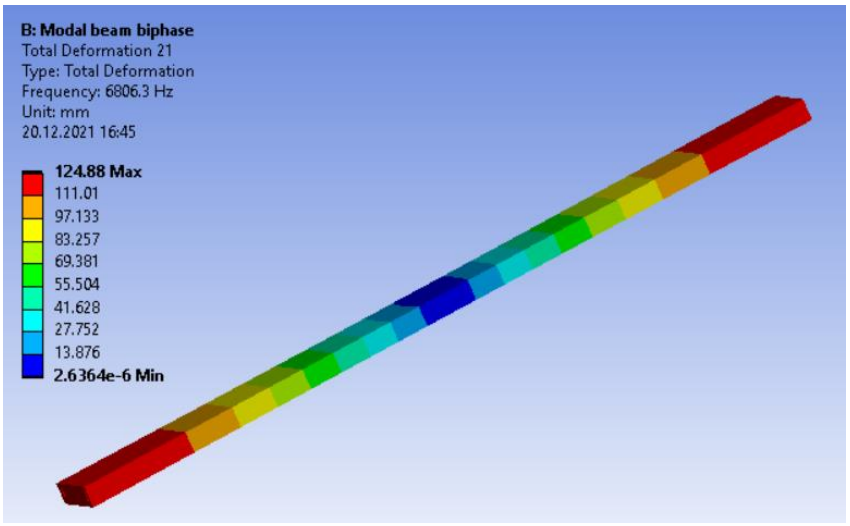

Figure 96 – 1st beam axial mode resulting from modal analysis (right)

A homogenized beam is modeled with the same cross section of the homogenized winding turns, i.e. with the external dimensions of the winding turns. A homogeneous, isotropic material with the properties calculated before is assigned. The mesh size on Figure 97 shows the big advantage of homogenization.

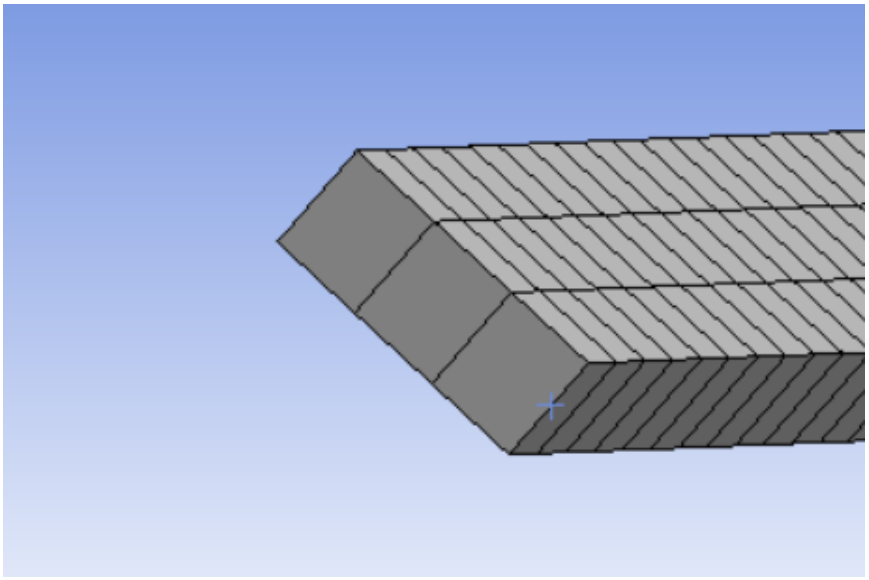

Figure 97 – Homogenized beam mesh

Computing eigenfrequencies through a modal analysis, it can be seen that the eigenfrequency of the first axial mode has a negligible difference with respect to the one of the reference model. Differently, the eigenfrequencies of the first bending mode are not in accordance, as shown in Table 10. The reason why only the first eigenfrequencies are considered is that fitting the first eigenfrequencies of a mode in a specific direction using a beam model, automatically leads to fitting higher eigenfrequencies of the modes in the same direction. Fitting the first eigenfrequencies only is sufficient.

Table 10 - Comparison of eigenfrequencies between reference and homogenized beam

	Reference Beam	Homogenized Beam	Error
First Axial Eigenfrequency [Hz]	6806.3	6801.6	0.07 %
First Bending Eigenfrequency [Hz]	259.2	409.5	58 %

The material properties computed are now assigned to the homogenized winding. An analysis has been run on the winding model, comparing the real and homogenized winding. In the first instance, two single turns (real and homogenized) are compared in terms of eigenfrequencies. The difference in the eigenfrequencies of the breathing mode is negligible, as shown in Figure 98.

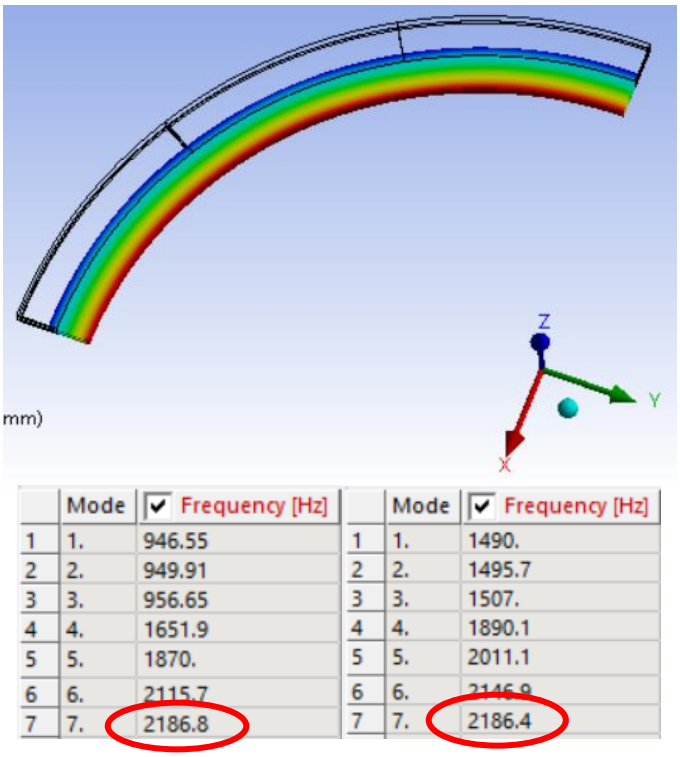

	Mode	Frequency [Hz]		Mode	Frequency [Hz]
1	1.	946.55	1	1.	1490.
2	2.	949.91	2	2.	1495.7
3	3.	956.65	3	3.	1507.
4	4.	1651.9	4	4.	1890.1
5	5.	1870.	5	5.	2011.1
6	6.	2115.7	6	6.	2146.9
7	7.	2186.8	7	7.	2186.4

Figure 98 - Breathing mode. Mode 7 at 2186.8 Hz. Eigenfrequencies reference vs homogenized.

This is a proof that a turn acts like a beam. Fitting the axial eigenfrequencies in the beam model leads to fitting the eigenfrequencies of the breathing mode of a circular turn, which involves the axial stiffness of the turn (where “axial stiffness of the turn” is here intended as circumferential, as shown on Figure 99). The modes in other directions are not well fit, which is the limitation of this technique. However, the radial dynamics is the most important. In fact, one of the most used techniques in Hitachi Energy for measuring the sound power, is that of deriving it from radial measurements of sound pressure levels, according to standards [1]. Measurements above the transformer are usually avoided due to safety reasons.

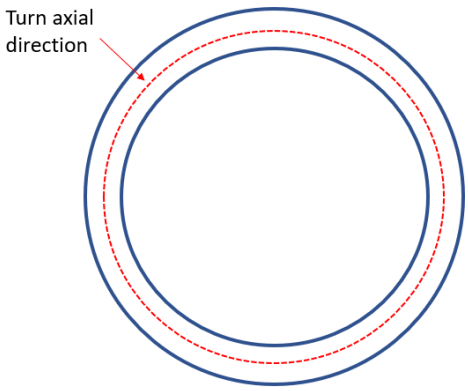

Figure 99 - Turn axial direction. Top/bottom view

At this point, the analysis is performed on the complete winding. Electromagnetic forces have been computed in Maxwell and then interpolated in the structural model, as shown on Figure 100.

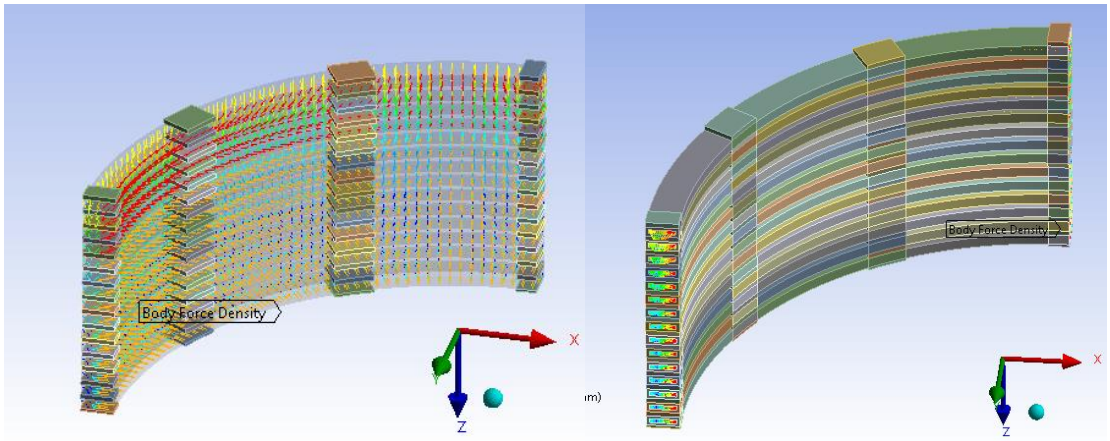

Figure 100 - Homogenized winding (left) vs real winding (right)

A harmonic analysis is performed. The deformed shape of the winding is shown on Figure 101. The average radial velocity of the two windings (reference and homogenized) during the operative deformation (breathing mode) are similar, as shown in Table 11. This is a proof that the radial deformation of the winding during the operative deformation involves a stretching-contraction of the winding turns, dominated by the turn axial stiffness, which has been fit using the beam model.

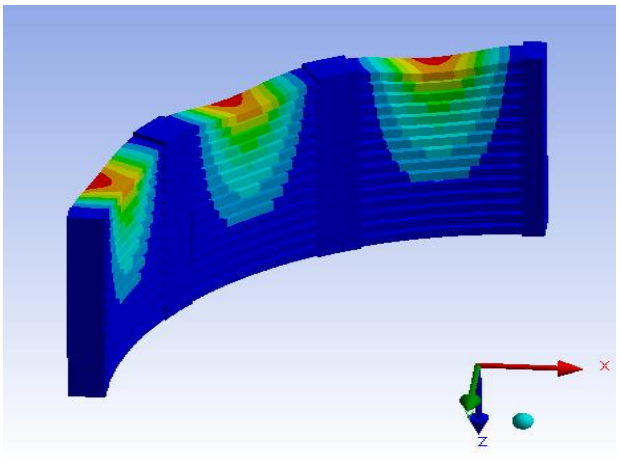

Figure 101 - Deformed shape of the winding subjected to Lorentz forces

The same is valid for SPL calculated on a microphone placed *5 m* far from the winding axial mid-point in the radial direction, as shown on Figure 102. The difference is less than *2 dB*. On the other hand, computing the SPL at 5 m above the winding (on its axis), the error is consistent. This also leads to a consistent error in the Sound Power computation. Table 11 resumes the results obtained from the reference and homogenized winding for *400, 600 and 800 Hz*.

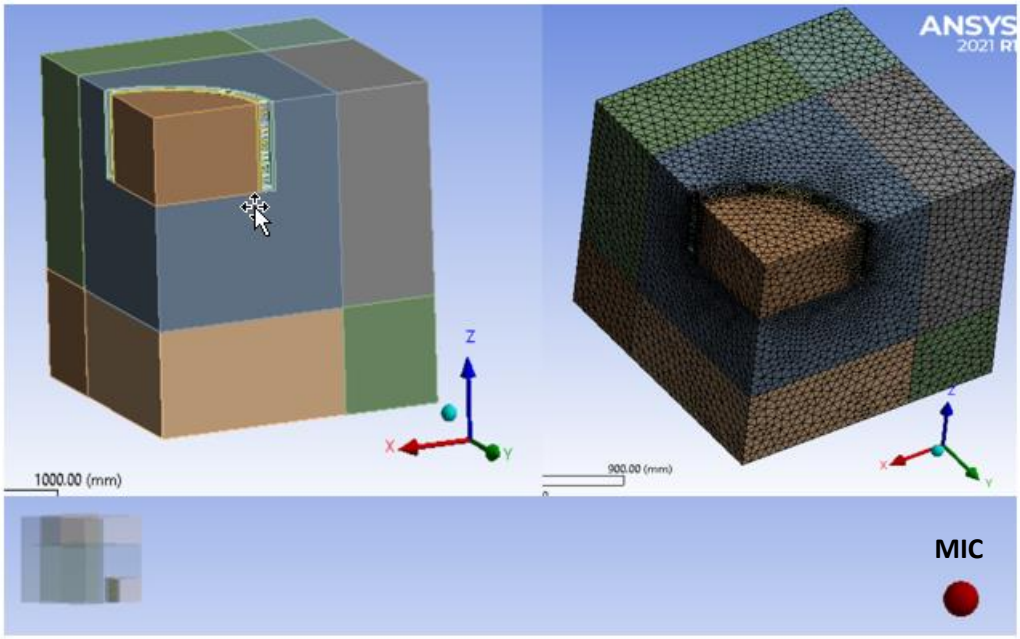

Figure 102 - Acoustic model and microphone position from SPL computation

Table 11 - Comparison between reference and homogenized winding

	Reference	Homogenized	Error	Frequency [Hz]
Average radial velocity [mm/s]	0.065 0.104 0.154	0.062 0.098 0.143	5% 6% 7%	400 600 800
Average vertical velocity [mm/s]	0.105 0.180 0.300	0.235 0.371 0.535	223% 200% 178%	400 600 800
Radial SPL [dB]	25.836 27.432 34.5	25.553 27.236 33.304	0.3 dB 0.2 dB 1.2 dB	400 600 800
Vertical SPL [dB]	22.663 41.11 50.41	21.364 33.331 43.13	1.3 dB 8 dB 7 dB	400 600 800
Sound Power [dB]	50.934 57.559 63.838	50.572 55.225 59.527	0.4 dB 2.3 dB 4.3 dB	400 600 800

9.1.2 Rectangular winding

In the second example, a rectangular winding is considered, as shown on Figure 105, where a quarter of the geometry is reported. As for the previous example, the first step is that of modeling a beam with the same cross section of the real one, representing all the materials with a non-negligible stiffness, as shown on Figure 103. This is the reference model. In this example, the winding turns are made of a central aluminum conductor surrounded by resin, whose properties are reported in Table 12. The length of the beam is chosen 10 times the longer dimension of the cross section, to respect the assumptions of the Euler-Bernoulli beam.

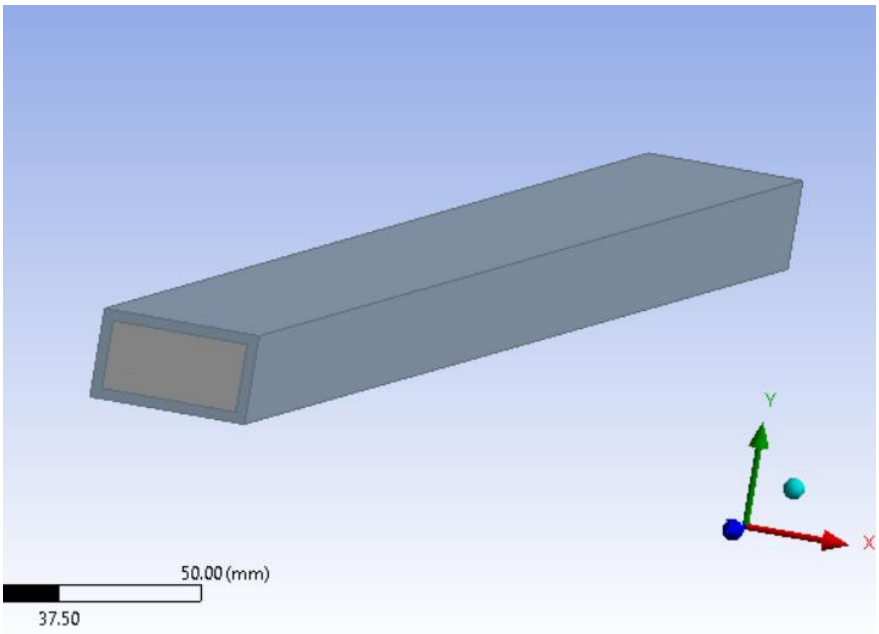

Figure 103 - Biphase beam - Y direction corresponds to the radial direction of the winding

Table 12 - Properties of materials composing the winding

	$\boldsymbol{E}\ [\boldsymbol{MPa}]$	$\boldsymbol{\nu}$	$\boldsymbol{\rho}\ \left[\frac{\boldsymbol{Kg}}{\boldsymbol{m^3}}\right]$
Aluminum	70000	0.31	2700
Resin	7600	0.35	1304

A conformal mesh is used, assuming that all the materials are perfectly bonded together. A modal analysis is run and the eigenfrequency of the first bending eigenmode in the direction correspondent to the radial direction of the winding is extracted, as shown on Figure 104. This frequency is substituted in Equation 16, where $i = 1$ and ρ is calculated with Equation 17, and E is calculated. Geometric parameters in the equations are set equal to the external one, i.e. equal to those of the homogenized one. The following equivalent material properties are calculated:

- $\rho = 2230\,\frac{Kg}{m^3}$
- $E = 31742\ MPa$
- $\nu = 0.3$ (can be chosen arbitrarily)

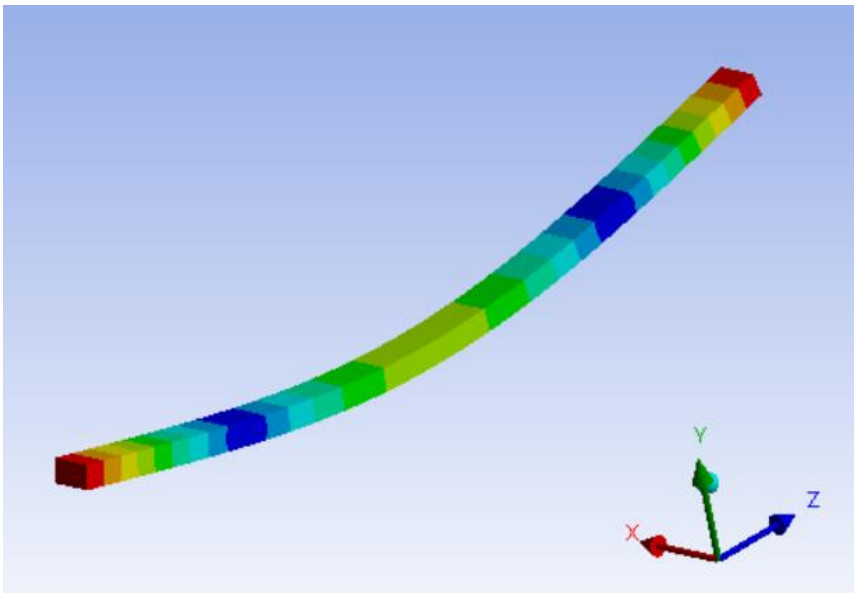

Figure 104 - First bending mode in winding radial direction

At this point, the analysis is performed on the complete winding. Electromagnetic forces have been computed in Maxwell and then interpolated in the structural model. A harmonic analysis is performed on the winding model, comparing the real and homogenized winding, shown on Figure 105. The average radial velocity of the two windings (reference and homogenized) during the operative deformation (breathing mode) are similar. This means that the radial deformation of a rectangular winding during the operative deformation involves a bending of the winding, dominated by the radial bending stiffness of the turns, which has been fitted using the beam model. Same is valid for SPL calculated on a microphone placed *5 m* far from the winding axial mid-point in the radial direction and for Sound Power. The error is below *0.4 dB* in the range of frequency considered. On the other hand, computing the SPL at *5 m* above the winding (on its axis), the error is consistent. Table 13 shows the results obtained from the two compared models at *120, 140* and *160* Hz. Negative *dB* are obtained when noise is negligibly low and affected by numerical errors.

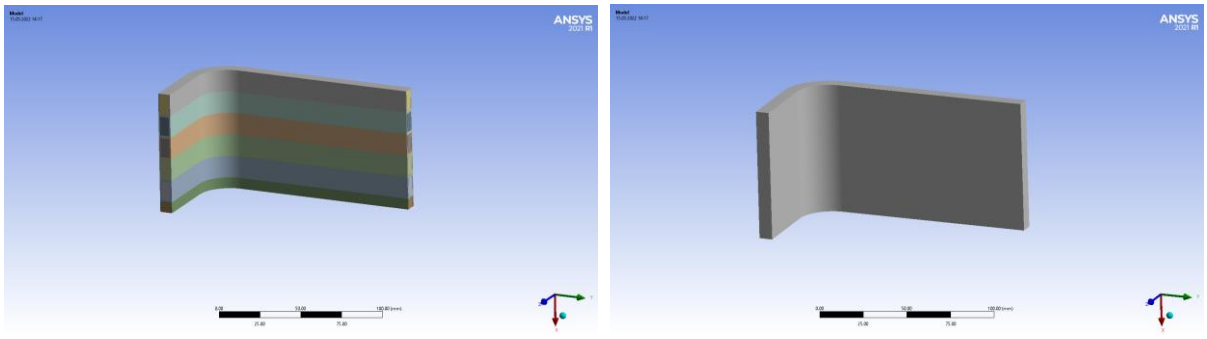

Figure 105 – Biphase vs homogenized windings

Table 13 - Comparison between reference and homogenized winding

	Reference	Homogenized	Error	Frequency [Hz]
Average velocity Z [mm/s]	2.7811 3.5242 4.4725	2.7459 3.4795 4.4157	1.5% 1.5% 1.4%	120 140 160
Average velocity Y [mm/s]	0.40699 0.52134 0.66988	0.42806 0.54872 0.70564	4.7% 3.7% 4.3%	120 140 160
Average velocity X [mm/s]	2.9204e-003 3.4357e-003 3.9717e-003	3.4259e-003 4.0354e-003 4.6727e-003	15% 15% 15%	120 140 160
SPL radial direction [dB]	15.383 21.974 28.302	15.604 22.171 28.488	0.3 dB 0.2 dB 0.2 dB	120 140 160
SPL vertical direction [dB]	-27.169 -14.081 -2.0696	-9.6719 0.87605 11.278	17.5 dB 14 dB 9 dB	120 140 160
Sound Power Level [dB]	34.304 40.9 46.507	34.526 41.102 46.701	0.2 dB 0.2 dB 0.2 dB	120 140 160

9.2 Model for the determination of structural interactions due to clamping

A brief description of the model used to have better understanding of the interaction of all the structural part after having clamped the core is here presented. Figure 107 shows the model used for this analysis, which is the same model used to test the methodology already presented. The real sequence of clamping is simulated. Clamping forces are calculated from clamping torques available from drafts through VDI [31]. They are applied through the *Bolt precompression* tool available in Ansys. Figure 106 shows a table from VDI in which the underlined values are the torques and forces relative to the studied case.

Anhang A Tabellen zur Berechnung

Tabelle A1. Montagevorspannkräfte $F_{M\,Tab}$ und Anziehdrehmomente M_A bei ν = 0,9 für **Schaftschrauben** mit metrischem Regelgewinde nach DIN ISO 262; Kopfabmessungen von Sechskantschrauben nach DIN EN ISO 4014 bis 4018, Schrauben mit Außensechsrund nach DIN 34800 bzw. Zylinderschrauben nach DIN EN ISO 4762 und Bohrung „mittel" nach DIN EN 20273

Annex A Calculation tables

Table A1. Assembly preload $F_{M\,Tab}$ and tightening torque M_A with ν = 0,9 for **shank bolts** with metric standard thread according to DIN ISO 262; head dimensions of hexagonal bolts according to DIN EN ISO 4014 to 4018, hexalobular external driving head bolts according to DIN 34800 or cylindrical bolts according to DIN EN ISO 4762 and hole "medium" according to DIN EN 20273

Abm. Size	Fest.-Klasse Strength Grade	Montagevorspannkräfte/Assembly preload $F_{M\,Tab}$ in kN für μ_G =							Anziehdrehmomente/Tightening torque M_A in Nm für $\mu_K = \mu_G$ =						
		0,08	0,10	0,12	0,14	0,16	0,20	0,24	0,08	0,10	0,12	0,14	0,16	0,20	0,24
M4	8.8	4,6	4,5	4,4	4,3	4,2	3,9	3,7	2,3	2,6	3,0	3,3	3,6	4,1	4,5
	10.9	6,8	6,7	6,5	6,3	6,1	5,7	5,4	3,3	3,9	4,6	4,8	5,3	6,0	6,6
	12.9	8,0	7,8	7,6	7,4	7,1	6,7	6,3	3,9	4,5	5,1	5,6	6,2	7,0	7,8
M5	8.8	7,6	7,4	7,2	7,0	6,8	6,4	6,0	4,4	5,2	5,9	6,5	7,1	8,1	9,0
	10.9	11,1	10,8	10,6	10,3	10,0	9,4	8,8	6,5	7,6	8,6	9,5	10,4	11,9	13,2
	12.9	13,0	12,7	12,4	12,0	11,7	11,0	10,3	7,6	8,9	10,0	11,2	12,2	14,0	15,5
M6	8.8	10,7	10,4	10,2	9,9	9,6	9,0	8,4	7,7	9,0	10,1	11,3	12,3	14,1	15,6
	10.9	15,7	15,3	14,9	14,5	14,1	13,2	12,4	11,3	13,2	14,9	16,5	18,0	20,7	22,9
	12.9	18,4	17,9	17,5	17,0	16,5	15,5	14,5	13,2	15,4	17,4	19,3	21,1	24,2	26,8
M7	8.8	15,5	15,1	14,8	14,4	14,0	13,1	12,3	12,6	14,8	16,8	18,7	20,5	23,6	26,2
	10.9	22,7	22,5	21,7	21,1	20,5	19,3	18,1	18,5	21,7	24,7	27,5	30,1	34,7	38,5
	12.9	26,6	26,0	25,4	24,7	24,0	22,6	21,2	21,6	25,4	28,9	32,2	35,2	40,6	45,1
M8	8.8	19,5	19,1	18,6	18,1	17,6	16,5	15,5	18,5	21,6	24,6	27,3	29,8	34,3	38,0
	10.9	28,7	28,0	27,3	26,6	25,8	24,3	22,7	27,2	31,8	36,1	40,1	43,8	50,3	55,8
	12.9	33,6	32,8	32,0	31,1	30,2	28,4	26,6	31,8	37,2	42,2	46,9	51,2	58,9	65,3
M10	8.8	31,0	30,3	29,6	28,8	27,9	26,3	24,7	36	43	48	54	59	68	75
	10.9	45,6	44,5	43,4	42,2	41,0	38,6	36,2	53	63	71	79	87	100	110
	12.9	53,3	52,1	50,8	49,4	48,0	45,2	42,4	62	73	83	93	101	116	129
M12	8.8	45,2	44,1	43,0	41,9	40,7	38,3	35,9	63	73	84	93	102	117	130
	10.9	66,3	64,8	63,2	61,5	59,8	56,3	52,8	92	108	123	137	149	172	191
	12.9	77,6	75,9	74,0	72,0	70,0	65,8	61,8	108	126	144	160	175	201	223

Figure 106 - Table for torque-force link from VDI [31]

80 laminations are modeled and symmetries are exploited to increase computational efficiency. Real material properties, available from datasheets, are assigned to each part. Contacts between all the parts have been defined using the *Frictional* type and the *Normal Lagrange* formulation with a friction coefficient of *0.3.* This is the most general and accurate contact definition, where separation and sliding are allowed and the condition of non-penetration is explicitly expressed though an equation in the formulation, which leads to negligible penetrations. The drawback is slow convergence.

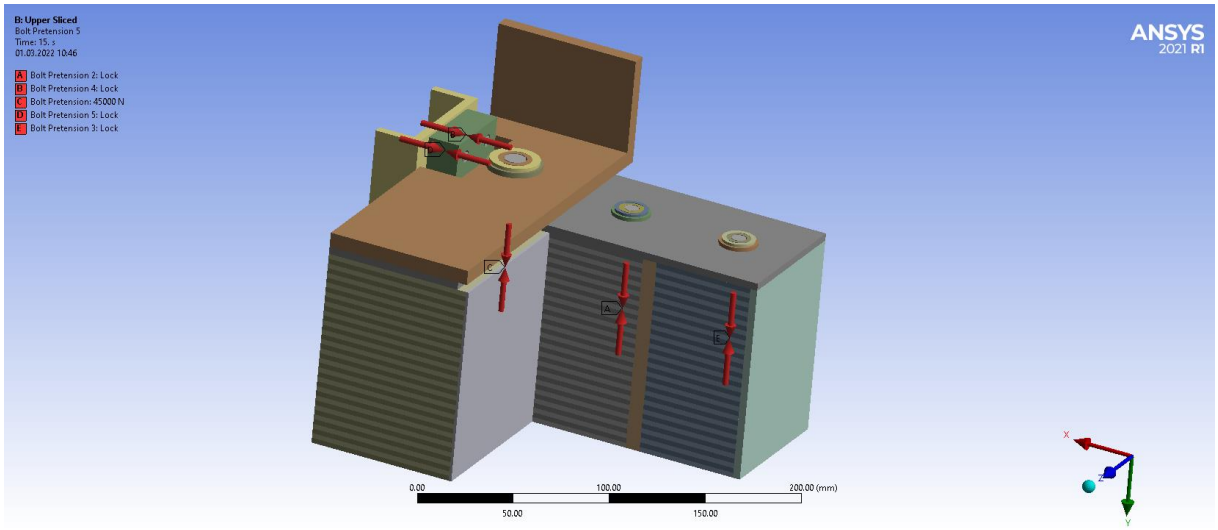

Figure 107 - Model for non-linear quasi static analysis for contact status prediction after clamping

Figure 108 shows the deformed structure after the clamping forces has reached their maximum nominal values. It is visible that some regions are separated. Penetration between the upper clamping profile and the block belonging to the vertical plate is occurring because no contact has been defined between them, since a small gap is present in the real case. For *1x* scaling of the contour, no penetration is visible. Figure 109 shows the final contact status. Dark orange regions indicate regions that are bonded, light orange ones indicate regions which are sliding respectively and yellow regions indicate a complete separation. It can be concluded that the regions close to the tie-rods can be considered as bonded together while in the central part of the yoke the bodies can slide respectively, which means that a *no separation* contact is more representative in this region, which has been used when performing the sensitivity analysis for studying the influence of the number of the lamination on the ERP in Paragraph 7.5.

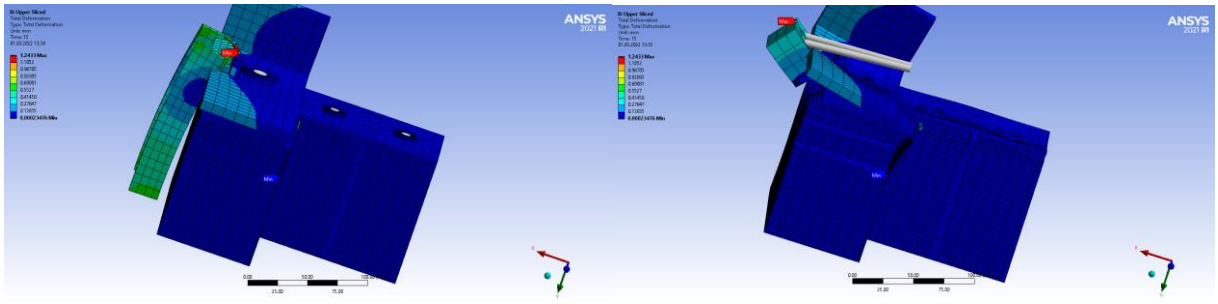

Figure 108 - Deformation due to the application of clamping forces. 30x scale (left) and 110x scale (right)

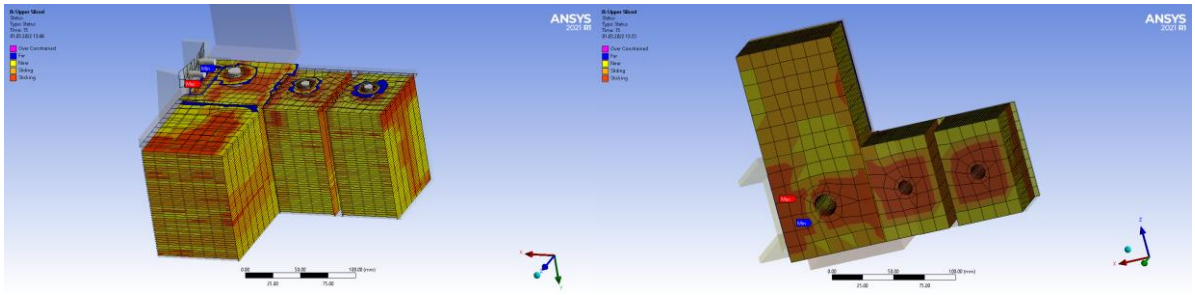

Figure 109 - Contact status after the application of clamping forces. Figure on the right refers to the inner part of the core (section plane used to plot the contour)

9.3 Monopole and Dipole models

Monopole and Dipole models represent a pulsating sphere immersed in a fluid which generate acoustic waves. Since analytical solutions are available for such models, they are useful to understand which are the best choices for constructing an acoustic model. They give guidelines to choose the correct acoustic domain shape and size, PML region size and number of PMLs layers, type of elements and mesh size. Sensitivity analyses have been performed to understand how these parameters affect the solution in terms of Sound Power. For briefness, only Dipole model is here presented, which is actually more stressing than Monopole model due to the high gradients of pressure generated. Figure 112 shows the acoustic pressure generated by a Dipole. The surface velocity is chosen equal to *1 m/s* in all the analyses. Acoustic domain size has been always chosen to be at least 10 times the radius of the sphere, to respect the hypotheses of the dipole model.

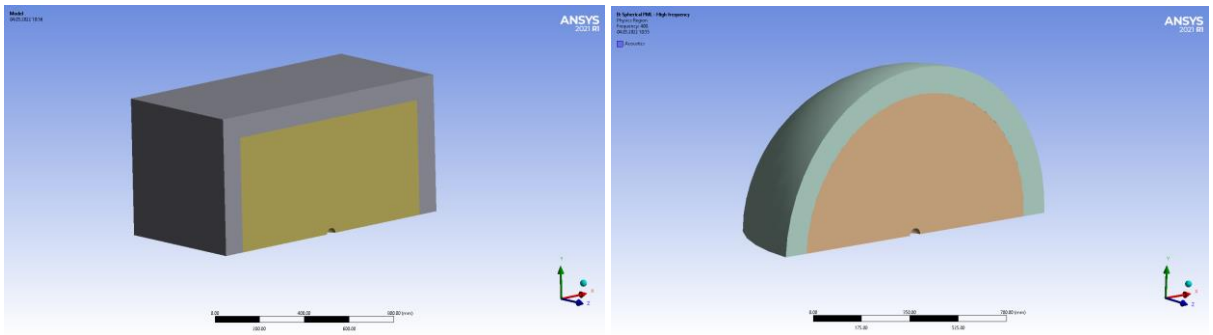

Figure 110 - Dipole model. Box shaped domain with cartesian PML (left) and spherical domain with irregular IPML (right)

9.3.1 Acoustic domain shape and acoustic domain size

The following paragraph shows sensitivity analyses where the influence of acoustic domain shape on the Sound Power is studied. A dipole radius of *25 mm* is here used. Two domain shapes are compared: spherical and box, as shown on Figure 110. The same minimum distance between radiating surface and PML inner surface is used. Quadratic tetrahedral elements have been used in both the models. PML elements are defined in two different ways for a spherical and a box shaped domain. When using a spherical domain, only *Irregular* type PMLs (IPML) can be used in Ansys. These elements allow to define reflection coefficient only in the direction normal to the inner surface of PML region. When using a box shaped domain, instead, only PML can be used. PML allow to define reflection coefficient in all the directions independently.

Box shaped acoustic domain has been proved to be the best choice, as also suggested by Ansys. A box shaped domain gives faster convergence and solution stability, as shown on Figure 111. This is due to the fact that PML are used and reflection coefficient can be defined in all the directions, which is not possible using a spherical domain with IPMLs.

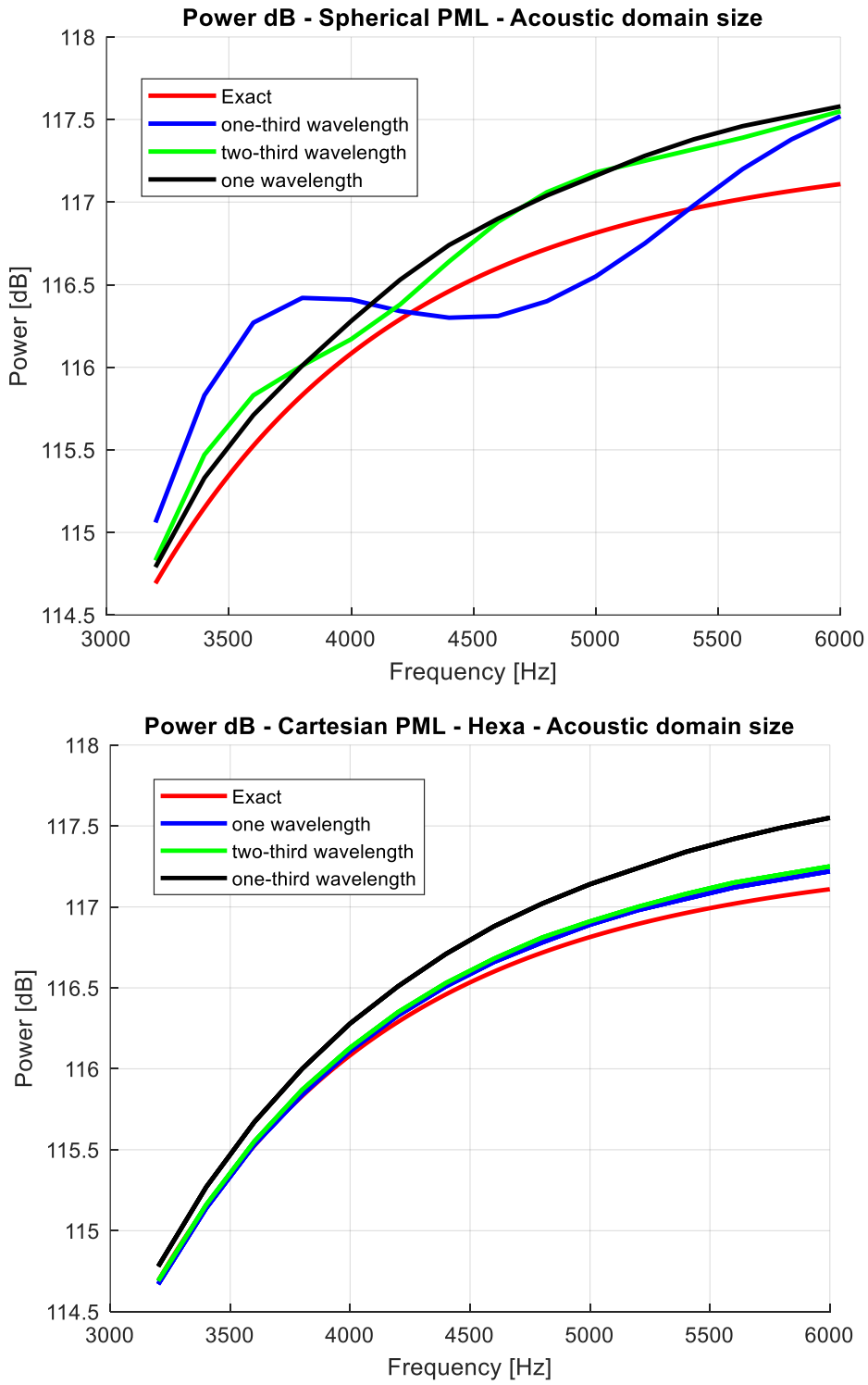

Figure 111 - Radiated Sound Power Level vs Frequency for different domain size compared to the analytical (exact) solution - Spherical domain (top) vs Box shaped domain (bottom)

Concerning the influence of acoustic domain size on the Sound Power, three different distances between the sphere and the inner surface of the PML region equal to one-third, two-third and one wavelength have been compared, where the reference wavelength here refers to a frequency of *6000 Hz,* i.e. the maximum simulated frequency. From Figure 111 it can be noticed that a domain size equal to two-third of wavelength is enough for convergence when using a box shaped domain. If a spherical domain is used, which is not however suggested, a domain size of at least one wavelength should be used. It can be also noticed that the deviation from the analytical solution increases with increasing

frequencies. This is due to the mesh size, which becomes less suitable when frequency increases (it should be refined for higher frequencies). However, a deviation of only *0.5 dB* is present at *6000 Hz*.

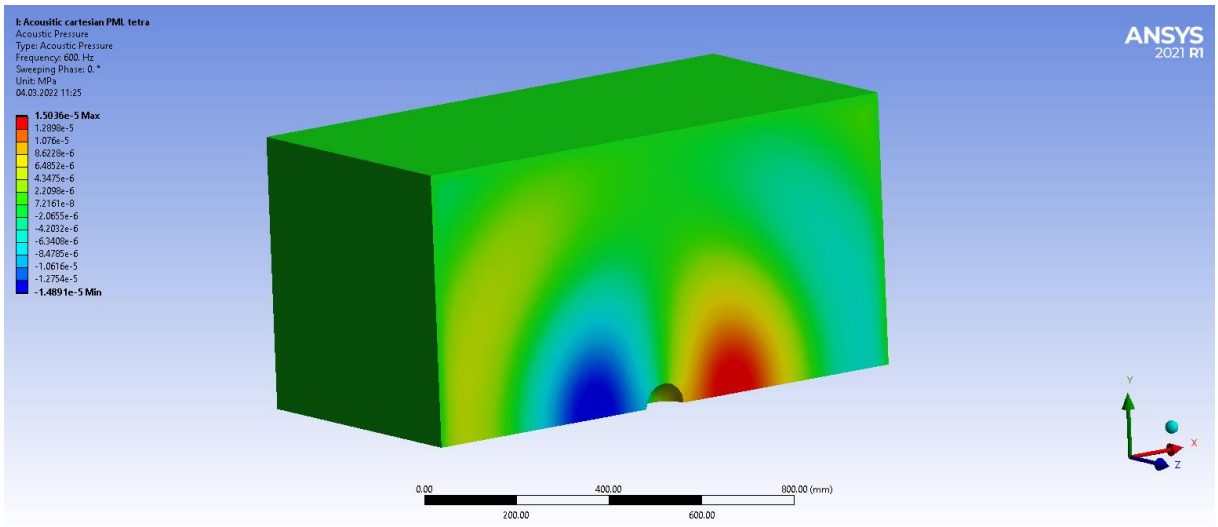

Figure 112 - Real part of acoustic pressure

9.3.2 PML region size and number of PML layers

The following paragraph shows sensitivity analyses where the influence of PML region size and number of PML layers on the acoustic power is studied, as shown on Figure 113. A dipole radius of *50 mm* is here used. A box shaped acoustic domain is used. All the parameters have been kept constant apart from PML region size and number of PML layers. 600 Hz frequency is simulated. Figure 114 shows that the PML region size should be chosen such that at least 2 layers of non-distorted PML elements whose size is equal to the size of the elements in the enclosure domain should be used. This is also suggested by Ansys.

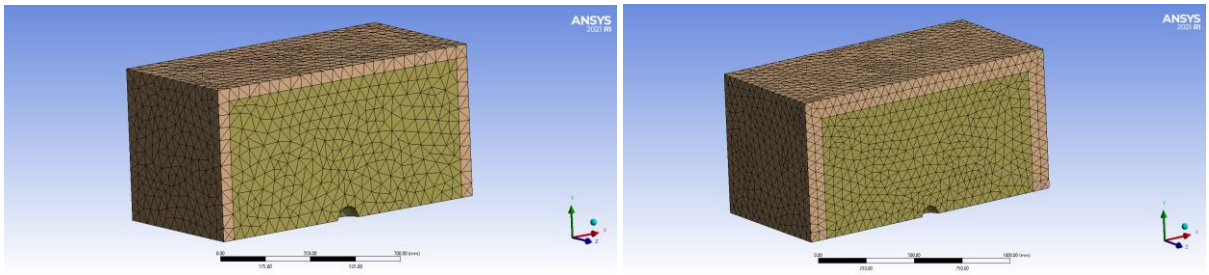

Figure 113 - 1 PML layer (left) and 2 PML layers (right)

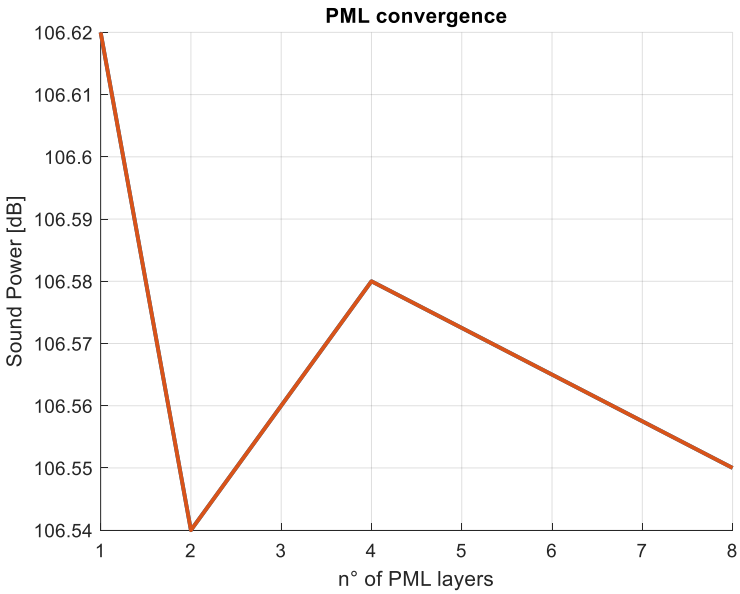

Figure 114 - Solution convergence with respect to the number of PML layers

9.3.3 Type of elements

The following paragraph shows sensitivity analyses where the influence of element type on the acoustic power is studied. A dipole radius of *50 mm* is here used. Quadratic tetrahedrons and quadratic hexahedral have been compared, as shown on Figure 115. Other parameters have been kept constant. Figure 116 shows that the difference between tetrahedrons and hexahedral is negligible. Since meshing the acoustic domain with hexahedral elements when dealing with acoustic analyses of real transformers can be difficult or can lead to highly distorted mesh, tetrahedrons have been proved to be the best choice.

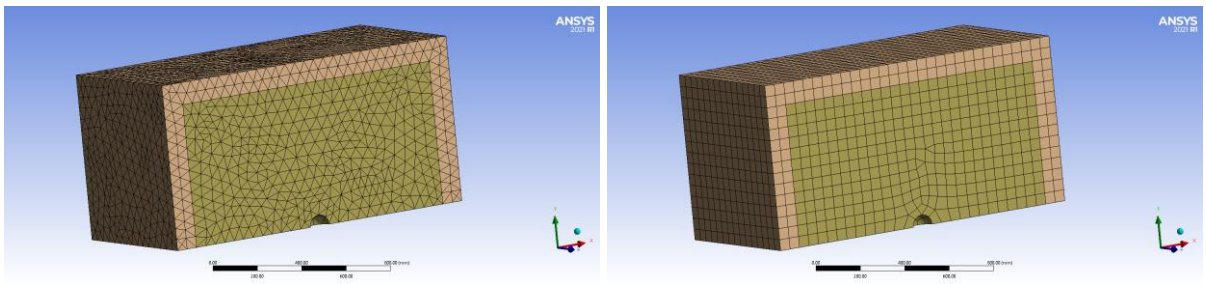

Figure 115 - Hexahedral mesh (left) vs tetrahedral mesh (right)

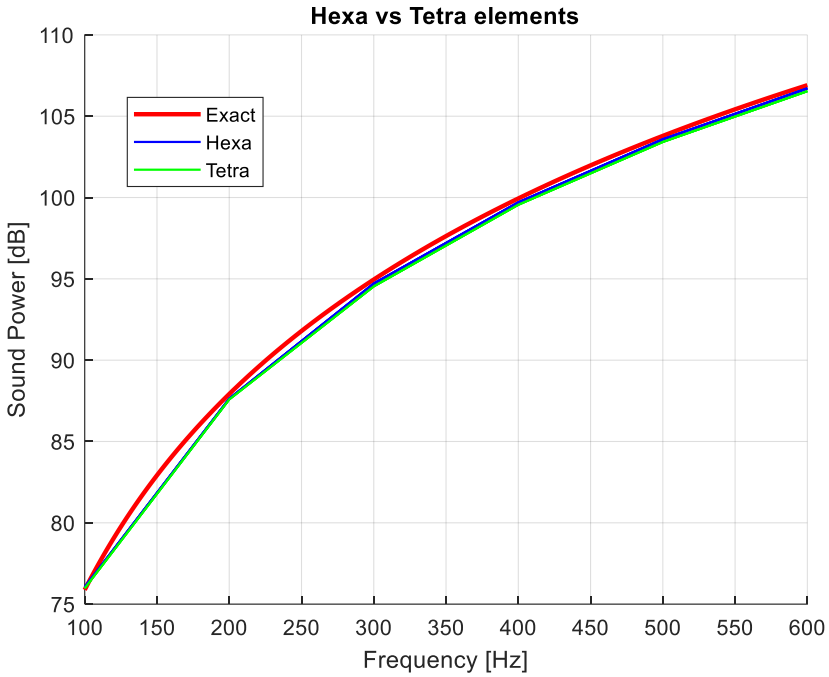

Figure 116 - Comparison between hexahedral and tetrahedral quadratic elements.

9.3.4 Mesh size

This paragraph shows the results of a sensitivity analysis where the influence of element size on the acoustic power is studied, as shown on Figure 117. A dipole radius of *600 mm* is here used. Tetrahedral quadratic elements have been used and all the parameters apart from mesh size have been kept constant. 600 Hz frequency has been simulated. Figure 118 shows how the solution becomes smoother for decreasing mesh sizes. Figure 119 shows that to obtain an accurate solution, element size should be at least 1/4th of the wavelength of the sound (in this case *150 mm*).

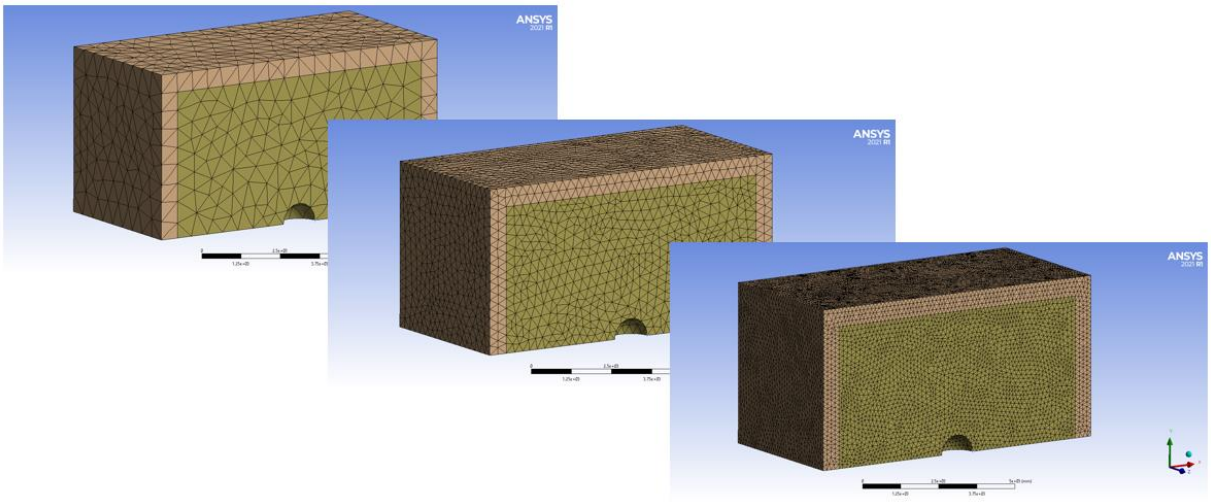

Figure 117 - Mesh size

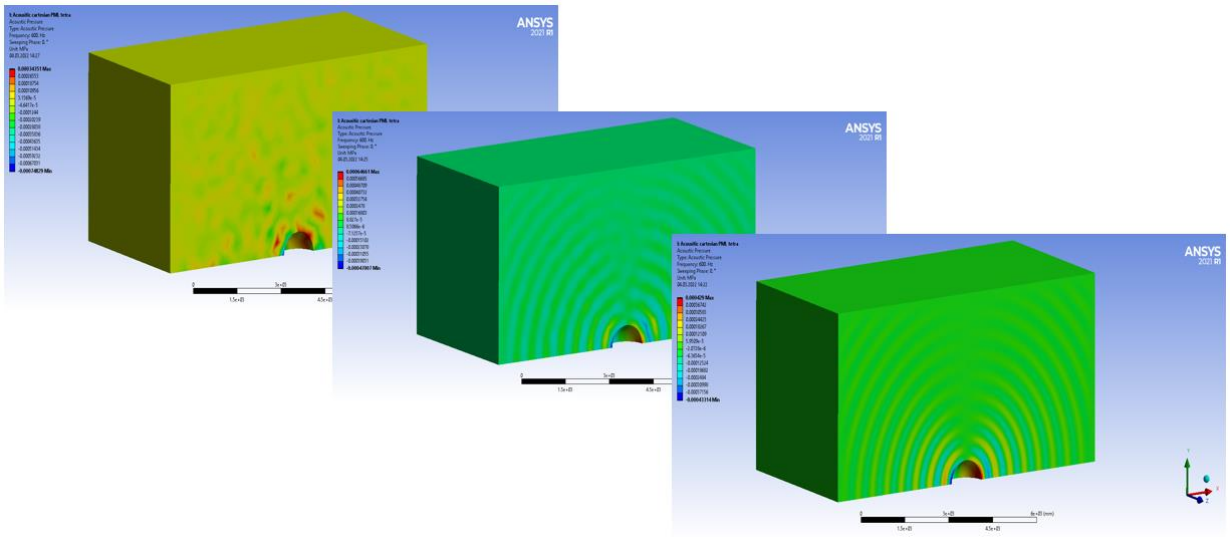

Figure 118 - Acoustic pressure for mesh size equal to one wavelength (left), half wavelength (middle) and 1/4th wavelength (right)

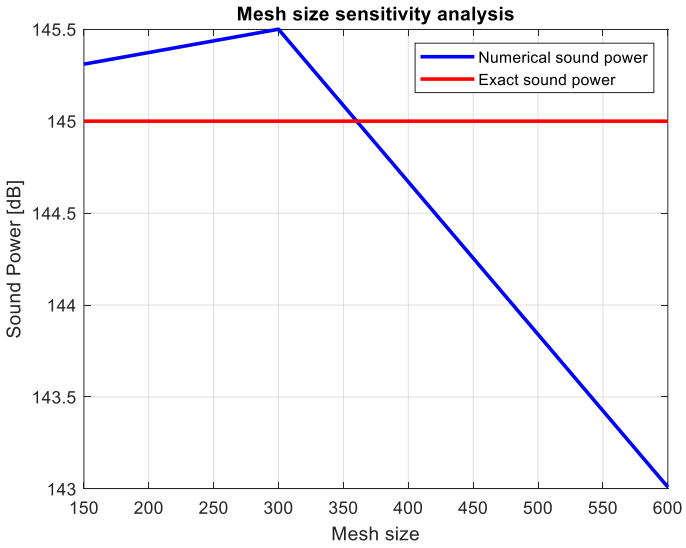

Figure 119 - Mesh size sensitivity analysis

9.4 Separation of contributions to Sound Power

As already mentioned, Ansys Maxwell doesn't allow to compute magnetostrictive forces alone. Only two options are available:
- computing Maxwell forces only or
- computing Maxwell and magnetostrictive forces together.

However, a simple numerical technique can be adopted to separate the contributions to the Sound power. Sound power can be written as follows,

$$W = F_1^H A_{11} F_1 + F_2^H A_{22} F_2 + 2Re\{F_1^H A_{12} F_2\} = W_{11} + W_{22} + W_{12}$$

where W is the total Sound Power, W_{11} is the Sound Power generated by magnetostriction, W_{22} is the Sound Power generated by Maxwell forces and W_{12} is the cross contribution, which is present since Sound Power depends quadratically on the exciting forces.

From two different Ansys Maxwell simulations, W and W_{22} can be computed. Two unknowns, W_{11} and W_{12}, are still present. However, performing another analysis in which magnetostrictive forces are scaled by an arbitrary factor a, the second following equation can be written,

$$W_a = a^2 F_1^H A_{11} F_1 + F_2^H A_{22} F_2 + 2aRe\{F_1^H A_{12} F_2\} = a^2 W_{11} + W_{22} + aW_{12}$$

where W_a is the total Sound Power considering a scaled magnetostriction. Scaling magnetostrictive forces is straight-forward and can be done by simply scaling the magnetostriction curve when assigning the core material.

The two equations above can be re-written as follows.

$$\begin{bmatrix} 1 & 1 \\ a^2 & a \end{bmatrix} \begin{bmatrix} W_{11} \\ W_{12} \end{bmatrix} = \begin{bmatrix} W - W_{22} \\ W_a - W_{22} \end{bmatrix}$$

The two unknowns W_{11} and W_{12} can be finally calculated. Three different analyses are needed. One in which Maxwell and magnetostrictive forces are considered, from which W is computed. A second one in which only Maxwell forces are considered, from which W_{22} is computed. A third one in which Maxwell and scaled magnetostrictive forces are considered, from which W_a is computed.

10. References

[1] IEC 60076-10-1:2016, *"Power transformers – Part 10-1: Determination of sound levels – Application guide",* https://webstore.iec.ch/publication/24409, 06.04.2022

[2] Ali Al-Abadi, *"Developing an accurate load noise formula for power transformers"*, 2019 6th International Advanced Research Workshop on Transformers – Cordoba - Spain, 6-7-9 October 2019, pp. 19-24, https://ieeexplore.ieee.org/document/8930195

[3] M. Kavasoglu, R. Hattel, C. Ploetner, *"Prediction of transformer load noise",* Excerpt from the Proceedings of the COMSOL Conference 2010 Paris, https://www.comsol.it/paper/download/63432/kavasoglu_paper.pdf

[4] D.K Lee, J.Y. Ryu, D.M. Kim, D.J. Kim, M.S. Lim, *"Load noise prediction of high-voltage transformers by equation applying 3D EMCN"*, 15 July 2020, IEEE Access, Vol. 8, pp. 130669 – 130677, (PDF) Load Noise Prediction of High-Voltage Transformers by Equation Applying 3-D EMCN (researchgate.net)

[5] B. Weiser, H. Pfützner, J. Anger, "*Relevance of magnetostriction and forces for the generation of audible noise of transformer cores*", 5 September 2000, IEEE Transactions on Magnetics, Vol. 36, No. 5, pp. 3759-3777, https://ieeexplore.ieee.org/document/908346

[6] https://en.wikipedia.org/wiki/Epstein_frame , 06.04.2022

[7] M. Javorski, J. Slavič, M. Boltežar, "*Frequency Characteristics of Magnetostriction in Electrical Steel Related to the Structural Vibrations*", December 2012, IEEE Transactions on magnetics, Vol. 48, No. 12, pp. 4727-4734, https://www.researchgate.net/publication/236964347_Frequency_Characteristics_of_Magnetostriction_in_Electrical_Steel_Related_to_the_Structural_Vibrations

[8] G. Shilyashki, H. Pfützner, J.Anger, K.Gramm, F. Hofbauer, V.Galabov, E. Mulasalihovic, "*Magnetostriction of transformer core steel considering rotational magnetization*", January 2014, IEEE Transaction on magnetics, Vol. 50, No. 1, pp 1-15, https://ieeexplore.ieee.org/document/6607168

[9] N. Baumgartlinger, C. Krell, H. Pfützner, G. Krismanic, "*Application of Neural Networks for the prediction of multidirectional magnetostriction*", 2 June 2000, Journal of Magnetism and Magnetic Materials, Vol. 215-216, pp. 617-619, https://www.sciencedirect.com/science/article/pii/S0304885300002420

[10] Krell *et al,* "*Relevance of multidirectional magnetostriction for the noise generation of transformer cores*", 2 June 2000, Journal of Magnetism and Magnetic Materials, Vol. 215-216, pp. 634-636, https://www.sciencedirect.com/science/article/pii/S030488530000247X

[11] Krell *et al,* "*Stress effects on the multidirectional magnetic behavior of grain-oriented silicon iron sheets*", 2 June 2000, Journal of Magnetism and Magnetic Materials, Vol. 215-216, pp. 63-65,

https://www.sciencedirect.com/science/article/pii/S0304885300000676

[12] Pfutzner, Hasenzagl, *"Fundamental aspects of rotational magnetostriction",* 1996, Journal of Nonlinear Electromagnetic Systems, pp. 374-379, https://books.google.it/books?hl=it&lr=&id=A5V2tIZofK4C&oi=fnd&pg=PA374&dq=Pfutzner,+Hasenzagl,+%E2%80%9CFundamental+aspects+of+rotational+magnetostriction%E2%80%9D&ots=4Vsmowtm-T&sig=IOwib0FP0Wr1fLnsbag0BgGhrXA&redir_esc=y#v=onepage&q=Pfutzner%2C%20Hasenzagl%2C%20%E2%80%9CFundamental%20aspects%20of%20rotational%20magnetostriction%E2%80%9D&f=false

[13] M. Mizokami, Y. Kurosaki, "*Noise variation by compressive stress on the model core of power transformers*", 1 May 2015, Journal of Magnetism and Magnetic Materials, Vol. 381, pp. 208-214, https://www.sciencedirect.com/science/article/pii/S0304885314012797

[14] A.J. Moses, P.I. Anderson, T. Phophongviwat, S. Tabrizi, "*Contribution of magnetostriction to transformers noise*", 31 August 2010, 45th International Universities Power Engineering Conference UPEC2010, Cardiff, UK, pp. 1-5, https://ieeexplore.ieee.org/abstract/document/5649285

[15] P. I. Anderson, A. J. Moses, H. J. Stanbury, "*Assessment of the Stress Sensitivity of Magnetostriction in Grain-Oriented Silicon Steel*", August 2007, IEEE Transactions on Magnetics, Vol. 43, No. 8, pp. 3467-3476, https://ieeexplore.ieee.org/abstract/document/4277884

[16] C. Holt, J. A. Robey, "*The AC Magnetostriction of 3.25-Percent Grain-Oriented Silicon-Iron under Combined Longitudinal and Normal Compressive Stress*", September 1969, IEEE Transactions on Magnetics, Vol. 5, No. 3, pp. 384-388, https://ieeexplore.ieee.org/abstract/document/1066458

[17] S. L. Foster, E. Reiplinger, *"Characteristics and Control of Transformer Sound",* IEEE Transactions on Power Apparatus and Systems, March 1981, Vol. PAS-100, no. 3, pp. 1072-1077, https://ieeexplore.ieee.org/abstract/document/4110701

[18] T. Phophongviwat, "*Investigation of the Influence of Magnetostriction and Magnetic Forces on Transformer Core Noise and Vibration*", https://orca.cardiff.ac.uk/56199/

[19] M. Ishida, S. Okabe, K. Sato, "*Analysis of Noise Emitted from Three-Phase Stacked Transformer Model Core*", October 1998, Kawasaki Steel Technical Report, No. 39, https://www.jfe-steel.co.jp/archives/en/ksc_giho/no.39/e39-029-035.pdf

[20] SS-EN ISO 9614-3:2009, *"Determination of sound power levels of noise sources using sound intensity",* Swedish Institute for Standards, https://www.sis.se/en/produkter/maskinsakerhet-357f77b1/acoustics/sseniso961412009/, 06.04.2022

[21] UNI EN ISO 3744-2010, *"Determination of sound power levels of noise sources using sound pressure",* *https://www.iso.org/standard/52055.html*

[22] NEMA ST 20-2014, "*Dry Type Transformers for General Applications*", https://www.nema.org/standards/view/dry-type-transformers-for-general-applications,

[23] IMO 468-IS, *"Code on Noise Levels on Board Ships",* 4 January 1982, Inter-governmental maritime consultative organization, https://wwwcdn.imo.org/localresources/en/KnowledgeCentre/IndexofIMOResolutions/AssemblyDocuments/A.468(12).pdf

[24] Watson, Farley and Williams, *"Code on Noise Levels on Board Ships",* https://zdocs.ro/doc/wfw-maritime-codeonnoiselevelsonboardships-e12lnn2go7pv

[25] M. Ertl, H. Landes, *"Investigation of load noise generation of large power transformer by means of coupled 3D FEM analysis",* 2007, COMPEL – The international journal for computation and mathematics in electrical and electronic engineering, Vol. 26, No. 3, pp. 788-799, https://doi.org/10.1108/03321640710751226

[26] Ansys, "*Maxwell Help 2021R1*", www.ansys.com

[27] R. Hattel, M. Kavasoglu, A. Daneryd, C. Ploetner, *"Prediction of transformer core noise",* Excerpt from the Proceedings of the COMSOL Conference 2014 Paris, https://www.comsol.ru/paper/download/199301/haettel_paper.pdf

[28] S.G. Johnson, *"Notes on Perfectly Matched Layers (PMLs)", https://arxiv.org/abs/2108.05348*

[29] Ansys, "*Acoustic analysis guide 2021R1*", www.ansys.com

[30] H. Fleischer, H. Fastl, "*Beiträge zur Vibro- und Psychoakustik*", https://www.researchgate.net/profile/Helmut_Fleischer/publication/281633344_Glockenschwingungen/links/57388ca408ae9f741b2bcd63.pdf

[31] Oak Ridge National Lab., TN.; Department of Energy, Washington, DC.; Verein Deutscher Ingenieure (VDI), Duesseldorf (Germany, F.R.), "*VDI 2230 Part 1 - Systematic calculation of high duty bolted joints*", 1984, https://ntrl.ntis.gov/NTRL/dashboard/searchResults/titleDetail/DE84003447.xhtml

[32] C.E. Crede, J.E. Ruzicka, *"Theory of vibration isolation",* http://160592857366.free.fr/joe/ebooks/Mechanical%20Engineering%20Books%20Collection/VIBRATIONS/Harris%20C.M.%20&%20Piersol%20A.G.%20-%20Harris'%20Shock%20And%20Vibration%20Handbook%205th%20Ed%20%5BMcGraw%20Hill%202002%5D/70811_30.pdf, 06.04.2022

[33] R. M. Hochhesier, *"How to select vibration isolators for OEM machinery & equipment",* Barry - Controls noise – Vibration Shock

[34] https://en.wikipedia.org/wiki/Dynamic_modulus, 06.04.2022

[35] A. L. Libardi, P. S. Varoto, "*Experimental Determination of Loss Factors on Coupled Structures Using The Power Injection Method",* Proceedings IMAC-XXII: Conference and Exposition on Structural Dynamics, 2004

[36] PerkinElmer, *"Dynamic Mechanical Analysis, a beginner guide",* *https://resources.perkinelmer.com/corporate/cmsresources/images/4474546gde_introductiontodma.pdf*

[37] K. Saarinen, L. Lamula*, "Noise control of common base frame",* Proceedings of the Sixteenth International Congress on Sound and Vibration, Krakow, Poland, 2009

[38] M. M. Winkler, *"Dynamic measurement of elastomer elements",* https://www.thkoeln.de/mam/downloads/deutsch/hochschule/fakultaeten/fahrzeugtechnik_und_produktion/nvh_fallstudie_elastomere.pdf

[39] C.A.J. Beijers, A. de Boer*, "Numerical modelling of rubber vibration isolators",* Proceedings of the Tenth International Congress on Sound and Vibration, Stockholm, Sweden, 2003, vol. 283, p. 284, https://ris.utwente.nl/ws/portalfiles/portal/5406048/Beijers03ICSV.pdf

[40] H. N. Ghalif, "*Vibration analysis of a generator anti-vibration rubber mounts*", 2016, Journal of Computer Science & Computational Mathematics, Vol. 6, No. 4, pp. 105-111, http://real.mtak.hu/92639/1/VIBRATIONANALYSISOFAGENERATORANTI-VIBRATIONRUBBERMOUNTS.pdf

[41] S. Kari, K. Timo, A Seppo, H. Pertti, *"Structure-borne sound power transmission through a point connection to a frame structure",* 20 September 2002 in Forum Acusticum Sevilla 2022, Sevilla, Espana, Sociedad Espanola de Acustica, https://research.aalto.fi/en/publications/structure-borne-sound-power-transmission-through-a-point-connecti